Prediction and Design of Colloidal Matter Using Directional Entropic Forces

by

Nayaz **Khalid** Ahmed

A dissertation submitted in partial fulfillment
of the requirements for the degree of
Doctor of Philosophy
(Chemical Engineering)
in The University of Michigan
2015

Doctoral Committee:

Professor Sharon C. Glotzer, Chair
Professor Ronald G. Larson
Professor Michael J. Solomon
Professor Anish Tuteja

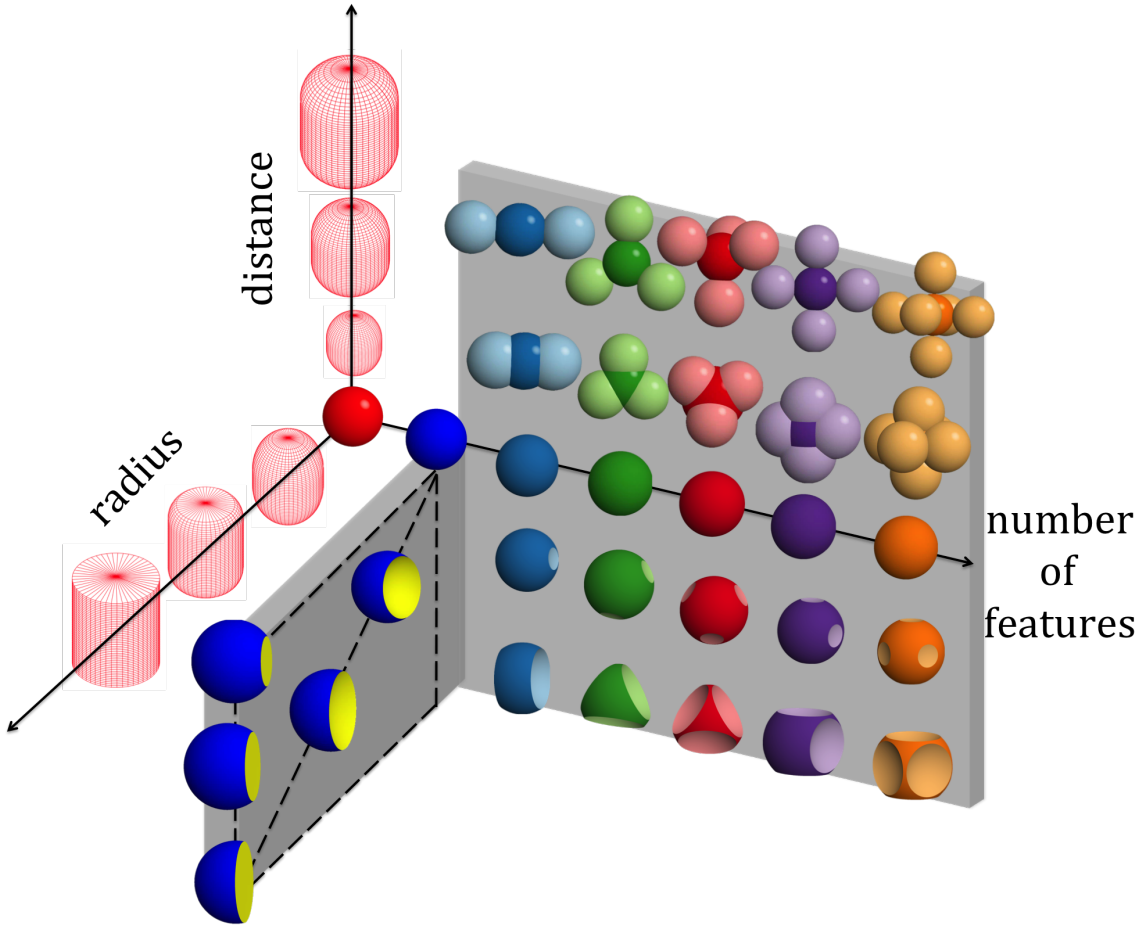
distance
radius
number
of
features

2015

For Noor,
and all my teachers.

A C K N O W L E D G M E N T S

First and foremost, I would like to thank God Almighty for blessing me with the opportunity to pursue my doctoral studies at the University of Michigan. The life of a researcher has many interesting turns - the ability to always sit back and know that He whose love knows no bounds is in control is very satisfying. Nothing can happen without His will and I am very grateful for these past five years.

The first person I would like to thank is my beloved wife, Noor. Life beyond the lab has been fun and eventful because of her. The fresh baked cookies, lovely road trips and beautiful memories helped provide the right balance to my life as a researcher.

Prof. Sharon Glotzer has been a very supportive advisor, allowing me to design my research and staying confident in my ability to do so effectively. Sharon provided me with lots of encouragement and freedom all along, apart from patiently working with me in my research.

Dr. Greg van Anders has played a pivotal role throughout my doctoral life. From helping me frame my research to understanding my results, Greg has always been there to help navigate various concerns through enriching conversations. At times, he has had more faith in my results than I did.

I would also like to thank my committee members – Professor Michael Solomon, Professor Ronald Larson and Professor Anish Tuteja, who were always available to provide valuable guidance and useful suggestions in my research and beyond.

I would like to thank the Glotzer group manager, Karen Coulter. Her willingness to handle all of the group's logistics helps ensure that the research keeps happening. Her attention to detail in documentation has helped me find answers to the most bizarre questions regarding travel, seminars and everything else – making my journey a much smoother ride.

The Glotzer group has been a great team to work with. I am immensely thankful to Dr. Eric Jankowski for teaching me the details of coding during my early years as a graduate student. Dr. Jens Glaser, with his unmatched speed in getting things done, has been a very friendly motivating force for me during the final

years of my PhD. Dr. Ben Schultz was a great companion to share office space, as we spent time talking about our careers and venting about all things beyond our control. Other members of the Glotzer group, including Dr. Michael Engel, Dr. Nguyen Nguyen, Wenbo Shen, Richmond Newman, Paul Dodd and Mayank Agarwal among others have been a integral part of many thought provoking discussions that have added great value to my doctoral life. There have been a number of friends outside my research circle who have played a big role in bringing balance to my life, including Dr. Mahesh Ganesan and Arjang Talatoff.

A special thanks also goes to Dr. Tershia Pinder-Grover, Dr. Susan Montgomery, and the rest of the team at CRLT-Engin for mentoring me in various life skills and helping me make important career decisions. I also wish to thank Prof. Sunitha Nagrath for her patience in guiding me during my teaching when I served as graduate student instructor. I would also like to thank the extremely cordial staff in the Chemical Engineering department, especially Susan Hamlin, for helping me on numerous occasions.

Finally, I would like to thank my parents for all their efforts in my early education. I was the child who never liked to go to school - and their constant effort helped change my attitude towards education. I will be forever grateful to them for all they have done for me.

TABLE OF CONTENTS

LIST OF FIGURES

LIST OF APPENDICES

ABSTRACT

Prediction and Design of Colloidal Matter Using Directional Entropic Forces

by

Nayaz Khalid Ahmed

Chair: Sharon C. Glotzer

We study the effect of entropic forces in the preferential binding of colloidal building blocks towards the assembly of target structures. By using methods developed to calculate the potential of mean force and torque, we quantify the interactions between convex facetted particles with increasing depletant concentration and find that pair-wise entropic interactions are up to a few k_BT. We use these interactions to determine the required depletant osmotic pressure to promote specific binding in different systems. We extend the notion of entropic binding from convex facetted particles to concave dimpled particles - geometrically achieved by reducing the radius of curvature of the entropic feature in a particle's shape. By understanding the transition between head-to-head and head-to-tail binding in systems with and without depletants, we evaluate that the robustness required of experimental techniques aimed at synthesizing facetted particles can be reduced in the presence of depletants larger that 0.4 diameters of the colloidal particles. We study the assembly of recently developed experimental building blocks that promise reconfigurable structures through their own shape reconfigurability. This study has necessitated the implementation of new overlap algorithms for Monte Carlo simulations of the equilibrium structures of convex and concave spheroidal particles,

particles that can be built as a combination of positive and negative spheres. Through the analysis of densest packing and assembly structures of concave spheroidal particles, i.e. multi-dimpled spheres, we generate geometric considerations that help *a priori* determine these emergent behaviors of entropic colloidal systems. Finally, through the study of packing and assembly of spherical union particles, i.e. positive unions of spheres, we develop a paradigm of entropic repulsive patches, necessary for the design of open crystal structures using entropy. We find open rotator face-centered cubic lattices at small protuberance amounts for all families of particles. At higher packing fractions, we find special crystal structures such as a rotator A15 phase with planar tetravalent particles and a hexagonal close packed phase with hexavalent particles. We believe that these assembly studies of spheroidal particles may provide insight into the assembly of protein building blocks, as proteins are complex systems that assemble under various depleting conditions into different open crystal structures.

CHAPTER 1

Introduction

> When nature finishes to produce its own species, man begins using natural things in harmony with this very nature to create an infinity of species.
>
> Leonardo da Vinci

1.1 Motivation

Most of the advances in human history have been achieved through the development of new materials that serve a novel function. During the Iron Age, the processing of iron was discovered and society advanced tremendously. New tools were built enabling rapid transportation that resulted in the exploration of many new lands and seas. More recently, the plastic age in the last half of the 20^{th} century provided us with flexible packaging materials, and the silicon age in the last quarter of the 20^{th} century opened the door to the world of electronics. Every advance in materials has been accompanied with a fundamental transformation in human life style forever.

The next generation of materials will be "designed" through building from the bottom-up. Bringing together various nano scale building blocks in a predetermined manner to achieve a target property will be the key ingredient in future materials. This can be achieved both through discovering nature's intelligent designs, and through experimental probing of various designs. These materials will again undoubtedly transform our civilization as we know it today.

Furthermore, these next generation materials will be also distinguished by their ability to adapt both on demand and to environmental cues in order to carry out targeted functions. The ability of materials to change structural, optical, electronic or other properties when needed, all require that the intrinsic building blocks that comprise the material be able

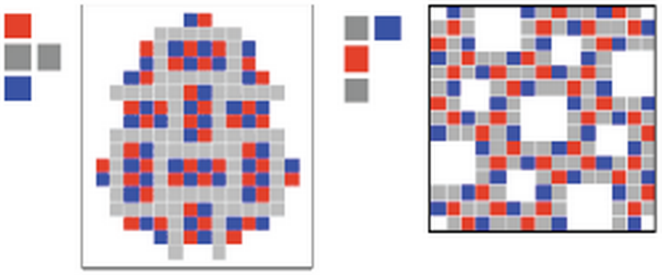

Figure 1.1: Two different assembled structures from similar model building blocks can be obtained through programmable shape and interactions. Based on work in Jankowski and Glotzer [1].

to switch from one structure to another. In biological systems, for which adaptability is ubiquitous and allows for critical function, the basic building blocks of biology – DNA and proteins – create structures that exhibit dynamic reconfigurability we require for the adaptive, functional materials applications described above.

If material building blocks could be imbued with programmable shape and interactions (see Fig. 1.1) so as to allow for their assemblies to actively and dynamically reconfigure in biomimetic fashion between distinct structures, then fundamentally novel capabilities (such as switching, programmability and autonomy) could be applied to the design of our next generation smart, adaptive materials. Recently, promising experimental techniques have been developed for the synthesis and fabrication of switchable building blocks capable of assembling into structures that can dynamically switch between two or more states.

It is our contention that the fundamental ability of a material's structure to dynamically reconfigure among two or more target structures is predicated on the ability of the structure to self-assemble from precursor building blocks whose shapes and interactions conspire to yield the right structure under the right circumstances. Self-assembly refers to this process, whereby a collection of objects (atoms, molecules, particles, etc.) spontaneously organize into a well-defined structure [10–12]. Surfactants self-assemble into micelles [13]; block copolymers self-assemble into lamellae [14, 15]; lipids self-assemble into cell membranes [16, 17], proteins self-assemble into viruses [18], birds self-assemble into flocks [19] – these are just a few of the many examples of larger structures formed from the spontaneous organization of smaller subunits or "building blocks".

Once assembled into a given structure, reconfigurability can be introduced by dynamically changing the shape of the building blocks, changing their interactions or changing their environment. The overall shape of building blocks can be easily tuned by swelling and shrinking them through the absorption or evaporation of a solvent from them. Interactions between building blocks can be changed by the introduction of salt in systems. Also,

the environment can be changed by introducing smaller "depletant" molecules in the system. These are viable techniques to increase the number of tunable structures that can be obtained from the same building block. These techniques form the primary basis of this work. We answer questions regarding the ability to self-assemble different structures from the same building block as a first step towards designing reconfigurable materials.

1.2 Self-Assembly for Materials Design

Self-assembly refers to the spontaneous formation of organized structures through a stochastic process that involves pre-existing building blocks, is reversible, and can be controlled by proper design of the components, the environment and the driving force [11, 12]. It is a governing principle by which materials form [10]. For customized materials on macroscopic length scales to be made, self-assembly is essential because the number of building blocks that would have to be precisely placed in the absence of a self-directed method are too large and the process is prohibitively time consuming. A Fermi approximation of the time required for building a 1 cm cube using 10 nm building blocks with the help of optical tweezers would be in the order of a billion days.

The basic idea promoting self-assembly is to develop building blocks that have sufficient information content inherent in them, allowing a desired structure to form spontaneously by moving to a minimum free-energy state after sampling an ensemble of possible configurations [2, 20]. Examples of self-assembled structures include lipid bilayers [16], peptide bundles [17], patchy nanoparticles [21–23] etc. amongst others.

Polystyrene colloidal crystals, consisting of charged monodisperse polystyrene microspheres suspended in water, self-assemble into a face-centered-cubic (fcc) lattice with lattice spacing comparable to the wavelength of light [24]. Such colloidal structures may also find applications in nanoscale electronics, miniature diagnostic systems and hierarchically structured catalysts amongst others [25]. However, for the assembly of more complex structures, it has been recognized that anisotropic shape and specific interactions (or "patchiness") are useful [2].

By offering strategies for generating nanostructures, self-assembly is important in a range of fields: chemistry, physics, biology, materials science, nanoscience, and manufacturing. Technologies involving nanometer-scale objects continue to improve the quality of our daily lives because the down-sizing of functional units can result in a significant decrease in device energy consumption and more efficient production processes. In addition, novel phenomena have been revealed at the nanometer-scale. Shrinking component size advances nanotechnology, while the related phenomena represent nanoscience. Therefore,

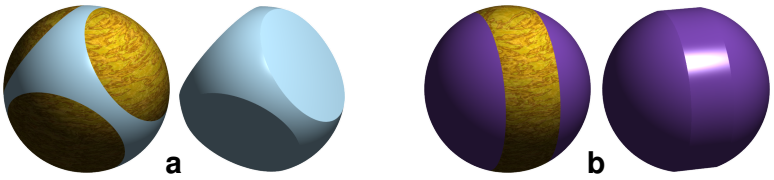

Figure 1.2: Many anisotropy dimensions for enthalpically patchy particles [2] have entropically patchy counterparts. Example traditional sticky patchy particles left (a) and (b) with entropically patchy counterparts right (a) and (b). Figure reproduced from [3].

the regimented fabrication of nanometer-scale objects is undoubtedly one of the central issues in current science and technology. Towards this end, world leading chipmaker Intel is now using self-assembly techniques for the development of chips with feature sizes less than 14 nanometers.

1.3 Enthalpy and Entropy

When the concept of self-assembly for materials design was proposed by Whitesides in 2002 [10], one of the motivating reasons was the ability to choose from a wide range of interactions (van der Waals, ionic, steric, magnetic, gravitational, electrostatic, and others) and the ability to adjust these interactions over wide ranges of strength, range, and selectivity. This has resulted in great flexibility in the design of building blocks for self-assembly.

The design principle of choosing from a wide range of interactions is equivalent to setting up an enthalpic potential for the interaction of particles. In such "traditional" patchy particles [2, 21], anisotropic interactions arising from patterned coatings, functionalized molecules, DNA, and other enthalpic means create the possibility for directional binding of particles into higher-ordered structures such as nanoparticle superlattices and colloidal crystals. Examples of patchy particles include Janus colloids [26–32], striped nanospheres [33] and nanorods [34], and DNA-coated patchy particles [35], among many others [2, 36].

With patchy particles, anisotropically placed patches promoting either specific or non-specific interactions with patches on other particles induce directional "bonding" between particles of the sort typically attributed to molecular substances. To date, patchy particles have been assembled into numerous structures [37–47], many of them isostructural to their atomic and molecular counterparts.

Another design principle involves the manipulation of building block shape for targeted self-assembly which takes advantage of the contribution of entropic forces. Since the work of Onsager [48], there has been considerable interest in the effects of shape on the

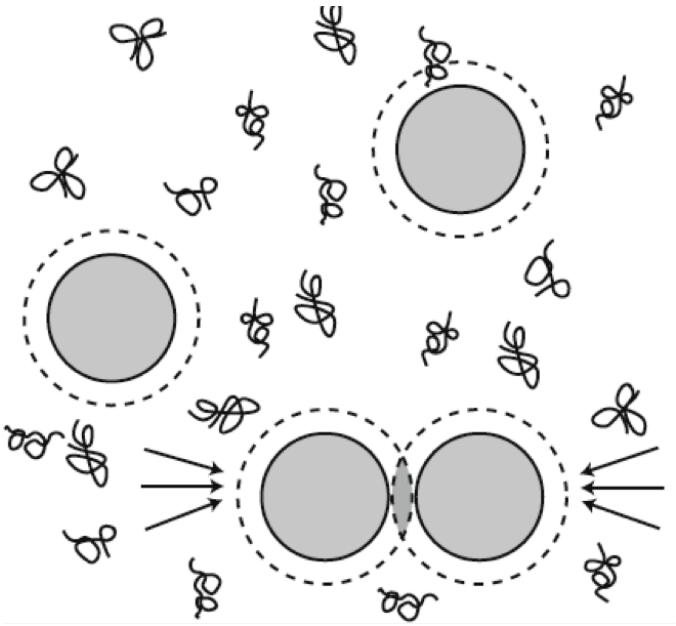

Figure 1.3: Effect of depletion. The free volume available to the depletants in this system, denoted by polymers, increases when spherical colloidal particles come closer to each other. Reproduced from Lekkerkerker [4].

form of assembled and ordered phases, beginning with spherocylinders [49, 50]. Early advances in nanoparticle synthesis led to the availability of various building blocks including spheres [51], cubes [52], rods [53], and tetrapods [54] at both the nano and micro scales. These entropic forces have been shown to assemble anisotropically shaped particles into complex structures [49,50,55–72]. A general observation from many of these studies is that dense suspensions of hard, facetted particles align their facets so as to maximize the system entropy, giving rise to ordered structures as complex as colloidal quasicrystals [57, 64] and crystals with unit cells containing as many as 52 particles [63]. Damasceno, *et al.* [63, 64] rationalized this tendency toward facet alignment as the emergence of "directional entropic forces" between hard particles. Directional entropic forces (DEFs) are not intrinsic to the particles, but instead are statistical and emerge from the collective behavior of the entire system upon crowding.

1.4 Depletion Interactions

Depletion interactions between colloidal particles are a unique way of controlling the self-assembly information inherent in the system [4]. Here the environment as well as the building block attributes together affect the binding force generated between the colloidal

particles. Depletion interactions are caused by the presence of smaller depletant particles, which promote the building blocks to bind in a fashion that would maximize the entropy of the system [73, 74]. The interaction between two colloidal spheres in a solution of depletants was first understood and explained as depletion interactions by Asakura & Oosawa [73].

Such effects of depletion have already been noted to occur in nature. In the 18th century, it was known that red blood cells (RBCs) tend to cluster, preferably with their flat sides facing each other, giving structures commonly known as "rouleaux" [75], as shown in Fig. 1.4. This aggregation of RBCs into "rouleaux" had been related to the increased serum protein concentrations of fibrinogen, globulin and albumin, and thus could be explained by depletion forces between RBCs, induced by the serum proteins [76].

Other similar examples include the formation of emulsion droplets when mixing biopolymers [77] (depletion-induced demixing), precipitation and isolation of viruses [78, 79], and aggregation and creaming of emulsion droplets [80, 81] (micelles as depletants).

Depletion interactions can be understood as a form of attraction through repulsion [4]. They are a beautiful example of entropically driven self-assembly. The key feature of depletion interactions is the hierarchy of length scales, introduced by two different sized particles. The minimum free-energy state of the system is found by maximizing the entropy of a system of colloidal particles and smaller depletant particles. In 1954, Asakura and Oosawa [73] provided the first theoretical explanation for depletion interactions when they derived the specific depletion force between two spherical colloidal particles using a force balance approach. This result was independently recovered and further elaborated by Vrij in 1976 [74]. In these models, the colloids are represented by hard spheres of radius R_c, while the polymers are assumed to be spheres of radius R_p that are mutually interpenetrable, yet cannot penetrate the colloidal particles. As a consequence, every colloidal particle excludes a sphere of volume $\frac{4}{3}\pi(R_c + R_p)^3$ to the polymers. When two colloidal spheres are brought together, these spherical volumes will overlap and the volume accessible to the polymer will increase. It is this increase in free volume that causes an effective attraction and the eventual phase separation of the colloids.

The depletion force between two colloidal particles can also be calculated by writing out the partition function of the system in two different configurations – with and without the effect of depletants [8]. For a system of colloids and depletant particles, the partition function is given by

$$Z = \int [dp] \exp(\frac{-\beta p^2}{2m}) \int_{V'} [dq] \int dp_{cm} \exp(\frac{-\beta p_{cm}^2}{2M}) \int dq_{cm} \int d\mathbf{q}_{cm} \qquad (1.1)$$

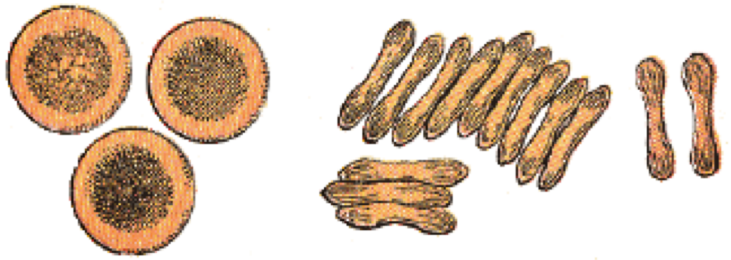

Figure 1.4: Depletion effect in nature. Red blood cells (left – top view) tend to cluster with their flat sides facing each other, giving a structure known as "rouleaux" (right – cross section). This aggregation is related to increased serum concentrations, and thus has been explained to be caused by depletion forces. Reproduced from [5].

where $V^{'}$ is the volume of the system available to the depletant particles, p and q denote the positions and quaternions of the colloidal particles and p_{cm} and q_{cm} denote the same for the center of mass of the depletant particles.

The free energy difference in the presence of depletants can then be shown to be

$$\Delta F = \frac{N}{\beta}\log(1-\frac{\Delta V}{V}) \approx \frac{-Nk_BT}{V}\Delta V \tag{1.2}$$

where ΔV is the volume between the colloidal particles that is gained by the depletants when the colloidal particles bind together.

The depletion force calculated from the free energy difference is proportional to the temperature of the system, which is a hallmark of entropic forces:

$$F = \frac{\partial F}{\partial x} \approx -(\frac{Nk_BT}{V})A \tag{1.3}$$

Also, assuming that the depletant particles behave like an ideal gas, with $PV = Nk_BT$, we get $F \approx -PA$, where A is the cross-sectional area that the depletant pressure acts upon. This implies that the depletion effect is osmotic in nature, and thus the depletant particles want to fill the excluded volume.

It has been shown using theory as well as experiments that the strength of depletion interactions is dependent on the concentration of the depletant particles and the range of the interacting potential is dependent on the size of the depletant particles [4, 73]. Most experiments on depletion interactions are conducted using colloidal particles and polymers in a solution. The colloidal particles are typically much larger than the gyration radius of the polymer.

In the past decade, these interactions were initially used for shape-dependent colloidal

separations [82]. The motivation of such work has been the fact that depletion interactions between colloidal particles depend on their shape. Thus, in systems of similarly sized particles with different shapes, particles of the same shape aggregate and precipitate out, one after the other, as depletants are added. The order of the shapes that precipitate depends on the free volume gained by the binding of the colloidal particles – particles that lead to the maximum free volume gain precipitate out first. This principle has also been applied for the separation of gold nanoparticles of different shape [83].

More recently, colloidal self-assembly has been directed using roughness controlled depletion attractions [84]. The aim of this work was to understand the effect of roughness on the depletion strength, when the order of roughness is about the depletant diameter. It was shown that when the height of roughness is greater than the depletant diameter, there is no depletion-induced aggregation. This work shows that in experiments performed to study depletion interactions, surface roughness is to be controlled to be within the order of the depletant diameter.

In recent studies by Barry and Dogic, smectic structures have been formed from homogenous monodisperse rods, as a function of the strength of the depletion attraction [85]. Two-dimensional discs were initially assembled by depletion effects of filamentous virus on a solution of dextran rods, and then upon further increasing to a much higher concentration of depletants, these two-dimensional discs assembled up to form larger three-dimensional cylindrical structures. These structures are found to be smectic from the point of view of the rod. This work [85] also reports that at intermediate concentration of the depletants, the discs prefer an edge-to-edge bonding to form a colloidal membrane.

Depletion interactions have also been shown to promote angularly specific binding in lock-and-key colloids [86–90]. The volume gained by the depletants is large when the key fits into the right sized dimple in the colloidal particle, thus resulting in a large gain in their entropy. This system is particularly interesting because the assemblies are not fixed and the ball and socket joint is free to move.

A large number of similar experimental studies have been conducted on depletion effects in various colloidal systems. There are also interesting theoretical studies about depletion forces and various attempts have been made at understanding the phase behavior of colloid and polymer mixtures. Lekkerkerker et al proposed a free-volume approach to calculate the phase behavior of colloid-polymer mixtures [91]. The key quantity in this approach is the statistically averaged volume that is available for the polymers at a given polymer activity set by a hypothetical reservoir. Using this approach, the partitioning of the polymer between colloid-rich and colloid-poor phases was taken into account, and this resulted in the emergence of three-phase coexistence regions between a colloidal gas, liq-

uid and a crystal in the phase diagram. This model can be used to study depletion effects, as the depletants can be modeled as non-adsorbing polymers. In order to compare between this "free-volume" approximation model and exact analytical results, solvable one-dimensional models of a binary mixture of hard rods of different lengths have been studied [92]. This work helps understand the range of compositions and densities over which the "free-volume" approximation may be used to understand the properties of hard-sphere mixtures.

Depletants are often simulated as penetrable hard spheres, an idea first proposed by Asakura and Oosawa [73] in their understanding of depletion interactions. More recently, numerical studies of the effective depletion potential between a pair of hard-spherical colloids in the presence of interacting depletant particles have been conducted [93]. Results show that depletant-depletant attractions favor colloidal aggregation. Interestingly, the effective pair-potential also becomes increasing long-ranged, and its radial dependence is represented by an exponential decay. Such sensitivity of the depletant critical fluctuations, where strength and range of interaction can be significantly changed by a small change in temperature, is a promising method for manipulating colloidal aggregates.

1.5 Thesis Overview

The main goal of this thesis is to propose shape modifications to spherical particles in order to use directional entropic forces for their self-assembly. Prior work has focused on lock and key particles and Pacman shaped particles in the presence of depletants. We extend this to more complex systems in order to achieve a holistic understanding of the factors at play during self-assembly. We consider both continuous and discrete shape modifications including stretching of spheres into capsules and modifying their radius into cylinders (chapter 3), bisecting spheres into hemispheres (chapter 4), introducing multiple concave dimples on spheres (chapter 5) and adsorbing protuberant spheres on the surface of spheres (chapter 6).

We begin this thesis with gaining a better understanding of the role played by depletants in systems of a pair of particles, for various changes in particle shape. In Chapter 2 we review Monte Carlo methods that are used to perform self-assembly simulations in subsequent chapters and present new work detailing the overlap algorithm for dimpled spheres and the method used to model depletants as implicit penetrable hard spheres. In Chapter 3, we quantify the interactions between a pair of particles in the presence of depletants. In Chapter 4, we extend this understanding to *a priori* predict the bulk self-assembly of a pair of particles in the presence of depletants by performing free volume calculations in

different configurations of colloidal particles. In Chapter 5, we model multiple symmetric concave features on spherical particles in order to understand the underlying controlling mechanism in their assembly. We use densest packings and self-assembly phase diagrams to determine the role of dimple volume in the emergent behavior of these systems. In Chapter 6, we also consider complementary protuberant spheres on the surface of a surface and understand their densest packing and self-assembly. These systems may be a starting model for the representation of proteins and hence these studies are found to be insightful.

CHAPTER 2

Methods

> A research problem is not solved by apparatus; it is solved in a man's head.
>
> Charles F. Kettering

In this chapter, we discuss the details of the computational tools used throughout this work. This chapter is organized as follows. In Section 2.1, we detail the Metropolis Monte Carlo simulation scheme. In Section 2.2, we briefly discuss the Hard Particle Monte Carlo (HPMC) plugin that has been implemented in HOOMD-Blue [6]. We also explain a new overlap algorithm, developed by Chen [7] and implemented here, for particles that are composed of positive and negative intersections of spherical volumes. In Section 2.3, we explain the implementation of penetrable hard sphere depletants as implicit depletants in HPMC.

2.1 Monte Carlo Simulations

Drawing motivation from morphological subunits of virus capsids called capsomeres, Monte Carlo studies of the self-assembly of anisotropic cone-shaped particles with directional attractions have demonstrated that structures with predesigned geometric accuracy could be obtained from such building blocks [23]. We consider similar and more advanced computational methods to understand the self-assembly of a new range of building blocks, as we finely tune both their shape and environment.

Metropolis Monte Carlo (MC) simulation [94–97] is a common technique that has been used to study the self-assembly of anisotropic building blocks. The Metropolis sampling scheme [94] avoids unnecessarily checking thermodynamically irrelevant configurations by generating a sequence of configurations that asymptotically approaches the underlying equilibrium distribution to be sampled.

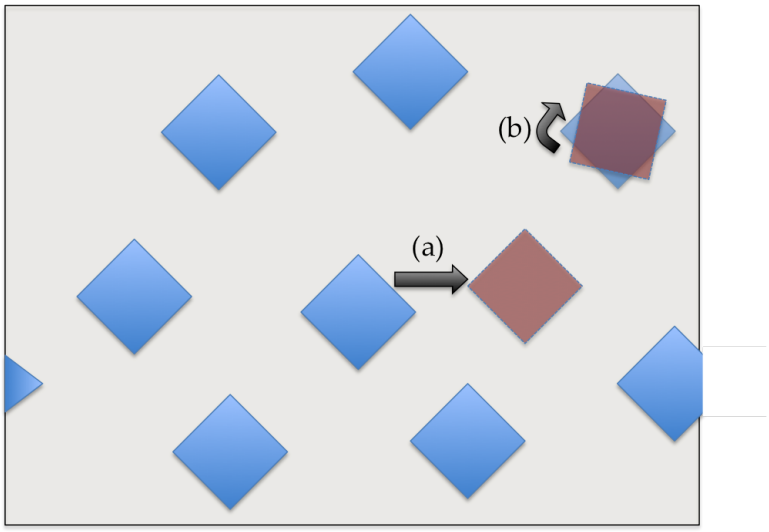

Figure 2.1: Example trial moves in a typical Monte Carlo simulation. Translational moves (a) and rotational moves (b) are performed on randomly selected particles in the system.

In this work, we develop and employ Monte Carlo simulations for studying the self assembly of anisotropic particles in the NVT and NPT ensembles, where number of particles, volume and temperature, and number of particles, pressure and temperature, respectively are held constant. Monte Carlo simulations are a straightforward and efficient way to sample a thermodynamic ensemble, so long as the system being modeled is ergodic [95–97]. Ergodic systems are those where the time average is the same for all initial points: statistically speaking, the system that evolves for a long time "forgets" its initial state. Hence any state can be accessed from any other state in a finite number of moves. A condition called detailed balance is sufficient to ensure the chain of states sampled in a Monte Carlo simulation is ergodic. This condition can be stated by equating the probabilities of being in states i and j, and the probabilities of transitioning from one to the other $\pi(i \rightarrow j)$, *i.e.*,

$$P_i \, \pi(i \rightarrow j) = P_j \, \pi(j \rightarrow i) \tag{2.1}$$

where π is the Markov transition matrix, and P_i and P_j are the probabilities of being in states i and j respectively.

The implementation of moves that obey detailed balance can vary from simulation to simulation. In general, at the beginning of a move, a particle is picked at random and given a uniform random displacement along each of the coordinate directions (both translational and orientational displacements), as shown in Fig. 2.1. This transforms the system from an initial state m to a final state n. The next step of a MC move is to determine the change in the internal energy of the system, ΔU. The determination of ΔU does not require a com-

plete recalculation of the configurational energy of the m^{th} state, rather only the changes associated with the particle undergoing displacement:

$$\Delta U = \sum_{j=1}^{N} u(r_{ij}^{n}) - \sum_{j=1}^{N} u(r_{ij}^{m}), \tag{2.2}$$

where the sum over particles excludes interactions $j = i$.

If the move is downhill in energy ($\Delta U \leq 0$), then the probability of state n is greater than that of state m and the new configuration is accepted. If the move is uphill is energy ($\Delta U > 0$), then the move is accepted with a probability equal to the Boltzmann factor of the energy difference, *i.e.*, $\exp(-\beta \Delta U)$. If the uphill move is rejected, the system remains in state m and an alternate move is attempted. This form of the probability ensures that the Markov chain converges to the Boltzmann distribution. Once equilibrium is achieved, every set of positions of the particles in the phase space of the ensemble corresponds to a minimum free energy. Thus, each time step represents a possible microstate that the real system might be in, amongst the large number of microstates in the ensemble. Thus this method allows us to take an ensemble average of the various properties of the system, and by ergodicity, this is equal to the time average of those properties of the system.

In all the systems considered in this work, we assume that the particles are, thermodynamically speaking, "hard". In hard particle Monte Carlo simulations, interactions between the particles are determined by means of their overlap. This implies that there are no energetic interactions between the particles, rather they are purely steric. As a result, the interactions between the particles are determined by geometric overlaps between neighboring particles when a trial move is attempted. If no overlap occurs, the trial move is accepted. If an overlap occurs, the interaction energy goes to infinity and thus the trial move is always rejected.

In our simulations, a full Monte Carlo cycle consists of $N + 1$ trial moves including arbitrary translation, rotation, and box shearing moves. Maximum step sizes are updated occasionally to keep the acceptance probabilities at 30%. Simulations are initialized at low packing fraction in a random configuration and subsequently compressed to higher densities. Crystallization (assembly into crystals) proceeds in three steps: (1) equilibration of the dense, metastable fluid (for example, $N = 512$: $< 0.1 \times 10^6$ Monte Carlo cycles); (2) nucleation and growth ($\sim 1 \times 10^6$ Monte Carlo cycles); and (3) healing of defects ($> 1 \times 10^6$ Monte Carlo cycles). Longer simulations facilitate equilibration in the transition region.

The number of Monte Carlo cycles performed for healing is at least an order of magnitude larger than the cycles for nucleation and growth. Thus we report structures that are

stable for long periods on our simulation time scales, longer than the auto-correlation time of crystal growth in these systems. All findings are verified by running independent simulations with different initializations and in different box sizes. The assemblies reported are those that form at the minimum density.

2.2 Hard Particle Monte Carlo Plugin for HOOMD-Blue

Hard particle Monte Carlo (HPMC) is a plugin developed for HOOMD-blue [6] that implements hard particle Monte Carlo (MC), with highly efficient parallel implementations both on the GPU and modern multi-core CPUs. HPMC represents each particle as an anisotropic particle with orientation and shape. The potential energy is zero when particles do not overlap and infinity when they do. The serial algorithm selects a single particle at random, proposes a random trial move, and then accepts or rejects that trial move. A new algorithm was recently designed for proposing many trial moves in parallel. The method works by splitting the simulation domain into cells and coloring them (four colors in 2D, eight in 3D) so that parallel moves are possible in the same color cells. Trial moves that cross cell boundaries are rejected to maintain detailed balance. We apply a random shift of the cells to restore ergodicity. Initial work on parallel MC focused on hard disk simulations accelerated on GPUs [98]. Since then, support has been included for 3D simulations, triclinic boxes, anisotropic particles, and an adaptation of the parallel algorithm to enable MPI domain decomposition across many CPU cores or many GPUs. Today, HPMC supports 2D and 3D simulations, a variety of shapes (polygons, convex polyhedra, general polyhedra, spheres, ellipsoids, rounded convex polygons, rounded convex polyhedra, faceted spheres), NVT and NPT ensembles, and pressure sampling in NVT ensembles.

2.2.1 Overlap Algorithm for Dimpled Spheres

For the work included in this thesis, a new overlap algorithm was developed by Chen [7] and implemented in HPMC. This overlap algorithm works with particles that can be defined as positive or negative intersections of the volume inside or outside of, up to, eight spheres. This algorithm has been implemented such that it takes full advantage of all features in HPMC - including running on multi-core CPUs as well as single and multiple GPUs.

The overlap check for convex particles cannot be directly extended to concave particles. Previous theoretical work on concave particles in 3D [99–102] used modifications of an overlap algorithm introduced by He and Siders [103] that required the radius of the valence sphere to be smaller or equal to the parent sphere and the particles were restricted to one

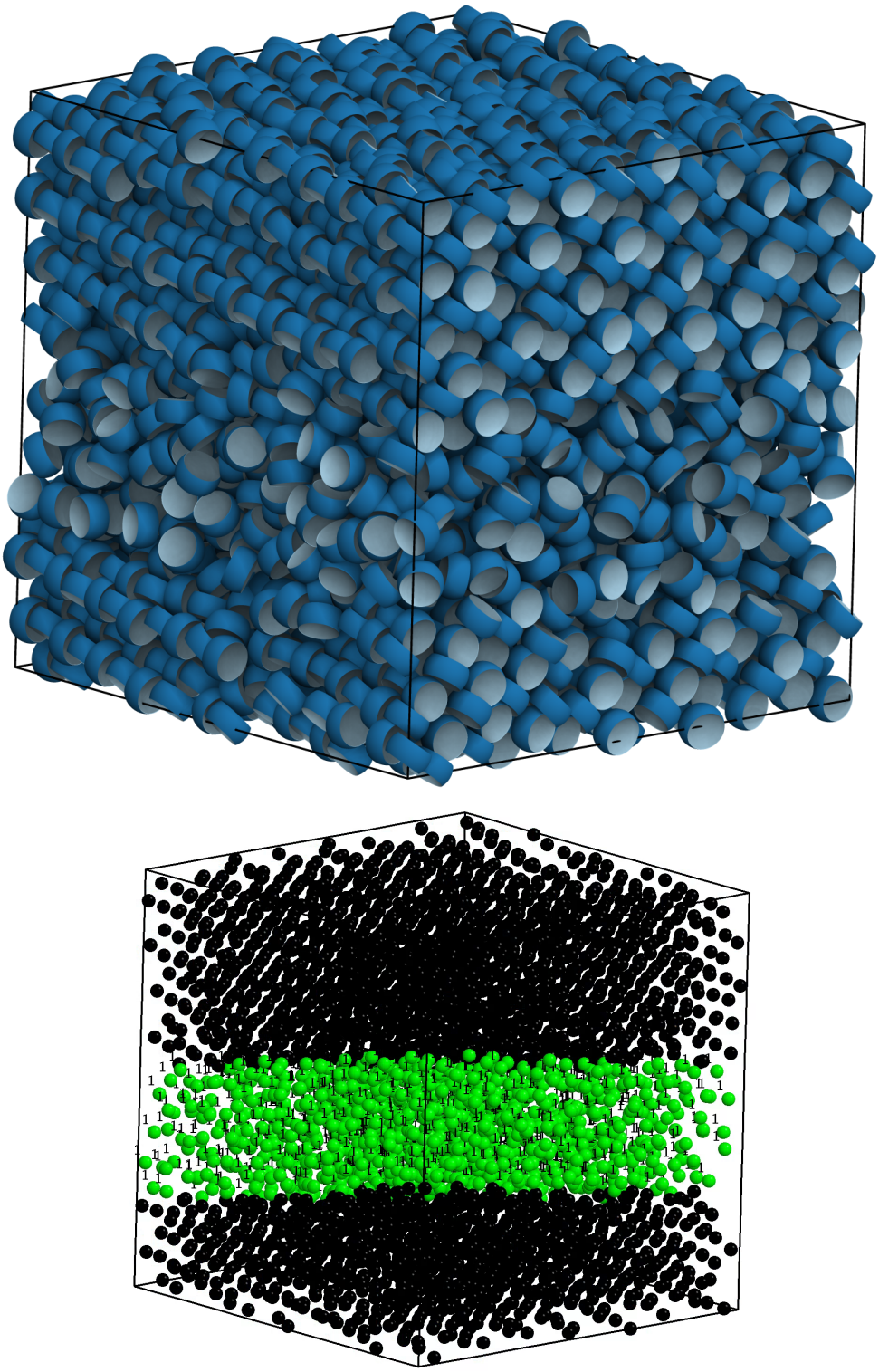

Figure 2.2: Monte Carlo simulation of 4096 bivalent dimpled spheres performed using Hard Particle Monte Carlo (HPMC) plugin for HOOMD-Blue [6]. The particles form a parquet crystal structure, and the system is undergoing nucleation and growth from a fluid to crystal. Below, we show the centers of the particles, where the green particles are in a fluid phase surrounded by black particles that arrange in a crystal lattice.

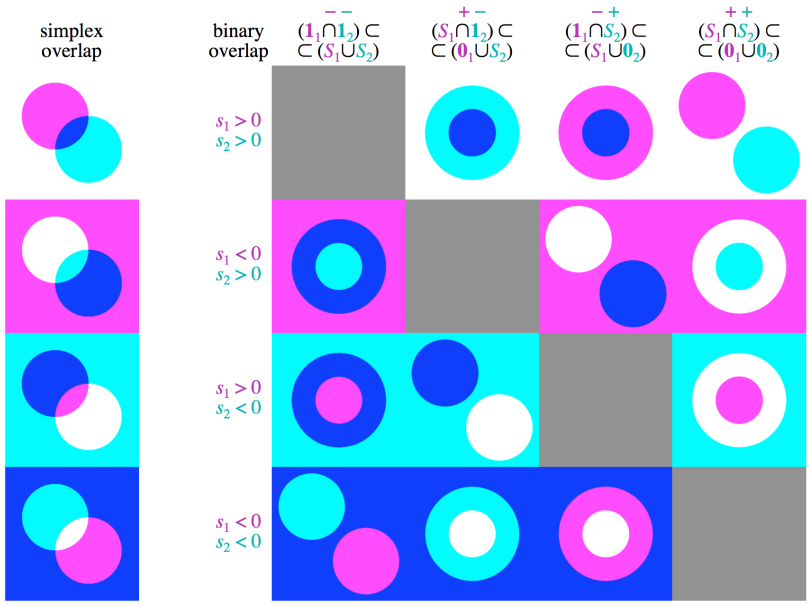

Figure 2.3: Overlap algorithm for particles made of spheres. For particles made of two spheres (Pacman particles), we show simplex overlap (left) within a single particle and binary overlap (right) between two particles $s1$ and $s2$ and the volume inside and outside of them. The diagonal $[k = l]$ is impossible (gray), row k has infinite region with color k, column l has no region with color l. Mutual intersection is shown in blue and the mutual union is shown in all colors except white. Figure reproduced from [7].

valence sphere, ($n_D = 1$). We instead use an overlap check algorithm that was designed for the "SPHINX (SPHere INterseXions)" family of shapes studied here, where previous constraints have been lifted ($n_D \geq 1$). The algorithm [7] implements a recursive algorithm based on the Cayley-Menger volume determinant and similar dihedral angle determinants. This overlap algorithm considers all topological types of overlap among the spheres and calculates the mutual union and the mutual intersection among them.

For the dimpled spheres studied in this work, we calculate the mutual intersection of the positive central sphere with one negative valence sphere from each surrounding particle by means of a recursive algorithm, as shown in Fig. 2.3. This requires the evaluation of overlaps between intersections of spheres. This is calculated by means of an initial trivial algorithm to calculate the separation of the union of the spheres, and then a recursive algorithm is applied to evaluate the separation of the intersection of the spheres. The overlap between the intersections is then evaluated as the opposite of the existence or non-existence of the separation between the intersections.

2.3 Modeling Depletants as Penetrable Hard Spheres

Some of the work included in this thesis models systems with depletant particles. We developed a code to treat implicit depletants as an alternate integrator for HPMC.

The implicit depletant code has been written as an integrator option for HPMC. As is standard when studying depletion, the code models the depletant particles as penetrable hard spheres. The penetrable hard sphere model allows particles of the same type (depletants) to overlap but particles of different types (colloids and depletants) are not allowed to overlap. The code follows the thermodynamics of a semi-grand canonical system wherein the simulation box is connected to a depletant reservoir of some user-specified concentration and the chemical potential of the depletants between the simulation box and reservoir is kept at a constant.

The code works as follows: first a colloidal particle is randomly selected in the simulation. A trial move is performed on the colloidal particle in typical Monte Carlo fashion. If the colloidal particle overlaps with another colloidal particle, this trial move is rejected as colloidal particles are modeled as hard particles. Depletant particles are next randomly thrown in a spherical volume encompassing the colloidal particle. The number of depletant particles thrown corresponds to a binomial distribution about the user-provided value of the depletant number concentration in the reservoir. We use a binomial distribution to model the number of successful depletant throws required, equivalent to a sample of n depletants drawn from the reservoir depletant population. This is important to ensure that detailed balance is maintained. The number of overlaps in the old configuration and the new configuration are recorded. Next, the move is accepted or rejected based upon a random value weighted according to the probability of successfully throwing a depletant with no overlaps in the initial configuration as compared to the probability of doing that in the trial configuration. These moves can be conducted in parallel across the system in the same manner as is done for HPMC.

As a result of explicitly throwing the depletants for each trial move, the depletants have uncorrelated positions at every trial move. This helps increase the dynamics of depletant particle movement within the system and does not affect the dynamics of the colloidal particles because the two species have different time scales.

2.4 Summary and Conclusion

In this chapter, we described the Monte Carlo simulation technique that we used to determine the phase diagram of crystal structures formed by different particles, by means

of sampling through important configurations to understand their self-assembly. We also described the implementation of the Monte Carlo simulation technique for hard particles, and briefly explained the working of the hard particle Monte Carlo integrator that has been added as a plugin to HOOMD-Blue [6]. We discuss a new overlap algorithm [7] that has been developed to perform simulations of dimpled spheres. This algorithm was successfully implemented within the HOOMD-Blue and HPMC frameworks taking full advantage of the scalability to multi-core CPU and GPU simulations of large system sizes, necessary for the work carried out in this thesis. Finally, we discuss the implementation of an implicit depletant integrator in HPMC that has been used to understand systems with depletant molecules that are modeled as penetrable hard spheres. This scheme was used for self-assembly simulations of systems with depletants throughout this work, and is being continuously improved and further extended at the time of publication of this thesis.

CHAPTER 3

Understanding Depletion Through PMFT Calculations of Facetted Particles

3.1 Introduction

Asakura and Oosawa's treatment of depletion interactions [73] has resulted in a large body of experimental work using depletants. They considered the effective interactions between a pair of colloidal spheres in a sea of soft polymeric depletants, as shown in Fig. 3.1. Consider a shell around each colloid, the thickness of which is of the order of the radius of the depletant. The region of this shell is inaccessible to depletants due to steric hindrance. When two colloidal particles are sufficiently close together, the intersection of their shells creates an overlapping region that is not available to the depletants because of steric hindrance. At this distance between the colloids, where the shells overlap, the volume of the intersecting region will be made available to the depletant particles in the rest of the system. This gives the depletant particles more translational freedom resulting in a greater entropy for the system, while inducing an effective attraction between the two colloidal particles[1].

Though the concept holds at varying size ratios, in colloquial usage the term "depletion" is often used to refer to systems in which the depletant particles are small compared to the colloidal particles and penetrable or semi-penetrable with respect to each other.

In many ways, the depletion effect for small depletants shown by Asakura and Oosawa is similar to the nematic ordering of hard rods shown by Onsager: the restriction of some specific degrees of freedom in the system (i.e. ordering) through the creation of a hierarchy of length scales. Onsager's rods have two length scales (the length and diameter of the rod) and Asakura-Oosawa's binary system consists of two species of spheres with different diameters. The techniques used to demonstrate the ordering in the two systems were different. Onsager used integral equations to examine coarse-grained densities of the rod

[1]This chapter is adapted from Reference [8]: G. v. Anders, D. Klotsa, N. Khalid Ahmed, M. Engel, S. C. Glotzer, Understanding Shape Entropy through Local Dense Packing, *PNAS* 111 (45) E4812-E4821, 2014

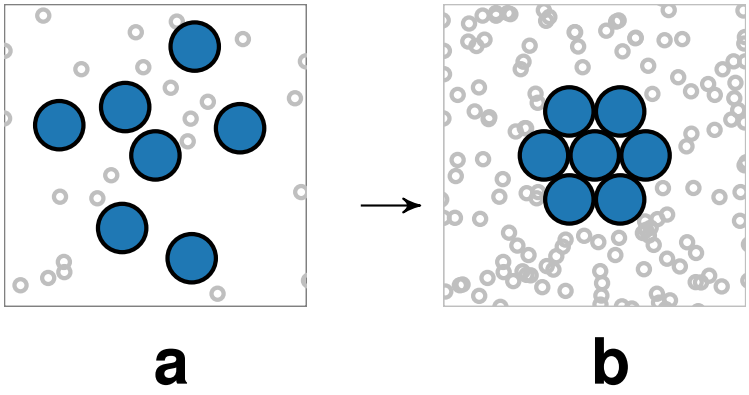

Figure 3.1: Effect of depletion in a monodisperse suspensions of hard disks. Adding in conventional small depletants induces a short-ranged attraction (a), however low concentrations do not induce aggregation. High depletant concentration can cause aggregation (b). Figure reproduced from reference [8].

distribution (as did Kirkwood with spheres), whereas Asakura and Oosawa considered effective pair interactions between two colloidal particles in a sea of depletants. However, de Boer [104] (and later also Vrij [74]) also considered similar systems to Kirkwood's hard spheres, but from an effective pair interaction approach, similar to that used in the later work of Asakura and Oosawa for colloid-polymer mixtures, and thereby providing a microscopic description of the mechanism underlying the ordering of hard spheres.

In the original treatment of Asakura and Oosawa [73] the depletants are soft penetrable spheres but can vary in size. There are various theoretical and experimental works for small depletants and large colloids where the depletant softness is varied (see [105] and references in [4]). It is widely known from the work on depletion systems that interactions among depletants often affect the effective interactions between colloids [4].

There has been experimental and theoretical work on systems of particles with moderate shape in the presence of small hard depletants, starting with [82], and followed by work on rough colloids in [84,106–111], as well as more anisotropic shapes [62,112,113]. However, strictly speaking, these systems do not have single shapes, but rather are mixtures due to the presence of anisotropic colloids and hard sphere depletants. Note that the lock-and-key system studied in [114–117] is technically a ternary mixture of particles. Work exists on particles with extreme shape, where properties of self-assembled membranes have been investigated at both continuum and molecular length scales. [85]. For a review of shape and depletion, see [118]. For a more general review of shape and assembly see [72].

In particular, both experiments and computer simulations suggest that the shape of col-

loidal particles plays a role in determining the form of their assembly. Yet, hitherto, it has not been possible to state this with any precision because a means of quantifying the effect of shape has been lacking. Indeed, it is known that in experimental systems there are many forces (*e.g.* van der Waals, electrostatic, etc.) that influence the self-assembly of the system. And, there are various techniques for measuring these forces, see *e.g.* [119, 120]. In contrast, no such techniques exist in the literature for quantifying the DEFs that arise from particle shape, though one may envision extending the use of optical tweezers [121] and confocal microscopy [122] in the case of colloids. Precisely defining these forces, and introducing a means of quantifying them would provide a way to determine whether and how much particle shape plays a role in self-assembly, especially compared to other forces that we know exist at nanometer scales.

3.2 Directional Entropic Forces for Colloids with Penetrable Hard Sphere Depletants

Directional entropic forces, as discussed below, are effective forces that exist between classical particles in thermal systems (e.g. nano- or colloidal particles) solely due to their anisotropic shape. The first suggestion of the existence of these forces came from the consideration of monodisperse hard particle systems [63].

We note that in experimental systems with sufficiently large depletants, e.g. [62], once the depletants have caused the aggregation of the colloidal particles, the ordering of the colloidal particles within the aggregate is determined by colloidal shape. In particular, if the size of the depletant is larger than the gaps between the colloidal particles, the depletants are, in effect, only serving as soft walls for the colloidal particles (see Fig. 3.1). In this sense, an entire mixed colloid-depletant system being studied in a beaker is at fixed volume, whereas if one considers the colloidal aggregate in isolation, it behaves as if it is being held at fixed pressure (the depletant osmotic pressure). One might expect a high degree of similarity between the self-assembled structures of colloids in the presence of depletants at constant volume and monodisperse colloids at constant pressure. Indeed, given this equivalence, it makes it more reasonable to expect that our methods below would apply in both cases [8]. Our approach below is an instance of the two-particle version of this argument.

There has been considerable focus on the contribution of entropic forces to the assembly of anisotropically shaped particles into complex structures [49, 50, 55–72]. A general observation from many of these studies is that dense suspensions of hard, faceted particles

align their facets so as to maximize the system entropy, giving rise to ordered structures as complex as colloidal quasicrystals [57, 63] and crystals with unit cells containing as many as 52 particles [64]. Damasceno, *et al.* [63, 64] rationalized this tendency toward facet alignment as the emergence of "directional entropic forces" between hard particles. Directional entropic forces (DEFs) are not intrinsic to the particles, but instead are statistical and emerge from the collective behavior of the entire system upon crowding. The DEF approach to the self-assembly of colloidal cubes, octahedra, rhombic dodecahedra, and tetrahedra was recently demonstrated by Young *et al.* [123].

In summary, the osmotic pressure arising from entropy is the principle behind the ordering of hard particles regardless of their shape, relative size, or the relative repulsion of the depletants.

3.3 Potential of Mean Force and Torque

We use the concept of the potential of mean force and torque in order to establish the interaction between neighboring particles. Though this has been developed before in [112, 124, 125], we would like to present these ideas in such a way as to clarify the role of the entropic patches.

To begin, consider the case of a pair of colloidal particles interacting via depletion. For the sake of simplicity we work in the hard particle limit for the colloidal particles and the penetrable hard sphere limit for the depletants, i.e. the depletants are hard with respect to the colloidal particles, but an ideal gas with respect to each other. The microcanonical partition function for our system is

$$\mathcal{Z} \propto \int [dq][dQ][dr]\ 1\ , \tag{3.1}$$

where q are the colloid center of mass coordinates, Q are the colloidal orientational degrees of freedom, and r are the depletant centers of mass. The integral is over all configurations that do not lead to colloid-colloid or colloid-depletant overlaps. We will focus on a single pair of axisymmetric colloidal particles in a bath of depletants. To find the potential of mean force and torque between the colloidal particles we will find a set of invariant quantities that describe unique configurations of the colloidal particles and compute the partition function in restricted ensembles in which those quantities are fixed. There are ostensibly twelve colloidal degrees of freedom, however six may be fixed by fixing the position and orientation of one of the particles, and two more are fixed by the axial symmetries. Only four degrees of freedom are required to uniquely specify a configuration of the two colloids

and they can be taken as

$$\{|\vec{q}_{12}|, \hat{q}_{12}\cdot\hat{n}_1, -\hat{q}_{12}\cdot\hat{n}_2, -\hat{n}_1\cdot\hat{n}_2\}\,, \tag{3.2}$$

where $\vec{q}_{12} = \vec{q}_2 - \vec{q}_1$ is the vector between the colloidal centers of mass, and $\hat{n}_{1,2}$ are their symmetry axes. We define the restricted partition function

$$\begin{aligned}\mathcal{Z}(R,\phi_1,\phi_2,\chi) \equiv \int [dq][dQ][dr]\; \delta(R-|\vec{q}_{12}|)\delta(\phi_1 - \hat{q}_{12}\cdot\hat{n}_1) \\ \delta(\phi_2 + \hat{q}_{12}\cdot\hat{n}_2)\delta(\chi + \hat{n}_1\cdot\hat{n}_2)\,,\end{aligned} \tag{3.3}$$

from which we derive an effective potential

$$\begin{aligned}\beta U(R,\phi_1,\phi_2,\chi) \equiv -\log\int [dq][dQ][dr]\; \delta(R-|\vec{q}_{12}|)\delta(\phi_1 - \hat{q}_{12}\cdot\hat{n}_1) \\ \delta(\phi_2 + \hat{q}_{12}\cdot\hat{n}_2)\delta(\chi + \hat{n}_1\cdot\hat{n}_2)\,.\end{aligned} \tag{3.4}$$

This effective potential can be evaluated in a number of ways. In this work, we will perform the integral by doing a change of variables to R, $\phi_{1,2}$, and χ, and then doing a Monte Carlo integration over the depletant coordinates. We find that the restricted partition function (3.3) can be written as

$$\mathcal{Z}(R,\phi_1,\phi_2,\chi) = \frac{R^2 V_F^N}{\sqrt{1-\chi^2-\phi_1^2-\phi_2^2-2\phi_1\phi_2\chi}}\,, \tag{3.5}$$

where V_F is the free volume available to the depletants, which is given by

$$V_F = V - \eta V_{\text{colloid}} + V_{\text{overlap}}\,, \tag{3.6}$$

where η is the colloidal packing fraction and V_{overlap} is the depletant overlap volume. For a large system

$$V_{\text{overlap}} \ll V - \eta V_{\text{colloid}}\,, \tag{3.7}$$

which means we can expand the expression for the potential of mean force to find that, up to an irrelevant overall additive constant,

$$U(R,\phi_1,\phi_2,\chi) = -PV_{\text{overlap}} - kT\log\left(\frac{R^2}{\sqrt{1-\chi^2-\phi_1^2-\phi_2^2-2\phi_1\phi_2\chi}}\right), \tag{3.8}$$

where we have used the ideal gas equation of state.

The expression (3.8) for the potential of mean force, for this case, is instructive for a few reasons. In particular, we can see that it is the sum of two terms that are both purely entropic and geometric in origin. The first term comes from the geometry of the colloidal particles, and therefore determines their effective "patchiness" [8]. The second term comes from the entropy of available to other free particles in the system. The "binding" of colloidal particles along different distances and orientations is determined, therefore, by a competition between these two terms.

The expression (3.8) was arrived at by integrating out the depletant positions exactly. In more general systems such an exact integration cannot be performed. Yet even in those cases, formally, the potential of mean force and torque factorizes into two terms carrying the same geometric information as in the depletant case.

To compute this potential for our systems with depletants we enumerate allowed configurations of the coordinates R, $\phi_{1,2}$, and χ, and compute V_{overlap} by Monte Carlo integration at each set of values. We could also have done this using Markov chain Monte Carlo, however there are a couple of calculational advantages to this approach. One is that we can compute the effective potential at all depletant pressures and temperatures at once. Another is that it can be shown that the depletant volume lies entirely within a lens formed by the intersection of spheres that are centred about the colloid centers of mass and that have radii equal to the sum of the radii of the respective circumscribing sphere of the particle and that of the depletant. This leads to a substantial reduction in required computational effort.

3.4 Coordinate Systems for PMFT: Axisymmetric case

We present an explicit computation of the Jacobian of the change of variables between the natural coordinates of a pair of particles, and the scalar invariant quantities that describe any such pair. We do so in the simpler case of axisymmetric particles. The general case can be computed straightforwardly in the same manner, but the expressions are cumbersome.

We take the first particle to be at the origin, with its symmetry axis oriented in the positive z direction. Using the azimuthal symmetry with this placement, we fix the second particle's position in the xy-plane, without loss of generality to be along the x axis. This gives the orientation of the second particle as

$$\hat{n}_2 = \sin\theta\cos\varphi\hat{x} + \sin\theta\sin\varphi\hat{y} + \cos\theta\hat{z} \tag{3.9}$$

where θ and φ are spherical coordinates in the coordinate system of the second particle, and

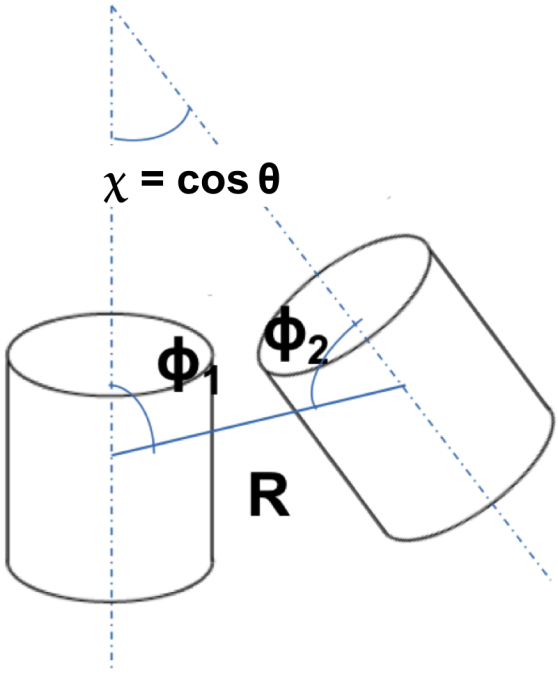

Figure 3.2: Geometric representation of the coordinate transformation for axi-symmetric particles in the case of true cylinders.

its position as

$$r_2 - r_1 = \rho\hat{x} + z\hat{z} \tag{3.10}$$

where ρ and z are cylindrical coordinates in the first particle's coordinate system. The volume form that appears in the integral that computes the partition function is

$$dV = \rho \sin\theta d\rho dz d\theta d\varphi \tag{3.11}$$

Now we make the change of variables to the scalar invariant quantities by taking

$$\begin{aligned} R &= \sqrt{z^2+\rho^2} \\ \phi_1 &= \frac{z}{\sqrt{z^2+\rho^2}} \\ \phi_2 &= -\frac{\rho\sin\theta\cos\varphi + z\cos\theta}{\sqrt{z^2+\rho^2}} \\ \chi &= -\cos\theta \end{aligned} \tag{3.12}$$

Inverting the relationship between the two coordinate systems gives

$$\begin{aligned}
\rho &= R\sqrt{1-\phi_1^2} \\
z &= R\phi_1 \\
\theta &= -\cos^{-1}\chi \\
\varphi &= \cos^{-1}\left(\frac{-\phi_1\chi-\phi_2}{\sqrt{(1-\chi^2)(1-\phi_1^2)}}\right)
\end{aligned} \tag{3.13}$$

The computation of the Jacobian is simplified by noting the dependence of ρ and z on only R and ϕ_1, and θ on only χ. This means that we only need to consider the dependence of φ on ϕ_2. Taking the Jacobian of this leads to the new volume form

$$dV = \frac{R^2 dR d\phi_1 d\phi_2 d\chi}{\sqrt{1-\chi^2-\phi_1^2-\phi_2^2-2\phi_1\phi_2\chi}} \tag{3.14}$$

In the absence of the excluded volume (or other) interaction between the particles, this expression measures the volume of configuration space available to a pair of free particles in a particular translationally and rotationally invariant configuration.

To verify that our expression correctly encodes the density of states for two free axisymmetric particles, we consider the following scenario. Suppose we had a pair of axisymmetric particles each undergoing Brownian motion with the constraint that their centers of mass could never be separated by a distance greater than $R_{\max}$, but that they were otherwise free to move, including to interpenetrate. If we were to make some N_{obs} uncorrelated observations of the particles for each of which we determine the values of R, ϕ_1, ϕ_2, and χ, we would find that their frequency distribution would converge to something proportional to the Jacobian of our coordinate transformation in the limit that $N_{\text{obs}} \to \infty$. We therefore verified our expression by performing precisely this calculation.

3.5 PMFT Calculations with Depletant Particles

In Fig. 3.3, we show these calculations for a Pacman model system. We observe that in the case of lock-key binding, the effective interaction potential between two Pacman particles is very strong and directional. In comparison, non-specific interactions are $\approx 10k_BT$ weaker and can occur over a large range of orientations between the particles. From this observation, we understand that non-specific interactions form and break easily in comparison to

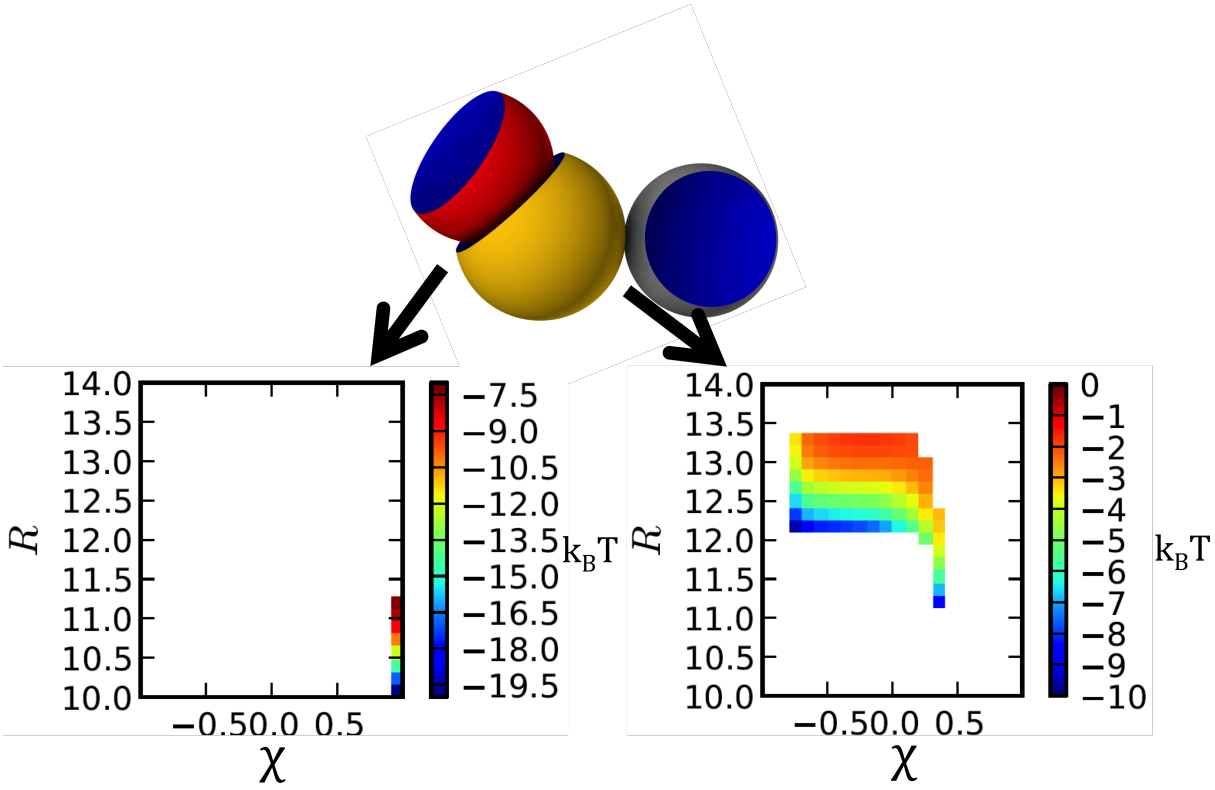

Figure 3.3: Potential of mean force and torque calculations in a Pacman model system. We see that the interactions between two Pacman particles are very strong and directional in the case of lock-key binding (left), while non-specific interactions can occur over a large number of orientations between the particles.

specific interactions. This suggests that non-specific interactions can function as a route to specific binding in these systems.

In Fig. 3.4, we plot this potential to compare the effect of different particle shape features. This figure compares the potential of mean force and torque at a fixed value of the temperature and pressure for a rounded cylinder and a true cylinder (see Fig. 3.2 for a depiction of the geometric understanding of the coordinates and top panel of Fig. 3.4 for a depiction of the rounded cylinders themselves). We define a rounded cylinder of diameter d_c with rounding of diameter d_r as the Minkowski sum of a cylinder of diameter $d_c - d_r$ and a sphere of diameter d_r. The plots show that there is a deeper potential well in the case of the true cylinder $d_r = 0$ that comes from the larger entropic patch at its end compared to the case of the rounded cylinder, in which $d_r/d_c = 4/5$.

From our expression for the potential of mean force and torque we can derive the forces and torques acting on the particles. Between two particles one and two, we find that for particle one they have the following form, without loss of generality:

$$\begin{aligned} F_1 &= -\hat{r}_{12}\frac{\partial U}{\partial R} - (\hat{n}_1 - \hat{r}_{12}\phi_1)\frac{\partial U}{\partial \phi_1} - (\hat{n}_2 + \hat{r}_{12}\phi_2)\frac{\partial U}{\partial \phi_2}\,, \\ T_1 &= -\hat{r}_{12}\times\hat{n}_1\frac{\partial U}{\partial \phi_1} + \hat{n}_2\times\hat{n}_1\frac{\partial U}{\partial \chi}\,. \end{aligned} \tag{3.15}$$

A further remark is in order. As can be seen in equation (3.8) the potential of mean force and torque is comprised of two terms both entirely geometric and entropic in origin: one comes from the entropy of the depletants, the other from the Jacobian of the transformation to invariant coordinates. At different thermodynamic state points these terms will have different relative contributions. This leads to a competition between the free particle entropy of the pair (the jacobian) and the entropy coming from the effective interaction of the patches. (see appendix A for details.

3.6 Binding Specificity of True Cylinders

We computed the potential of mean force and torque for a model system above and showed that it produced potential depths of several $k_B T$ at specific patch sites. In this section we show that even in the case of small effective entropic patches, we can cause preferential binding at patch sites through adjusting their strength by tuning the osmotic pressure of depletants..

To show this explicitly, we integrate the potential of mean force and torque over a set of coordinates for the pair of particles that correspond to the same qualitative binding con-

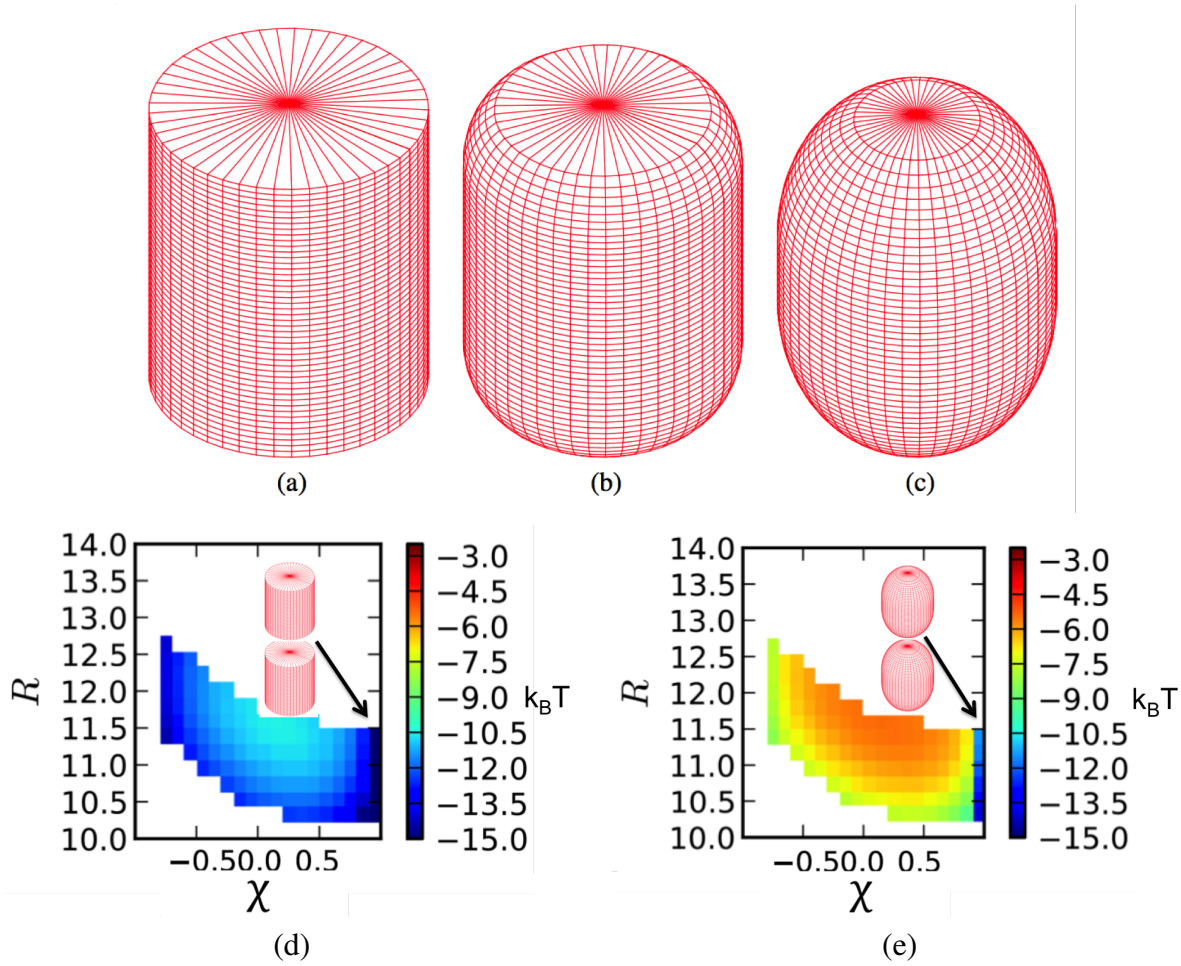

Figure 3.4: (Top) Cylinders with various degrees of rounding. Panel (a) shows a true cylinder. Panel (b) shows a rounded cylinder in which the ratio of the radius of the rounding to the radius of the cylinder is rounding $d_r/d_c = 2/5$. Panel (c) shows a rounded cylinder with $d_r/d_c = 4/5$. (Bottom) Potential of mean force and torque calculations for true cylinder (e) and cylinder with rounding $d_r/d_c = 4/5$. The true cylinder leads to a more highly anisotropic interaction potential with a deeper minimum near facial alignment than the rounded cylinder.

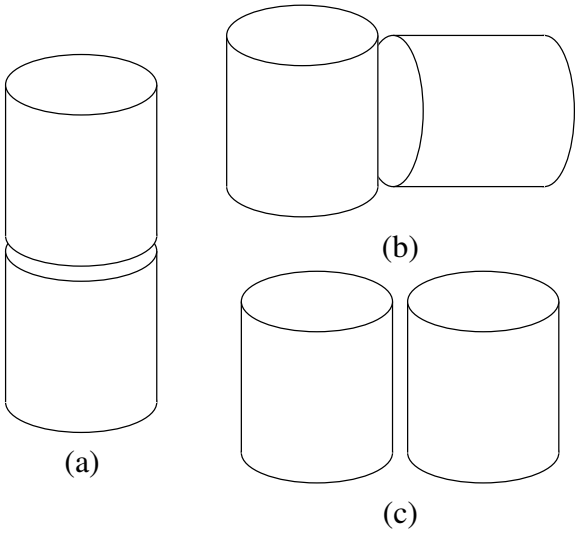

Figure 3.5: Examples of specific (a), semi-specific (b), and non-specific (c) binding configurations for a pair of colloidal cylinders.

figuration. For concreteness, let us consider the case of cylinders with equal diameter and height. We will define specific binding configurations that have non-zero depletant overlap volume in which the cylinders are end-to-end, non-specific binding as cases in which the cylinders are side-by-side, and semi-specific binding as cases in which the cylinders are end-to-side. See figure 3.5 for an illustration.

Formally, we find the probability of specific binding is proportional to

$$\begin{aligned}\mathcal{Z}_s \propto &\int_{\frac{1}{\sqrt{2}}}^{1} d\phi_1 \int_{\frac{1}{\sqrt{2}}}^{1} d\phi_2 \int dR \int d\chi e^{-\beta U(R,\phi_1,\phi_2,\chi)} \theta(-\beta P V_F) + \\ &\int_{-1}^{-\frac{1}{\sqrt{2}}} d\phi_1 \int_{-1}^{-\frac{1}{\sqrt{2}}} d\phi_2 \int dR \int d\chi e^{-\beta U(R,\phi_1,\phi_2,\chi)} \theta(-\beta P V_F) \, .\end{aligned} \tag{3.16}$$

We can evaluate this integral using our computation of the potential of mean force and torque above.

In figure 3.6 we plot the probability of specific binding for a family of rounded cylinders as a function of pressure. We see that as the amount of cylinder rounding decreases, the pressure required to induce specific bonding also decreases. This means that the entropic patch becomes stronger as its size increases, meaning that we can tune the interaction strength between our entropic patches by simply adjusting their size. Note that even at very small patch size, at sufficiently high depletant pressure, specific binding still occurs with unit probability.

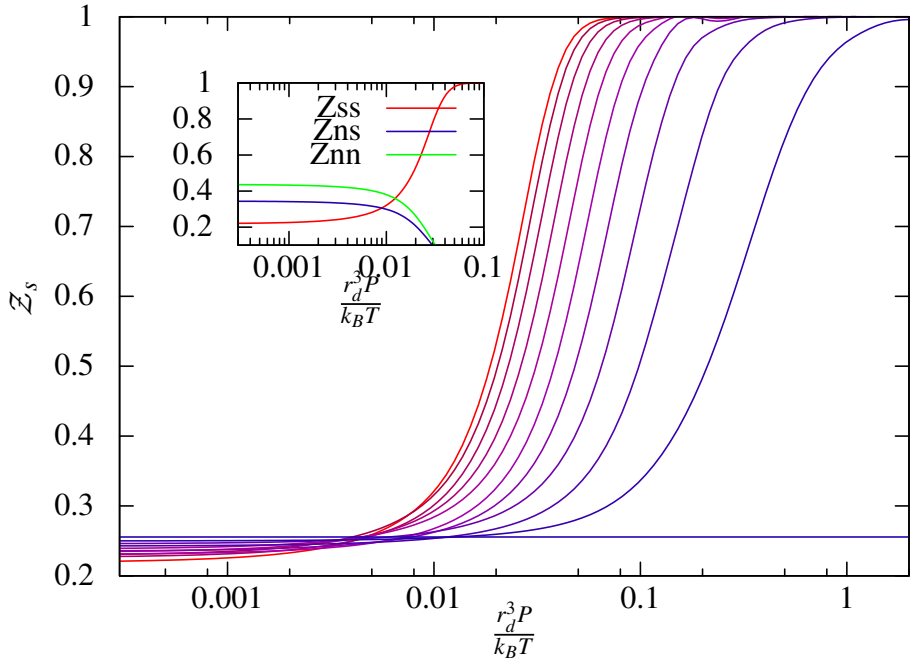

Figure 3.6: The probability of specific, i.e. end-to-end, binding between rounded cylinders as a function of depletant osmotic pressure for different amounts of rounding. We interpolate between a sphere (rounding of 1, blue curve) and a true cylinder (rounding of 0, red curve); in the latter case the diameter of the cylinder is the same as its height. In all cases the maximum radius of a sphere that can be inscribed within the shape is fixed to ten times the radius of the depletant. See figure A.1 for a depiction of the rounded cylinders themselves. Figure reproduced from [8].

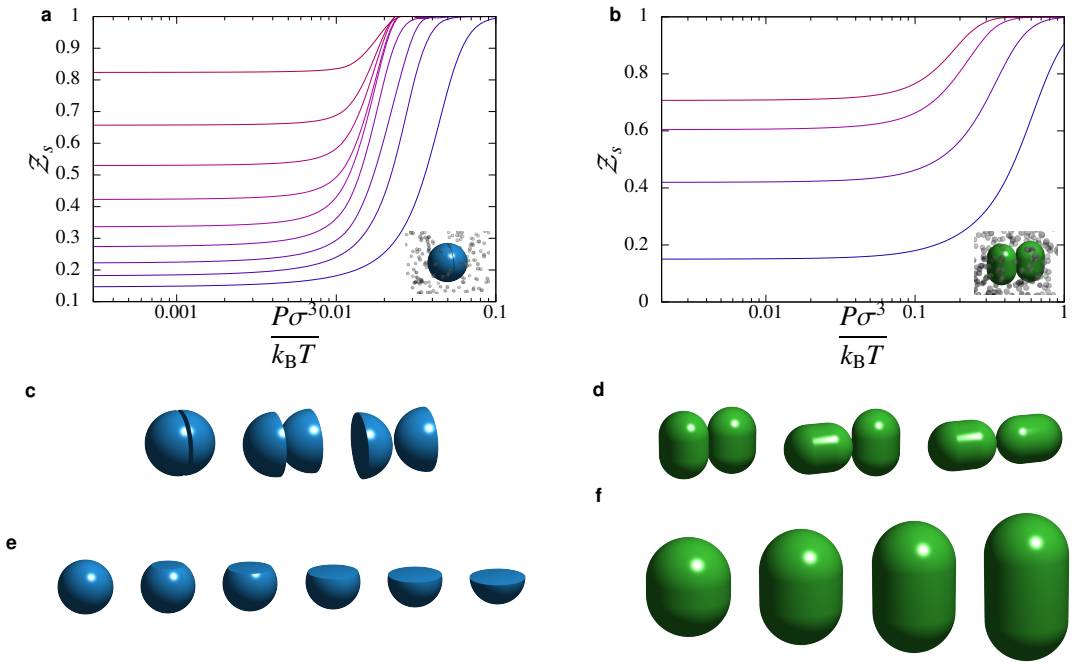

Figure 3.7: The probability of specific binding for (a) particles with a single facet, and (b) capsules, in a bath of depletants at various pressures. Panels (c) and (d) depict configurations that correspond to specific, semi-specific, and non-specific binding according to whether the binding occurs at sites of low curvature. Panels (e) and (f) show singly facetted spheres and spherocylinders with various facet and cylinder sizes, respectively. Curves in (a) and (b) show the probability of specific binding at various facetting amounts. Figure reproduced from [8].

3.7 Facetted Spheres and Facetted Capsules

We study DEFs as a function of the colloid shape in two systems with conventional weakly interacting, small depletants. One system consists of a pair of spherical particles that are continuously facetted with a single facet, in order to promote locally dense packing. The other is a system of spherocylinders of constant radius that are continuously elongated. In each case the alteration creates a region on the surface of the particle with reduced spatial curvature. As the amount of alteration to particle shape increases, it leads to stronger attraction between the sites of the reduced curvature, sites with smaller deviation from being flat, as encoded in the probability of observing particles with these sites adjacent. Following [3] we identify such sites as entropic patches.

In the case of the facetted particle, we varied the depth of the facet linearly between zero (a sphere) and unity (a hemisphere), with the radius of the sphere fixed to 10 (see Fig. 3.7e). In the case of the particles with a band, we studied spherocylinders with cap radii fixed to 5 and cap centers interpolating linearly between 1 (nearly spherical) and 4

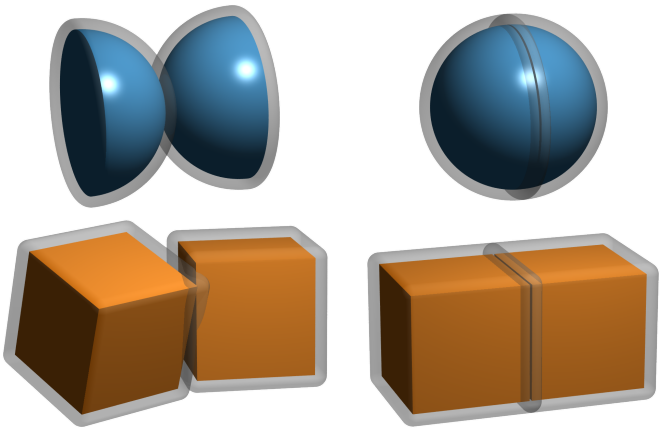

Figure 3.8: The effective entropic interaction between particles generates both forces and torques, because the volume excluded to the rest of the system when the particles are fixed at separation distance depends on their relative orientation.

(an elongated spherocylinder), where all lengths are in units of the depletant radius (see Fig. 3.7f). In Fig. 3.7 a and b we show the probability that if a pair of particles is bound, then they are bound patch-to-patch (specific binding). Specific binding is depicted in the inset images and the left hand particle pairs in panels c and d, and is contrasted with patch-to-non-patch (semi-specific binding), and non-patch-to-non-patch (non-specific binding) in the center and right hand particle images in panels c and d. Panels a and b show that we can tune binding specificity by adjusting the patch size and the depletant pressure. Different curves correspond to increasing patch size (more facetting) as the color goes from blue to red.

3.8 Forces and Torques

For concreteness, we give an example for how to compute the forces and torques from the PMFT for axisymmetric particles.

The isotropy of the stress tensor does hold in the case of idealized depletant systems. Suppose we have N depletant particles. In this case, we can explicitly evaluate the free energy available to the rest of the system, $\tilde{F}_{12}(\Delta\xi_{12})$, in Eq. (3.8).

$$e^{-\beta\tilde{F}_{12}(\Delta\xi_{12})} \propto V_{\mathrm{F}}(\Delta\xi_{12})^{N}\,, \tag{3.17}$$

where V_{F} is the volume available to the depletants. If we consider two nearby configura-

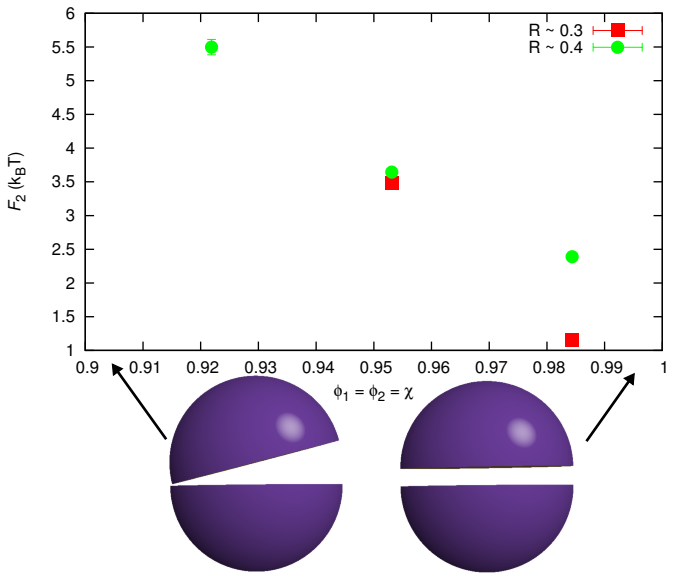

Figure 3.9: The χ dependence of the PMFT for facetted spheres in the presence of penetrable hard sphere depletants at different distances between their centers, for a slice of the potential with $\Psi \equiv \phi_1 = \phi_2 = \chi$ fixed. Although the angular differences are small (perfect alignment is $\Psi = 1$), the effective interaction varies by more than 2 k_BT over this angular range at small separations, indicating that the penalty for small misalignment is significant. Inset particle images illustrate the relative orientations shown.

tions, we have that

$$\begin{aligned}\beta(F'_{12} - F_{12}) =& V' - V - N\log\left(\frac{V'_{\mathrm{F}}}{V_{\mathrm{F}}}\right) - \log J' + \log J \\ \approx& V' - V - \beta P(V'_{\mathrm{F}} - V_{\mathrm{F}}) + \log J' - \log J \,,\end{aligned} \tag{3.18}$$

where we have used the ideal gas equation of state for the depletant particles. Thus, up to an irrelevant additive constant

$$\begin{aligned}\beta F_{12}(\Delta\xi_{12}) =& \beta V(\Delta\xi_{12}) - \beta P V_{\mathrm{F}}(\Delta\xi_{12}) \\ & - \log J(\Delta\xi_{12}) \,.\end{aligned} \tag{3.19}$$

This is the generalization of the Asakura-Oosawa [73] result for depletion interactions between spherical particles to particles of arbitrary shape. Depending on the relative position and orientation of the particles, the effective force between them will be different.

In Fig. 3.9, we show the χ dependence of the PMFT for facetted spheres in the presence of penetrable hard sphere depletants at different distances between their centers. This angular specificity achieved by facet alignment *via* DEFs is reminiscent of the angular specificity of enthalpic interactions conceptualized within the patchy particle paradigm [2, 21].

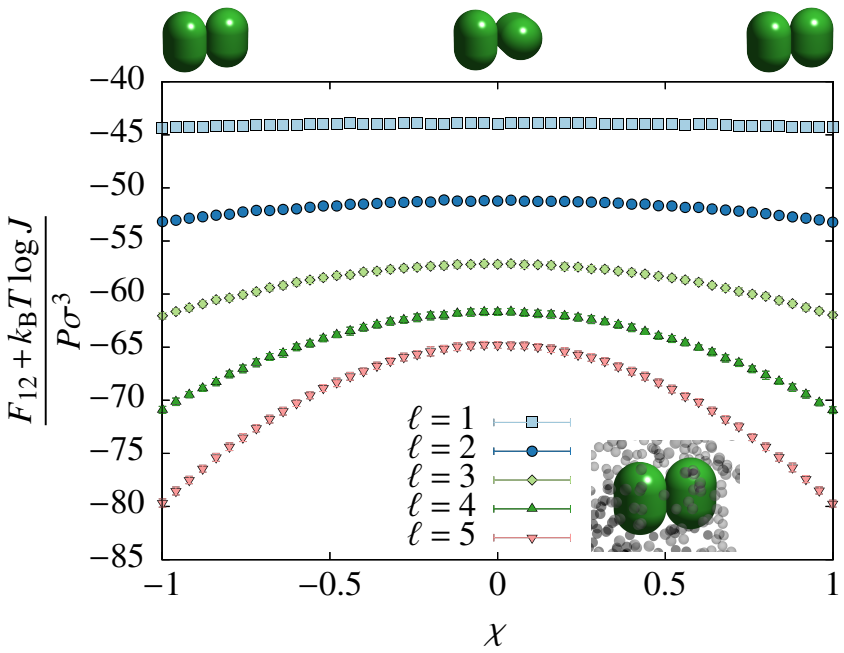

Figure 3.10: The χ dependence of the PMFT for spherocylinders in the presence of penetrable hard sphere depletants for different cylinder side lengths. As the side length, ℓ, increases from 1 to 5 (in units of the depletant radius), the amount of dependence on χ increases, indicating greater torques, as expected.

For spherocylinders, it is straightforward to show the effect of the entropic patches in generating torques that cause the particles to align. To isolate the part of the torque that comes from the patch itself, we rearrange Eq. (3.19) for non-overlapping spherocylinders to get

$$\frac{F_{12}+k_BT\log J}{P\sigma^3} = -\frac{V_F}{\sigma^3} \tag{3.20}$$

For clarity, we fix the separation distance R between the spherocylinders to be 1% larger than the spherocylinder diameter (which is the minimum separation distance), and fix the orientation of each spherocylinder to be normal to the separation vector between them ($\phi_1 = \phi_2 = 0$). In Fig. 3.10 we plot the χ dependence of the PMFT. For small side lengths of the spherocylinder, there is very weak dependence of the PMFT on χ. As the length of the cylinder increases (and therefore as the entropic patch gets larger) the χ dependence of the PMFT becomes more pronounced. This means that not only do the particles coordinate at their entropic patch sites, but there exists a torque that causes the alignment of the patches.

To compute the torques, we find it convenient to work in terms of rotation matrices in the spin $\frac{1}{2}$ representation of $SU(2)$. If $\mathbf{q}$ is the rotation, then to determine the torque, we must differentiate the PMFT with respect to it. If we represent the rotations in the canonical fashion, and use Pauli matrices as the basis vectors of the Cartesian space coordinates, then

we have scalar products of the form

$$\vec{a} \cdot \vec{b} = \frac{1}{2} \mathrm{Tr}(a^\dagger b) \tag{3.21}$$

and cross products of the form

$$\vec{a} \times \vec{b} = \frac{1}{2i}[a, b] \tag{3.22}$$

Our potential depends on scalar products alone. That means to determine the torque we are required to know, e.g. that if

$$\phi_1 = \frac{1}{2} \mathrm{Tr}(\mathbf{q}^\dagger \hat{z} \mathbf{q} \hat{r}_{12}) \tag{3.23}$$

then

$$\frac{\partial \phi_1}{\partial \mathbf{q}} = \frac{1}{2} \mathbf{q}^\dagger \left[\mathbf{q} \hat{r}_{12} \mathbf{q}^\dagger, \hat{z} \right] \tag{3.24}$$

which we recognize as a cross product. We have taken, without loss of generality, the reference vector to be $\hat{z}$ in the coordinate frame of the particle. We then use the chain rule to differentiate F_{12} with respect to $\mathbf{q}$, and convert back to Cartesian coordinates to find a contribution to the torque of the form

$$\vec{T}_{\phi_1} = -\hat{r}_{12} \times \hat{n}_1 \frac{\partial F_{12}}{\partial \phi_1} \tag{3.25}$$

Similar manipulations yield the other contributions.

3.9 Extension of PMFT Methods for Penetrable Hard Sphere Depletants

The results we obtained via free volume calculations with ideal depletants can also be obtained via simulations with explicit depletants. To see why the two forms of computation are equivalent, we consider the following situation. Again, for the sake of simplicity, we will work in the penetrable hard sphere limit. The probability of accepting a trial Monte Carlo move of our colloidal particle is given by

$$p_a = (1 - p)^N \tag{3.26}$$

where N is the number of depletants, and p is the probability that a depletant will be in the region swept out by the particle during its move. In the limit in which we are working, this

is given by

$$p = \frac{\Delta V_{\text{sweep}} - \Delta V_{\text{overlap}}}{V_{\text{F}}} \tag{3.27}$$

where V_{F} is the free volume available to the depletants, ΔV_{sweep} is the volume swept out by the colloid during move, and $\Delta V_{\text{overlap}}$ accounts for any increase in the depletant overlap volume.

In the limit that the move is small, i.e. $Np \ll 1$, the probability of accepting the move is

$$p_a \approx 1 - \frac{N(\Delta V_{\text{sweep}} - \Delta V_{\text{overlap}})}{V_{\text{F}}} \tag{3.28}$$

which gives the probability of rejecting such a move as

$$p_r \approx \frac{N(\Delta V_{\text{sweep}} - \Delta V_{\text{overlap}})}{V_{\text{F}}} \tag{3.29}$$

We can, similarly, find the probability of rejecting a reverse move. That is given by

$$p'_r \approx \frac{N(\Delta V_{\text{sweep}})}{V_{\text{F}} + \Delta V_{\text{overlap}}} \approx \frac{N\Delta V_{\text{sweep}}}{V_{\text{F}}}\left(1 - \frac{\Delta V_{\text{overlap}}}{V_{\text{F}}}\right) \tag{3.30}$$

where we have assumed that, without loss of generality, the "forward" move causes an increase in the depletant overlap volume, and the reverse move causes it to decrease. We have again also used the fact that the size of the move is small.

We compute the difference in probability for the two moves

$$\Delta p \equiv p'_r - p_r \approx \frac{N\Delta V_{\text{overlap}}}{V_{\text{F}}}\left(1 - \frac{\Delta V_{\text{sweep}}}{V_{\text{F}}}\right) \approx \frac{N\Delta V_{\text{overlap}}}{V_{\text{F}}}\,. \tag{3.31}$$

We can now consider another pair of moves in which the initial configuration of the forward move is identical to the situation just described, but the final configuration is different. If in that case the change in overlap volume is $\Delta V'_{\text{overlap}}$, then the probability difference is

$$\Delta p' \approx \frac{N\Delta V'_{\text{overlap}}}{V_{\text{F}}} \tag{3.32}$$

From these quantities we can compute the ratio $\Delta p/\Delta p'$, which is dependent only on the free volume, which, in turn, is encoded in our potential of mean force and torque. We get that

$$\frac{\Delta p}{\Delta p'} = \frac{\Delta V_{\text{overlap}}}{\Delta V'_{\text{overlap}}} \tag{3.33}$$

which means we can write

$$\frac{\Delta p}{\Delta p'} = \frac{F_{12}^{\text{post}} - F_{12}^{\text{pre}}}{F_{12}^{\text{post}\prime} - F_{12}^{\text{pre}}} \tag{3.34}$$

in the limit that $T \to 0$. From this expression we see that the PMFT we deduced from the free volume calculation is precisely quantity that controls the average acceptance rate of MC moves of the colloids in a simulation with explicit depletants. Hence results obtained from the free volume methods used above will precisely match those obtained using much more expensive MC simulations with explicit ideal depletants.

3.10 Extension of PMFT Methods to Hard Particle Systems

In many ways, the depletion effect for small depletants shown by Asakura and Oosawa is similar to the nematic ordering of hard rods shown by Onsager: the restriction of some specific degrees of freedom in the system (i.e. ordering) through the creation of a hierarchy of length scales. Onsager's rods have two length scales (the length and diameter of the rod) and Asakura-Oosawa's binary system consists of two species of spheres with different diameters. The techniques used to demonstrate the ordering in the two systems were different. Onsager used integral equations to examine coarse-grained densities of the rod distribution (as did Kirkwood with spheres), whereas Asakura and Oosawa considered effective pair interactions between two colloidal particles in a sea of depletants. However, de Boer [104] (and later also Vrij [74]) also considered similar systems to Kirkwood's hard spheres, but from an effective pair interaction approach, similar to that used in the later work of Asakura and Oosawa for colloid-polymer mixtures, and thereby providing a microscopic description of the mechanism underlying the ordering of hard spheres.

In summary, the osmotic pressure arising from entropy is the principle behind the ordering of hard particles regardless of their shape, relative size, or the relative repulsion of the depletants. Of course, details differ from system to system. However, the notion of DEFs suggested for monodisperse hard particle systems in [63] applies to a broad class of colloidal systems that includes polydisperse systems that would be classified as traditional depletion, because, as shown in [8], the mechanism is insensitive to those details.

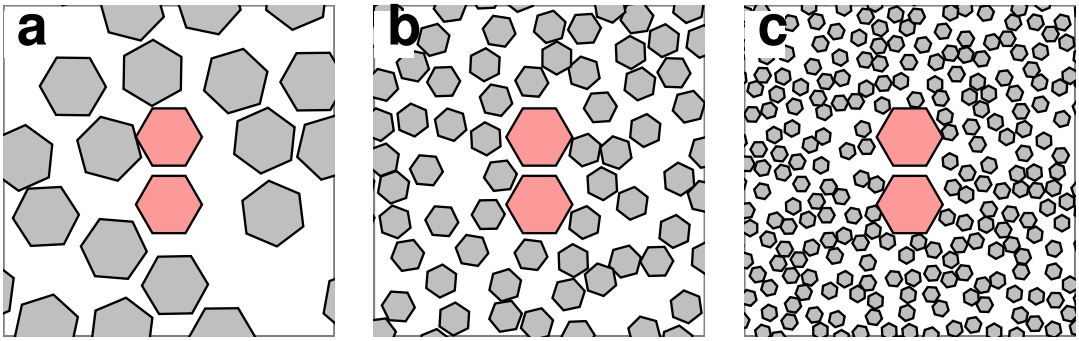

Figure 3.11: As the size ratio of the particle pair of interest (pink) to the surrounding particles (grey) in a hard particle system is varied between unity in a monodisperse hard particle system (a) much greater than unity in a binary hard system (c) through intermediate sizes (b), the system goes from a monodisperse system, to one that begins to resemble a conventional "depletion" system.

3.11 Discussion

We have shown that by changing the shape of colloidal particles we can create effective entropic patches that lead to binding in specific configurations. We verified this effect in a number of simple situations using a variety of axisymmetric shapes. We quantified the effect of the entropic patches through the potential of mean force and torque, which provides a detailed quantitative measure of the directional entropic force that leads to particle binding. By focusing on a pair of particles and formally integrating out the other degrees of freedom we explicitly cast this in terms of a competition between the osmotic effect of the particles that were integrated out and the entropy of the pair of free particles, clarifying the role of the entropic patch. By tuning the patch size and the osmotic pressure we showed that we were able to control the specificity of the binding.

We first considered a pair of colloidal particles in a bath of depletants. This provided us with a simple system in which to verify the effect of the entropic patches in detail. In [8], we also consider model hard particle systems and demonstrate quantitatively similar results, confirming that entropic patches play a role in that system as well.

We computed the strength of the effective entropic interaction between colloidal particles in the presence of depletants in our example systems, and found it to be on the order of several $k_{\mathrm{B}}T$. This establishes that depletants can be used to promote entropic patchiness for assembling materials. Moreover, the methods we have described here also provide a means of quantifying the relative effect of shape on assembly in systems where other forces are also at play. One could imagine developing reconfigurable materials in which particles are

patterned both with shape, and some sort of hydrophobic coating in different symmetric patterns, and this could lead to materials that microscopically reconfigure as the depletant concentration in the system is varied.

One of the key conceptual features of the entropic effect that distinguishes it from particles that have conventional energetic patches is that the forces between colloidal particles are emergent, i.e. they arise only when the system has a finite number of depletants, equivalent to an osmotic pressure. As we've been taught, more is different [126], and we believe entropic patches are an interesting example of this for a number of reasons. From a fundamental point of view, it is interesting to design materials from particles that only experience a force when they are among particles of the right sort, and under sufficient pressure. Yet if more is different, then less is also different: our colloidal particles only experience emergent forces. This could be of use from a practical point of view as particles with entropic patches could be used to make materials of novel complexity without requiring the introduction of heavy metals or organic moieties that would lead to environmental damage if the products they are in become damaged or are improperly disposed of. Indeed, Ref. [62] created particles with interesting shape that were plain old silica.

CHAPTER 4

Depletion Driven Self-Assembly of Facetted and Dimpled Particles

4.1 Introduction

In this chapter, we consider concave shape transformations to model particles starting from spheres. Such single dimple particles have been studied in various contexts, including the assembly of spherical caps [102, 127], bowls [99, 100], lenses [101], lock-and-key dynamics [86], and ferroelectric liquid crystals [128]. These particles also hold the promise of being good candidates for the entropic assembly of complex structures using shape complementarity, an idea that has been both theoretically studied [87, 88, 129] and experimentally demonstrated [86, 130] as an alternative to enthalpy-driven assembly achieved through, for e.g., complementary DNA binding[1].

Here, we introduce control on specific binding through shape transformations on concave features of colloidal particles [8]. Functional materials in nature self-assemble into complex structures through highly specific and selective binding among molecular building blocks. To harness similar functionality from colloidal materials, patchy particles [2, 21] use, for e.g., selectively modified surface chemistry [21, 131], including hydrophobic-hydrophilic interactions [132, 133] or DNA functionalization of the surface [134, 135]. Simulation has already shown [63, 64] that various complex structures can be obtained from convex entropically patchy particles of different shapes [3]. Entropy drives the ordering of these systems through emergent directional entropic forces, causing the particles to assume local dense packing motifs that repeat throughout the system [8].

Investigations of colloid shape have primarily focused on convex polyhedra due to their geometric simplicity and the availability of synthesis techniques [46, 86]. A general observation from many of these studies is that dense suspensions of hard, facetted particles align

[1]This chapter contains work that comprises a manuscript in preparation by N. K. Ahmed, J. Glaser, G. van Anders and S. C. Glotzer.

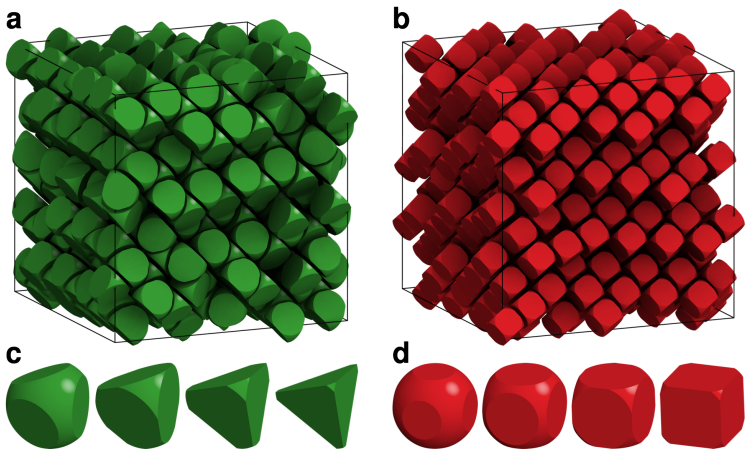

Figure 4.1: Self-assembled structures of facetted spheres obtained in MC simulation by designing particle shape. Panel (a) shows a diamond lattice obtained by giving a particle tetrahedrally coordinated facets as in (c). Panel (b) shows a simple cubic lattice, obtained by giving particles cubically coordinated facets as in (d).

their facets so as to maximize the system entropy, giving rise to ordered structures as complex as colloidal quasicrystals [57,63] and crystals with unit cells containing as many as 52 particles [64]. Damasceno, *et al.* [63,64] rationalized this tendency toward facet alignment as the emergence of "directional entropic forces" between hard particles, as shown in Fig 4.1. Directional entropic forces (DEFs) are not intrinsic to the particles, but instead are statistical and emerge from the collective behavior of the entire system upon crowding. The DEF approach to the self-assembly of colloidal cubes, octahedra, rhombic dodecahedra, and tetrahedra was also demonstrated by Young *et al.* [123].

Motivated by the ability to promote specific binding using concave shape transformations, we study a family of single feature particles where the valence sphere radius is continuously varied from a flat facet (radius = infinity) to a perfect dimple (radius = one), as shown in Fig. 4.2 (a). Specifically, we probe the binding configuration of a pair of particles in the presence of penetrable hard sphere depletants of different sizes by calculating the available free volume. We limit the particles to the configuration where the feature, i.e. valence sphere, always intersects with the parent sphere along its diameter, as shown in Fig. 4.2 (b). Intuitively, we understand that directional entropic forces will vary from "head-to-head" binding, where facets or dimples align, to "head-to-tail" binding, where facets or dimples "align" with the convex feature of the neighboring particle, as we increase the concavity of the particles, as shown in Fig. 4.2 (a). This effect can be calculated geometrically by understanding the excluded volume available to depletants. Here, we study the effect of depletant size on binding for a pair of these particles. By measuring the available

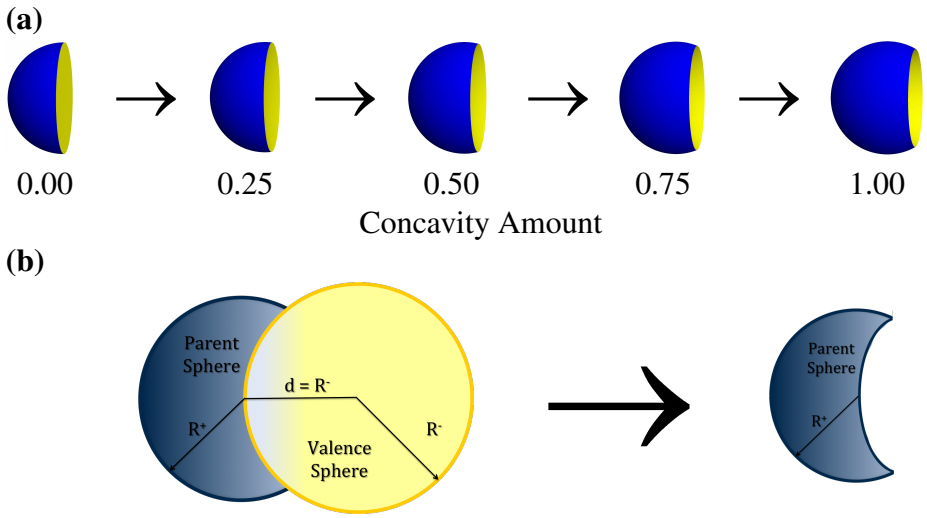

Figure 4.2: (a) Change in shape of a single feature particle from flat facet to concave dimple as concavity amount is increased from 0 to 1. (b) Particles are built as an intersection of the volume of one parent sphere with the volume outside of a second valence sphere.

free volume for depletants analytically and using a Monte Carlo volume integration, we predict the preferred binding for a given concavity amount and depletant radius. We verify these predictions by performing Monte Carlo simulations of the self-assembly of these colloidal particles in the presence of a sea of penetrable hard sphere depletants using methods described in Chapter 2.

4.2 Model and Methods

The particles studied in this chapter, shown schematically in Fig. 4.2 (a), comprise a parent sphere (radius $R^+ = 1$) that is modified by subtracting a single valence sphere of varying radius (radius R^-). The parent sphere radius is fixed to be one, and the valence sphere radius is varied from 20 to 1. We fix the location of the valence sphere such that it is always tangential to the parent sphere diameter, i.e., distance between the centers of parent and valence sphere is equal to the radius of the valence sphere, $d = R^-$, as shown if Fig. 4.2 (b). We use this condition as a first step in understanding the effect of introducing concavity in a particle's shape. We thus define the "concavity amount",

$$\alpha = \frac{R^+}{R^-}$$

as a parameter varying from 0 to 1 as the valence sphere radius, R^- varies from ∞ to R^+. Previous studies of concave bowls and lenses [99–102, 127] were restricted to the condition

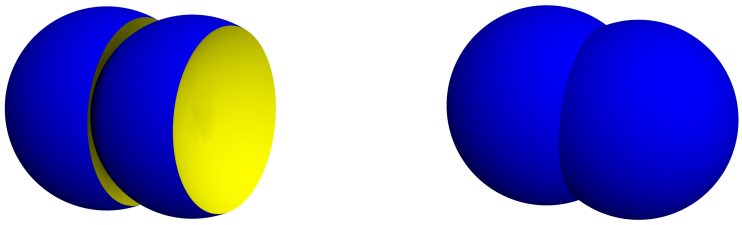

(a) Head to tail binding: chains (b) Head to head binding: dimers

Figure 4.3: Possible binding configurations of particles forming chains (left) and dimers (right). In (a), the particles arrange head to tail forming chains while in (b), the particles arrange head to head forming dimers.

that $R^+ \geq R^-$, due to a limitation in the algorithm used to calculate the overlap of particles. In this work, we determine particle overlaps by implementing a geometric algorithm developed for dimpled particles [7] without this limitation, allowing us to continuously vary the valence sphere radius up to infinity.

We perform standard Monte Carlo volume calculations using penetrable hard sphere depletants of different sizes to calculate the available free volume for depletants in different configurations for a pair of particles. 1000 depletants are thrown into a system of a pair of particles that are fixed in their position and orientation for over five million attempts.

We also use standard Monte Carlo simulation techniques (see, chapter 2 and [57] for details) to obtain assemblies of these particles. We identify crystal structures by replacing each particle by a point at its centroid as in several previous works [8, 22, 63, 64, 136].

4.3 Results

4.3.1 Free Volume

We consider a pair of particles in two possible binding configurations – "head-to-tail" binding and "head-to-head" binding, as shown in Fig. 4.3. In head-to-tail binding, the particles form chains with each other while in head-to-head binding, the particles form dimers. As shown in chapter 3, we understand from equation (3.8) that the potential of mean force and torque between a given pair of particles at fixed configuration in the presence of depletants is dominated by the free volume available to depletants. Hence in order to determine the preferred configuration at different depletant sizes, we consider the free volume available in head-to-tail and head-to-head binding configurations.

Analytical calculations

First we perform analytical calculations of the free volume available to depletants, V_F in each of the configurations. We can write

$$V_F = V - (2 \times V_{excl} - V_{overlap}) \tag{4.1}$$

where V is the total volume, V_{excl} is the excluded volume around a single free colloidal particle that depletants cannot access and $V_{overlap}$ is the overlap in the excluded volume that is gained upon binding of the colloidal particles.

The excluded volume around a single concave colloidal particle is given by the sum of the outer and inner surface area, SA, multiplied with depletant radius thickness r_{depl}.

$$V_{excl} = SA \times r_{depl} \tag{4.2}$$

The overlap in the excluded volume is dependent on both the size of the depletant as well as the binding configuration of the pair of colloidal particles.

In the case of head-to-tail binding, we analytically calculate the point on the valence sphere of the first particle where the radial distance between the valence sphere of the first particle and the central sphere of the second particle (head and tail spheres) equals the depletant diameter. The equations for the valence sphere of the first particle and the central sphere of the second particle are

$$(x - R^-)^2 + y^2 + z^2 = (R^-)^2, \tag{4.3}$$

and

$$(x - R^+)^2 + y^2 + z^2 = (R^+)^2, \tag{4.4}$$

where the spheres are moved by their radius to obtain the head-to-tail configuration for the particles.

We find a point H on the valence sphere such that it is $R^+ + d_{depl}$ away from the central sphere of the second particle, where R^+ is the radius of the central sphere and d_{depl} is the depletant diameter. This point H gives the height of the cap that is inaccessible to depletants. Solving (4.3) and (4.4), we find that H corresponds to a circle with radius r_H, given by the solution to:

$$R^+ d_{depl} = \sqrt{(r_H - R^+)^2 + (R^-)^2 - (r_H - R^-)^2}. \tag{4.5}$$

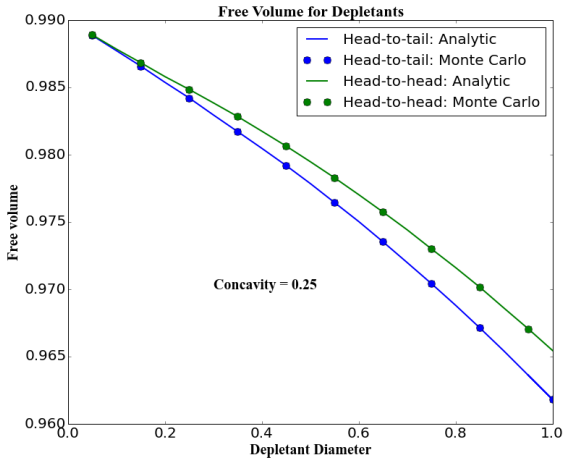

(a)

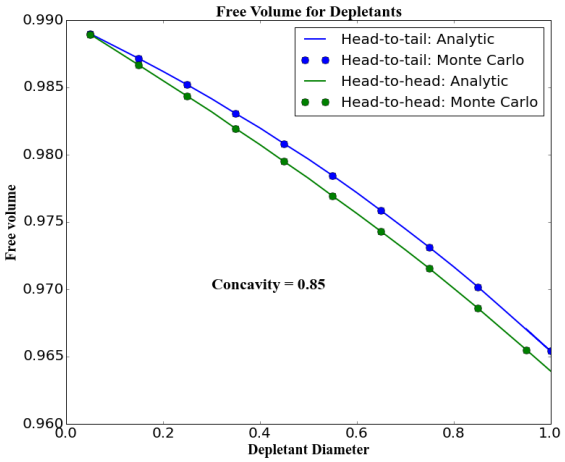

(b)

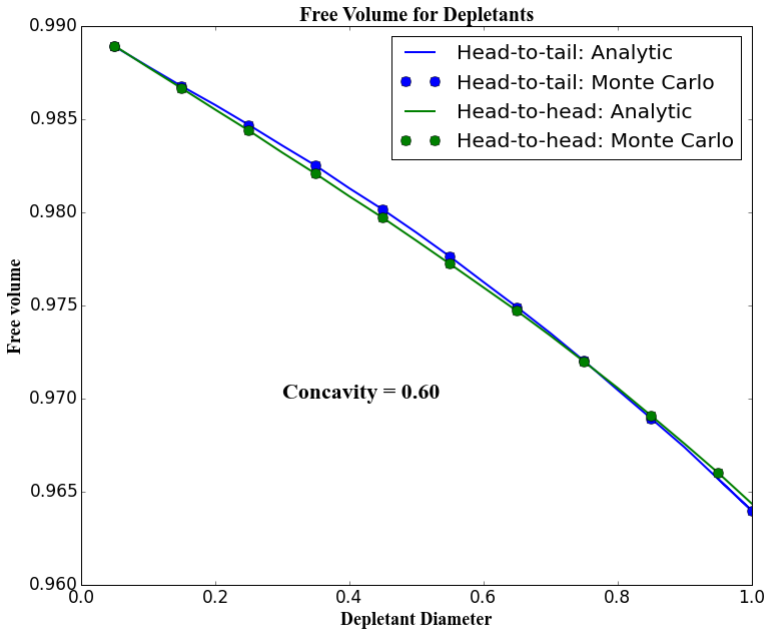

(c)

Figure 4.4: Analytic free volume calculations (lines) and Monte Carlo free volume integration (points) in a system of a pair of single dimple colloidal particles and depletants of varying diameters. The free volume available to depletants as a function of their diameter is shown at concavity amount $\alpha = 0.25$ (a), $\alpha = 0.85$ (b), and $\alpha = 0.6$ (c). We find that the two methods to calculate free volume available to depletants perfectly match. We also observe that at low concavity amounts the free volume is always maximum for head-to-head binding (forming dimers) (a) and at high concavity amounts the free volume is always maximum for head-to-tail binding (forming chains) (b). At intermediate concavity amounts, we see a competition between head-to-head and head-to-tail binding on the order of the depletant volume.

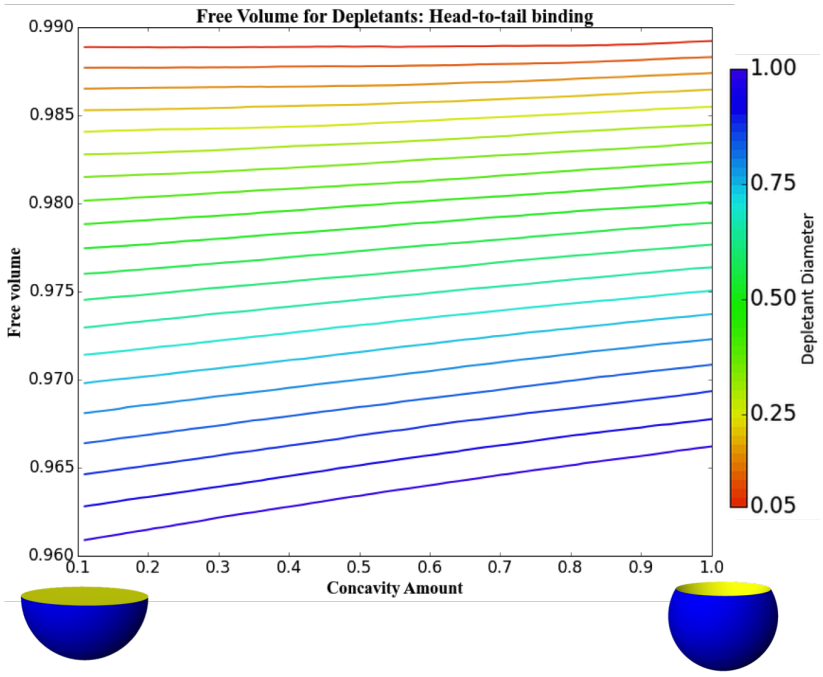

Figure 4.5: Free volume available to depletant particles in the head-to-tail configuration of colloidal particles, at different concavity amount and increasing depletant sizes from red to blue.

Thus we calculate the overlap volume as the sum of the corresponding inner surface area of the valence sphere and the outer surface area of the central sphere of the first and second particles respectively, multiplied by the depletant radius r_{depl}.

Similarly, for the case of head-to-head binding, we analytically calculate the point on the valence sphere of the first particle where the radial distance between the valence sphere of the first particle and the valence sphere of the second particle (face to face spheres) equals the depletant diameter. We perform similar algebra as for the head-to-tail configuration.

We plot the analytical free volume calculations in Fig. 4.4 for different depletant diameters. We see that at small (large) concavity amounts the available free volume is always maximum for head-to-head (head-to-tail) binding. At intermediate concavity amounts, $\alpha \simeq 0.6$, we observe a competition between the head-to-head and head-to-tail binding free volume according to the depletant size. This occurs at these intermediate concavity amounts because the difference in excluded volume for head-to-head and head-to-tail binding is on the order of depletant volume, approximately 0.001. At higher and lower concavity amounts, the difference in excluded volume is roughly ten times larger.

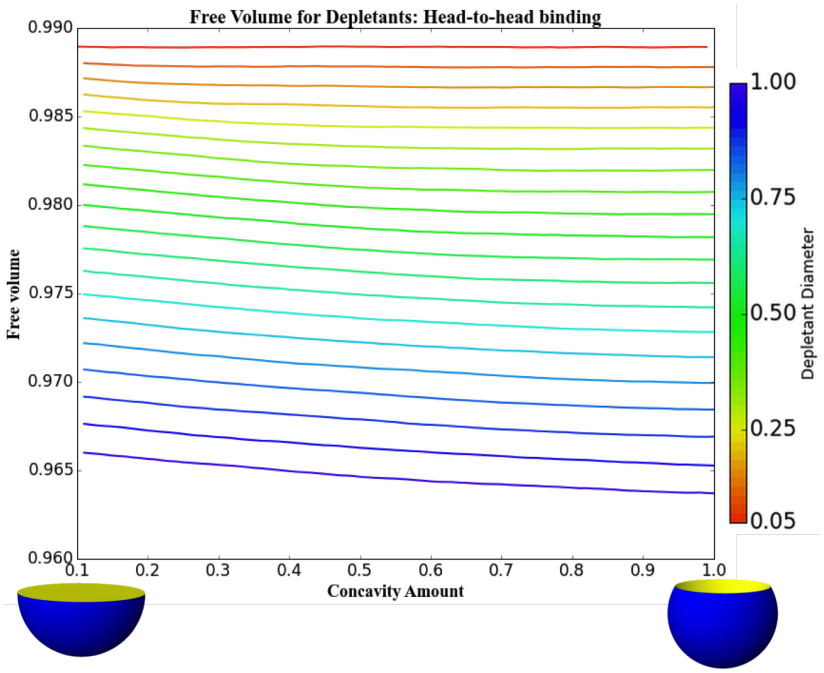

Figure 4.6: Free volume available to depletant particles in the head-to-head configuration of colloidal particles, at different concavity amount and increasing depletant sizes from red to blue.

Monte Carlo integration

Next, we compute by a Monte Carlo volume integration the free volume available to depletants of 20 different radii in $[0.05, 1.00]$ for each configuration at 100 different concavity amounts $\alpha \in [0, 1]$. We present the free volume available to depletants as a fraction of the total volume of the system for head-to-tail and head-to-head binding configurations in Fig. 4.5 and Fig. 4.6.

As shown in Fig. 4.5, in the head-to-tail binding configuration, the fraction of free volume available to depletants increases with increasing concavity for large depletant sizes. This is because at large concavity amounts, the particles align to form a perfect chain, resulting in the smallest excluded volume region for the depletants. As the concavity amount decreases, there is an increasing misfit between neighboring particles, resulting in a smaller excluded volume region for the depletants. This misfit reduces the free volume available to the depletants. At smaller depletant sizes, there is a less significant reduction in the available free volume as the concavity amount decreases between $[1, 0]$.

As shown in Fig. 4.6, in the head-to-head binding configuration, the fraction of free volume available to depletants decreases with increasing concavity for large depletant sizes. This is because at small concavity amounts, the particles align with each other to form a

perfect sphere. As the concavity amount increases, an empty volume is formed between the particles that is inaccessible to large depletant sizes. However, smaller depletants are capable of accessing the volume between the particles, resulting in a less significant reduction in the available free volume as the concavity amount increases between $[0, 1]$.

We also compare our analytic free volume calculations with results from Monte Carlo volume integration, as shown in Fig. 4.4. The difference between these results is on the order of 1E−7, around three orders of magnitude smaller than the difference between head-to-tail and head-to-head binding free volume calculations.

4.3.2 Binding Configurations

From Fig. 4.5 and Fig. 4.6, we understand that the ideal binding configurations of a pair of particles can switch between head-to-tail and head-to-head binding. In order to understand where these transitions could occur, we show in Fig. 4.7 the difference between the free volume for head-to-tail and head-to-head configurations (red curve). In the head-to-tail (head-to-head) binding region shown, the free volume for depletants in head-to-tail (head-to-head) binding configuration is larger than that obtained for head-to-head (head-to-tail) binding.

At small concavity amounts, less than 0.45, head-to-head binding is the preferred alignment for all depletant sizes, (red curve of Fig. 4.7). For larger concavity amounts, we observe head-to-head binding at infinitesimally small depletant sizes that are insensitive to the volume changes between head-to-head and head-to-tail binding configurations. At intermediate depletant sizes, head-to-tail binding configuration is dominant due to the concavity of the shape of the particles. We also observe a reentrant head-to-head binding for large depletant sizes (red curve of Fig. 4.7). This is because at large depletant sizes, the free volume gained by the depletants is insensitive to the smaller volume gain obtained from head-to-tail binding of concave shapes.

Effect of Depletant Concentration

A further note is in order regarding the effect of depletant concentation in the plots shown in Fig. 4.5 – Fig. 4.6. In this work, we calculate the total free volume available to the depletants at a fixed configuration of a pair of particles. This is equivalent to assuming that an infinite pressure of depletants would preserve the configuration being considered. In this sense, the preferred binding configuration for a given concavity amount and depletant size shown in the red curve of Fig. 4.7 is the preferred binding configuration at infinite pressure.

4.4 Self-Assembly of Particles: Engineering Binding Using Depletion Forces

After considering the ideal pairwise configuration of particles in the presence of depletants, we perform bulk self-assembly computational experiments of systems with 100 to 1000 particles at different concavity amounts. Specifically, we target the binding found in Fig. 4.6 – Fig. 4.5 at varying depletant sizes.

In Fig. 4.7, we present the results found. In these simulations, the colloid packing was maintained constant at 0.25. At these low colloid packing fractions, the free energy of the system is dominated by the entropy of the depletant particles and not by the entropy of the colloidal particles. As a result, the free volume available to the depletants plays a significant role in driving the colloid self-assembly at these parameters.

The structure found is determined by the ratio of the peaks in the radial distribution function for the self-assembly of the particles, which is shown in Fig. 4.8 and Fig. 4.9. The depletant packing fraction is varied between 0.20 and 0.50. At higher depletant packing fractions, the dynamics of the system is much slower and thus we do not always achieve equilibrium. At lower depletant packing fractions, we confirm the systems have reached equilibrium by measuring the distribution of cluster sizes and radial distribution function and ascertaining they are constant.

Facetted Sphere Assemblies

For small concavity amounts, we observe facetted binding in the assembly of the particles. This is calculated from the radial distribution function of the bulk self-assembled structures of these particles, as shown in Fig. 4.8 (a). We find that most centers of neighboring particles are less than 1 distance unit apart, which is equal to the radius of the spheres. Additionally, we also observe in Fig. 4.8 (b) that the size of the cluster formed is two particles, as two particles align in a head-to-head binding to form spheres.

From the phase diagram presented in Fig. 4.7, we find that head-to-head binding is reentrant at larger depletant diameters for intermediate concavity amounts, in agreement with our analytic and Monte Carlo volume calculations in the previous section where we showed that the order of the free volume difference between head-to-head and head-to-tail binding is on the order of the depletant volume.

On the timescale of our simulations, the facetted spheres do not hierarchically assemble into an expected double face-centered cubic (fcc) lattice. We believe that this is a limitation of our depletant scheme. With current depletant moves, pairs of spheres do not form a

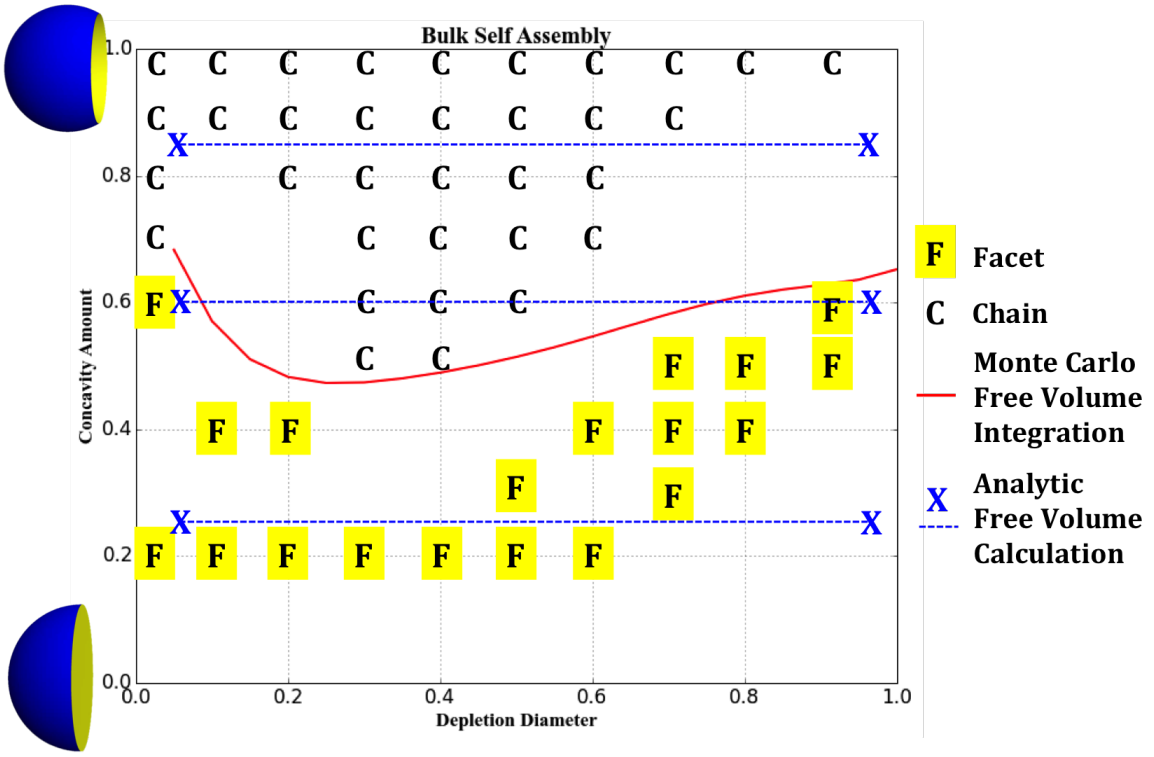

Figure 4.7: Bulk self-assembly phase diagram for particles with varying concavity amounts and depletant sizes. The phase diagram is determined by the ratio of the peaks for head-to-tail and head-to-head configurations from the radial distribution function of the particles. The red curve is the estimated value of zero free volume difference between head-to-tail and head-to-head binding from Fig. 4.5 and Fig. 4.6 by Monte Carlo volume integrations. The red curve denotes the preferred binding configuration of particles according to dimpling amount and depletant size, calculated from available free volume for depletants. In blue dotted lines, we show the points along which analytic calculations were performed in Fig. 4.4 and find a perfect match between the predicted and bulk assembled structures.

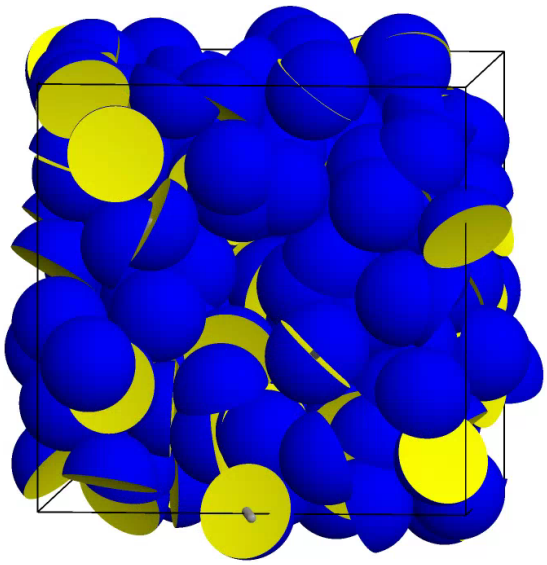

(a)

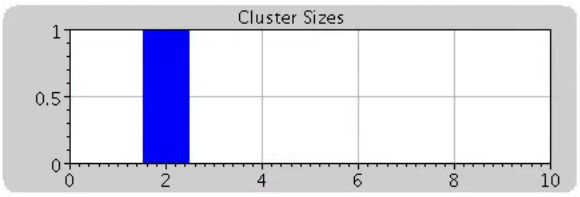

(b)

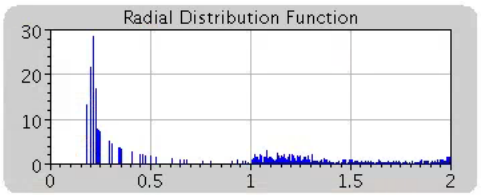

(c)

Figure 4.8: Self-assembly of particles with concavity equal to 0.40, in three-dimensional systems in the presence of depletants with radius equal to 0.8. (a) 3D self-assembly of particles with low concavity into spherical clusters. (b) Cluster size formed is equal to two, as the particles form a sphere. (c) Radial distribution function shows the particles are in facet binding configuration.

double fcc. At the time of publication of this thesis, further work is being carried out on a configurational bias scheme that holds greater promise towards assembly of a double fcc lattice in the presence of depletants.

Chain Assemblies

At higher concavity amounts, we observe the formation of chains as shown in Fig. 4.9. Chains have also been reported in experiments on lock and key particles [99, 100], in the absence of depletants at higher packing fractions. In Fig. 4.9, we show self-assembly of particles with concavity equal to one, $\alpha = 1$, into chains in the presence of depletants. Our results reinforce the idea that depletants are an effective osmotic pressure that promote a higher local density for colloidal particles.

Tetrahedral Particles

Recent studies show that hard truncated tetrahedra form a close-packed diamond structure [63] upon crowding, in the absence of depletants. In our recent work, we showed that cutting a sphere along the planes of a tetrahedron would introduce entropic patches that result in a close-packed diamond structure [8]. Let us consider the extension of these tetrahedrally *facetted* particles into tetrahedrally *dimpled* particles by increasing their concavity amount. We perform these studies in the absence of depletants and propose that depletants can be used to overcome the shortcomings in tetrahedrally dimpled particles.

In Fig. 4.10 (a), we observe that tetrahedrally facetted particles readily self-assemble the diamond crystal at sufficiently high packings, while tetrahedrally dimpled concave spheroidal particles do not. However, a templated assembly process where a diamond unit cell of the particles is fixed at the origin does produce the diamond structure shown in Fig. 4.10 (b).

The reason for the difference in these building blocks lies in the symmetry of these particles. As shown in Fig. 4.10 (c), when two facetted particles come together, they align their faces together (head-to-head binding) to maximize system free volume. In this configuration, these particles have translational freedom to move with their faces aligned. However, in the case of concave particles, the free volume is maximized when two neighboring particles align perfectly inside each other (head-to-tail binding). In this configuration, the particles lose translational freedom to move perpendicular to the lock and key. This results in reduced degrees of freedom for concave particles if they try to assemble into the diamond structure, as shown in Fig. 4.10 (d). As a direct consequence of this, concave spheroidal

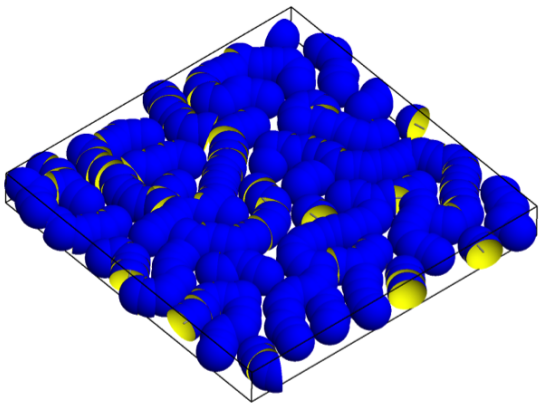

2D Self-assembly of concave particles

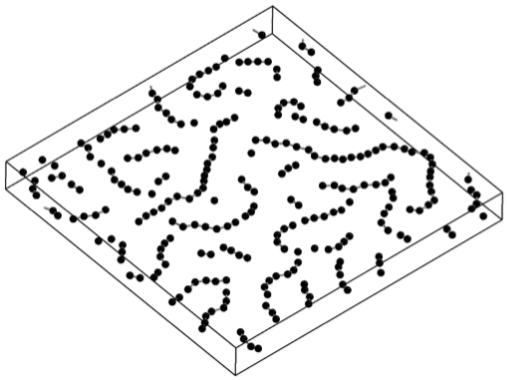

Centers of concave particles forming chains

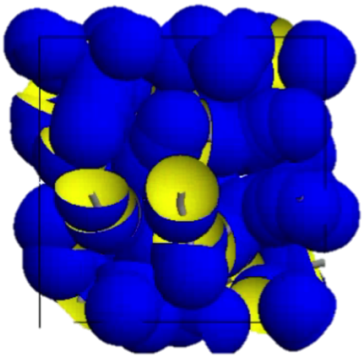

3D Self-assembly of concave particles

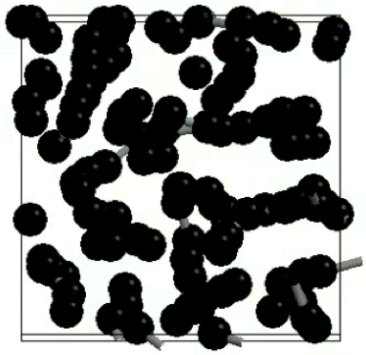

Centers of concave particles forming chains

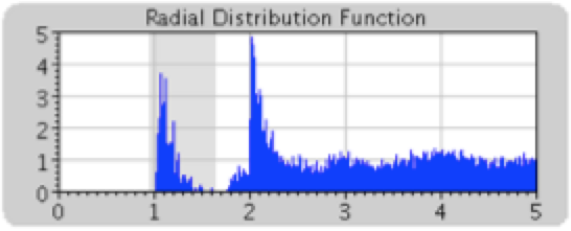

Radial distribution function (RDF) of particles

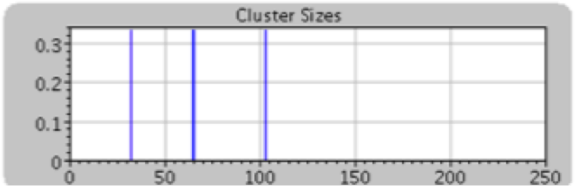

Size and frequency of chains

Figure 4.9: Self-assembly of particles with concavity equal to one, in two-dimensional and three-dimensional systems.

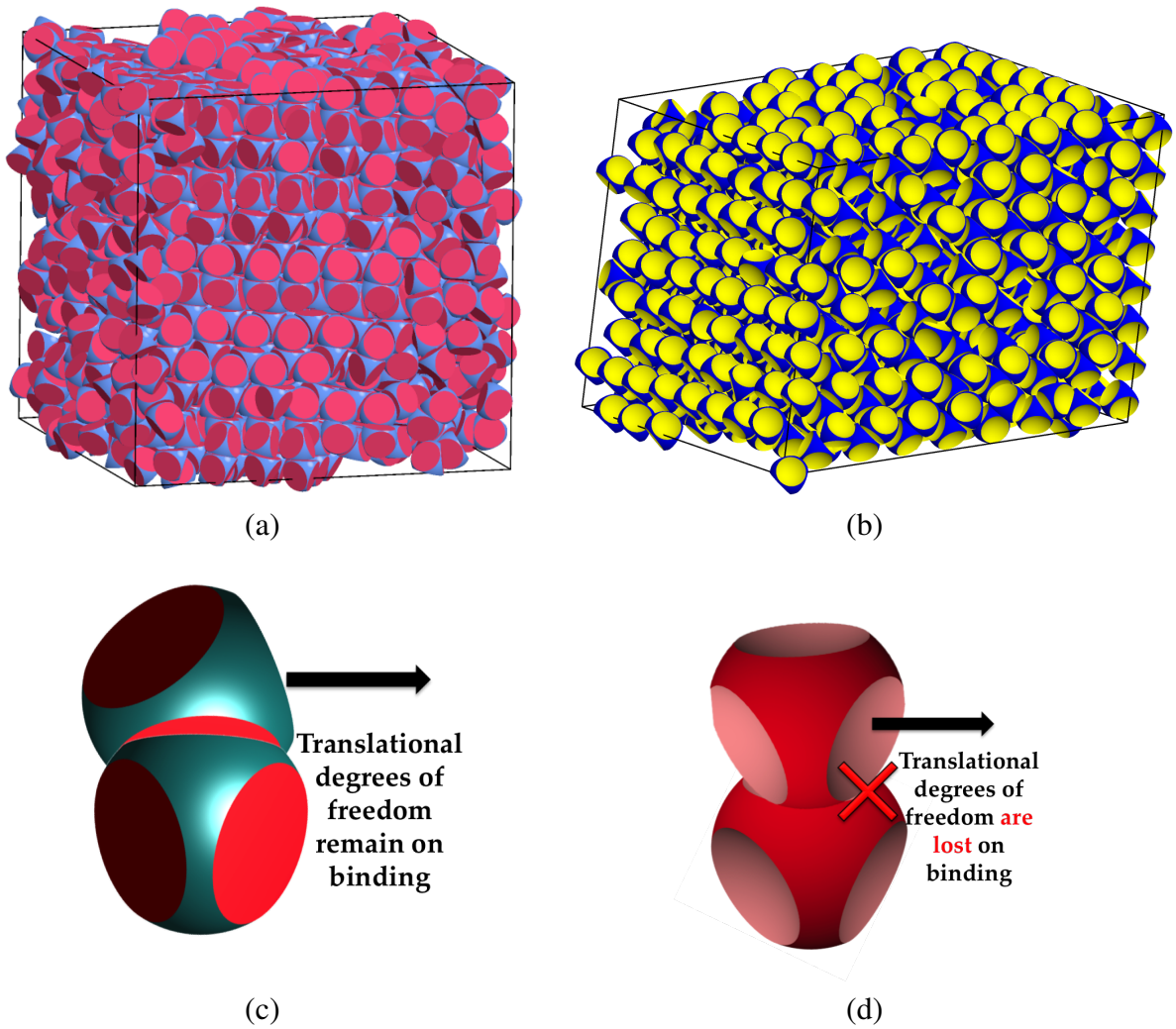

Figure 4.10: Self-assembly of the diamond crystal structure from (a) facetted particles and templated self-assembly of (b) concave particles. There exist extra degrees of freedom in facetted particles (c) in comparison to concave particles (d). The black arrows in (c) and (d) indicate translational degrees of freedom when particles bind that are available to tetrahedrally facetted particles but are unavailable to tetrahedrally dimpled particles.

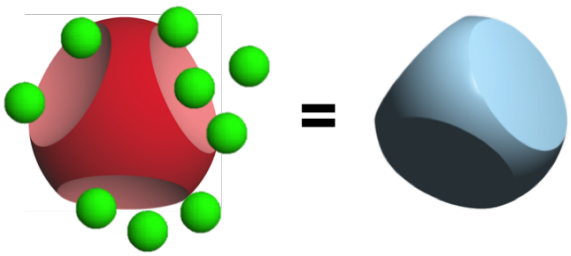

Figure 4.11: Experimentally synthesized tetrahedrally dimpled particles [9] could behave as tetrahedrally facetted particles in the presence of depletants (shown here as green spheres), resulting in the self-assembly of diamond structures [8].

particles have a smaller propensity to form the diamond structure in comparison to their facetted counterparts.

Our study in this chapter lays the foundation for using depletant particles of different sizes to tune concave particles to form the diamond structure. This study is advantageous to help build the diamond crystal using particle shape that can be synthesized in bulk.

4.5 Conclusions

We have considered a continuous change in particle shape from a flat facet to a perfect dimple. This is performed by modeling our particles as a union of two spheres, and continuously varying the ratio of their radii. The preferred binding configuration of these particles is calculated at different depletant sizes and concentrations, and we observe a reentrant facet binding configuration at large depletant sizes. In this manner we evaluate the binding configuration of a pair of particles and predict the bulk self-assembled structure for these particles. We find that particles with large concavity amount form chains as predicted from their preferred binding configuration and particles with smaller concavity have a greater propensity to form a double FCC structure as predicted from their preferred binding configuration.

We have shown the ability of using depletants as a means of controlling the binding between a pair of particles, and thus promote the local dense packing structure in the bulk self-assembly of particles. Particularly, we have shown that by controlling the depletant size, we can control the directionality of entropic forces between particles in their assembly. This finding can help design optimized shapes from different particles that can be synthesized experimentally. Experimentalists have successfully synthesized tetrahedrally dimpled particles [9] that can now be controlled to behave effectively as facetted particles, as shown in Fig. 4.11.

Self-assembly of colloidal particles into such structures with diamond connectivity is a promising avenue for the realisation of photonic crystals operating at infrared wavelengths [137, 138] and the visible spectrum [139]. Photonic crystals are a fascinating concept as they are considered to be "semiconductors for photons" [140]. With periodic structures that have strong optical interference effects, an important goal is to develop optical devices that would serve as diodes, transistors and switches for photons. Such photonic devices would work much faster than their electronic counterparts. Colloidal spheres decorated *in silico* with attractive patches along the corners of a tetrahedron were the first to point the way towards diamond connectivity through self-assembly [22]. Since then, these tetrahedral patchy particles, their phase diagrams and their glass-crystal competition have been studied in depth providing information for their spontaneous assembly into the diamond structure [141–143]. However it is difficult to experimentally introduce such specific enthalpic binding in a colloidal particle [144]. This is where depletants may be a valuable tool.

With an increase in the shape of various building blocks that have been synthesized [145], an interesting step forward is to look for other open crystal structures that can be directly self-assembled by opening up the parameter space by the inclusion of depletant sizes and concentrations [146].

Interplay of Anisotropy Dimensions

Beyond the simple faceting and dimpling of hard spheres, there are many ways of altering particle shape to introduce patches that promote local dense packing. These features act as "entropic patches" that cause preferential alignment.

The various shape operations that may be applied to generate attractive entropic patches may be described in terms of anisotropy dimensions (Fig. 4.12), as was done for enthalpic patches [2]. Eight examples of shape anisotropy dimensions are illustrated in Fig. 4.12, reproduced from [8]. Many of these anisotropy dimensions have already been explored in particles synthesized in the literature. For example, in lock-and-key colloids [21] the anisotropy dimensions of patch size (a), curvature radius (b), and shape composition operation (f) have been synthesized [147]. In roughened colloids the anisotropy dimensions of patch size (a), aspect ratio (c), patch angle (d), number of patches (e) and roughness (h) have been synthesized [84, 106–111]. There are many other examples of work in the literature that can be considered explorations of these anisotropy dimensions [123, 148–177], as we discuss in [8].

From the results in this chapter, we propose that depletants can be used to promote

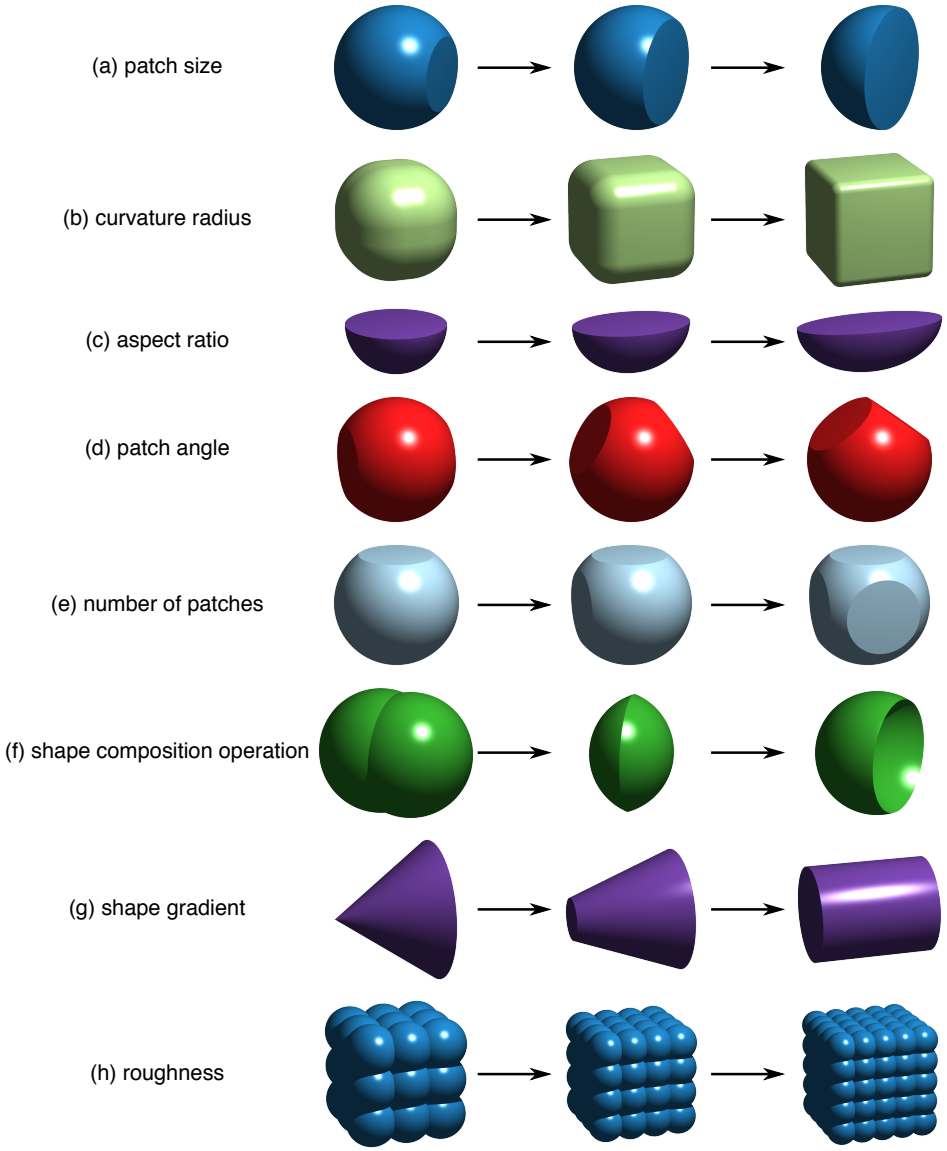

Figure 4.12: Anisotropic dimensions that were proposed in [3] can be tuned and controlled by the presence of depletants, resulting in reconfigurable structures that take advantage of different dimensions at different depletant sizes and concentrations.

reconfigurability between these different anisotropy dimensions. By controlling depletant size and concentration, we can reduce and/or increase the effective entropic force along different dimensions and thus create a large phase space for targeted design of reconfigurable materials.

CHAPTER 5

Crossover Behavior in Hard Concave Spheroidal Particles

5.1 Introduction

Physical systems from flocking animals [19] to heavy fermion materials [178] exhibit emergent macroscopic behaviors that are intrinsically difficult to predict from their microscopic properties [179]. Colloidal systems are fertile ground for investigating emergent behaviors for three reasons: a wide range of colloidal systems manifest emergent behaviors because they have entropy-driven phase behavior [180]; there is a broad range of techniques for manipulating colloids experimentally [36, 145, 181]; and colloidal systems can be investigated with a variety of techniques including *in situ* confocal microscopy [122]. Here, we study the microscopic properties that control the emergent macroscopic behavior of a family of entropically patchy [8] colloidal particles[1].

Entropically patchy particles are anisotropic colloidal particles that, when crowded in a thermal system, exhibit emergent directional entropic forces (DEFs) [8]. DEFs emerge when particles are driven into local dense packing arrangements as the entire system maximizes its shape entropy [8]. By simulating colloids with "entropic patches" – or shape features that promote local packing in certain arrangements – we proposed heuristic rules for controlling macroscopic behavior [3]. In a range of systems we found macroscopic ordering was consistent with entropic patch strengths on the order of a few $k_{\mathrm{B}}T$ [8]. Due to the emergent nature of these forces, however, it is not clear, *a priori*, how directional entropic forces between particles depend quantitatively on particle geometry.

Here we make this connection by studying families of anisotropic lock-and-key colloids [86] with complementary geometric features (see Fig. 5.1) that allow us to quantitatively determine the aspects of particle geometry that control macroscopic ordering. Lock-

[1] This chapter contains work that has been submitted to *Physical Review E*

and-key colloids have been the subject of a number of recent theoretical [87,88,99,100,129] and experimental investigations [9,86,130,147,177,182–185]. We study both packing (infinite pressure) and assembly (finite pressure) behaviors of families of particles that differ by dimple number and symmetry as a function of dimple size. We find that in both cases there are approximate universal parameters of the particle geometry that control macroscopic phase behavior. However, the control parameters are different in the dense packing and assembly limits. In the dense packing limit, a combination of analytic and numerical calculations show that (i) as dimple size increases, there is a crossover from body centered cubic or tetragonal phases to phases that reflect the number of dimples and particle symmetry, and surprisingly (ii) this point of crossover occurs approximately independent of particle symmetry and number of dimples. Similarly, in the assembly limit, we find that as dimple size increases in each family there is (i) a crossover from the FCC structures that are characteristic of hard sphere assembly [186] to BCC structures that are characteristic of soft sphere assembly [187], followed by (ii) a second crossover from BCC to structures that are determined by the particle symmetry and number of dimples. Surprisingly (iii) this second point of crossover also depends on a quantity that is approximately independent of particle symmetry, though it is different from the control parameter in the dense packing limit. We find that in the dense packing limit, the crossover in packing behavior is determined by a quantity that depends simultaneously on the geometry of all of the particle features, whereas in the assembly limit it is determined by the volume of individual dimples. We interpret these results in light of previous work [8] arguing that shape entropy maximization causes entropically driven colloidal systems to optimize local packing. Our results provide detailed quantitative evidence on how shape features control the macroscopic phase behavior of colloidal systems, while providing a concrete example of a set of systems experimentally realizable exhibiting an emergent macroscopic behavior that can be traced to a single universal control parameter.

5.2 Methods

The particles, shown schematically in Fig. 5.1(c) and denoted by Pn_D, comprise a central sphere P that is symmetrically dimpled by subtracting n_D valence spheres, all of the same radius as the central sphere hereafter taken to be one. The valence sphere positions are chosen to be related by discrete symmetries, and are equidistant from the central sphere as shown in Fig. 5.1(b). By using equal radii, there is a clear connection between the dimple volume and free volume gained by the rest of the system when particles bind entropically [3,8] due to shape complementarity. We study bivalent (P2), trivalent (P3), tetra-

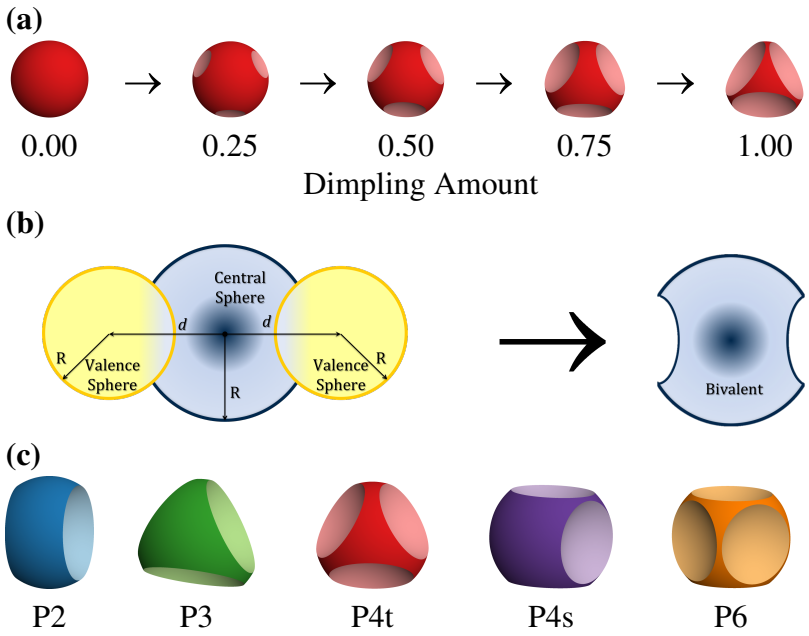

Figure 5.1: (a) Change in shape of a tetrahedral tetravalent particle from convex to concave as dimpling amount is increased from 0 to 1. (b) Parameterization of dimpled concave spheroidal particles. (c) Bivalent, trivalent, tetrahedral tetravalent, square tetravalent and hexavalent model spheroidal particles.

hedrally tetravalent (P4t), square tetravalent (P4s), and hexavalent (P6) dimpled particles. For each of these concave particles, there is a one-parameter family of shapes determined by the distance d between the central and valence spheres which is maximum when the valence spheres are tangent to the central sphere and minimum when the valence spheres are tangent to each other.

Dimples are pairs of spherical caps bounded by the intersection of the central and valence spheres, and have the following volume, surface area, and circumference:

$$v_d = \tfrac{\pi}{12}(d+4)(2-d)^2 \,,$$
$$s_d = \pi(2-d) \,,$$
$$c_d = \pi\sqrt{4-d^2} \,.$$

We parametrize the dimple geometry by linearly mapping d^2 to the "dimpling amount" f, where $f = 0$ ($f = 1$) when d^2 is maximum (minimum).

We use standard Monte Carlo simulation (see, e.g., [57] and Supplemental Materials (SM) for details) to obtain both assemblies and putative densest packings. In both cases, we determine particle overlaps by implementing a geometric algorithm developed for dimpled

particles [7] (see SM for details). To verify the putative densest packings, where practical, we perform analytic calculations to determine the unit cell of the densest packing structure (see SM for details). We identify crystal structures by replacing each particle by a point at its centroid as in several previous works [8, 22, 63, 64, 136].

5.3 Crossover in Densest Packings Structures

Following [188], we study continuous shape deformations. We compute putative densest packings for each family of particles at 100 different dimpling amounts $f \in [0, 1]$; see Fig. 5.2. In all cases, for small $f \approx 0$, particles pack most densely into FCC lattices, like hard spheres [186]. For slightly larger values $f \leq f^*_{DP}$, all particle types pack like soft spheres [64] into a BCT structure. This transition from FCC to BCT packing structures stems from a new contact between particles upon dimpling, sphere-dimple contact, in addition to sphere-sphere contact. The dimple-sphere contact results in a shorter contact distance between neighboring particles. This results in a body-centered tetragonal structure with $\alpha = \beta \neq \gamma$, where α, β, and γ are lattice vectors. The transition from FCC to BCT structures occurs almost instantaneously with dimpling, and is captured in our analytic densest packing calculations. We represent this by means of a single continuous curve in our analytic calculations in Figures B.1 - B.5. However, in numerical putative densest packing calculations, the particles pack in the FCC structure until a large enough dimpling amount due to local frustrations.

Around these values of f, the dimples become increasingly filled by adjacent particles with decreasing system volume, allowing denser packings without the need for global structural rearrangement. In each family, below a critical dimpling amount f^*_{DP} particle dimples make contact with the convex part of adjacent particles, while at f^*_{DP} the concave dimples of one particle *completely* encompass the convex region of a neighboring particle in its tangential direction, meeting the surface of the neighboring concave dimples. In order to help elucidate this observation, we show the configuration of a pair of binary dimpled particles in Fig. 5.3.

At $f \geq f^*_{DP}$, neighboring particles interlock within each other resulting in a crossover to a structure determined by the number and arrangement of dimples on individual particles. We find that just above f^*_{DP}, P2 particles pack into a parquet structure; P3 particles pack into an AB-stacked hexagonal packing (hexagonal close packing–HCP); P4t particles pack into a diamond lattice; P4s particles pack into a tetragonal lattice with rotational parquet symmetry; and P6 particles pack into a simple cubic lattice. A further increase in f beyond f^*_{DP} introduces larger voids between particles and a reduction in packing fraction. As f

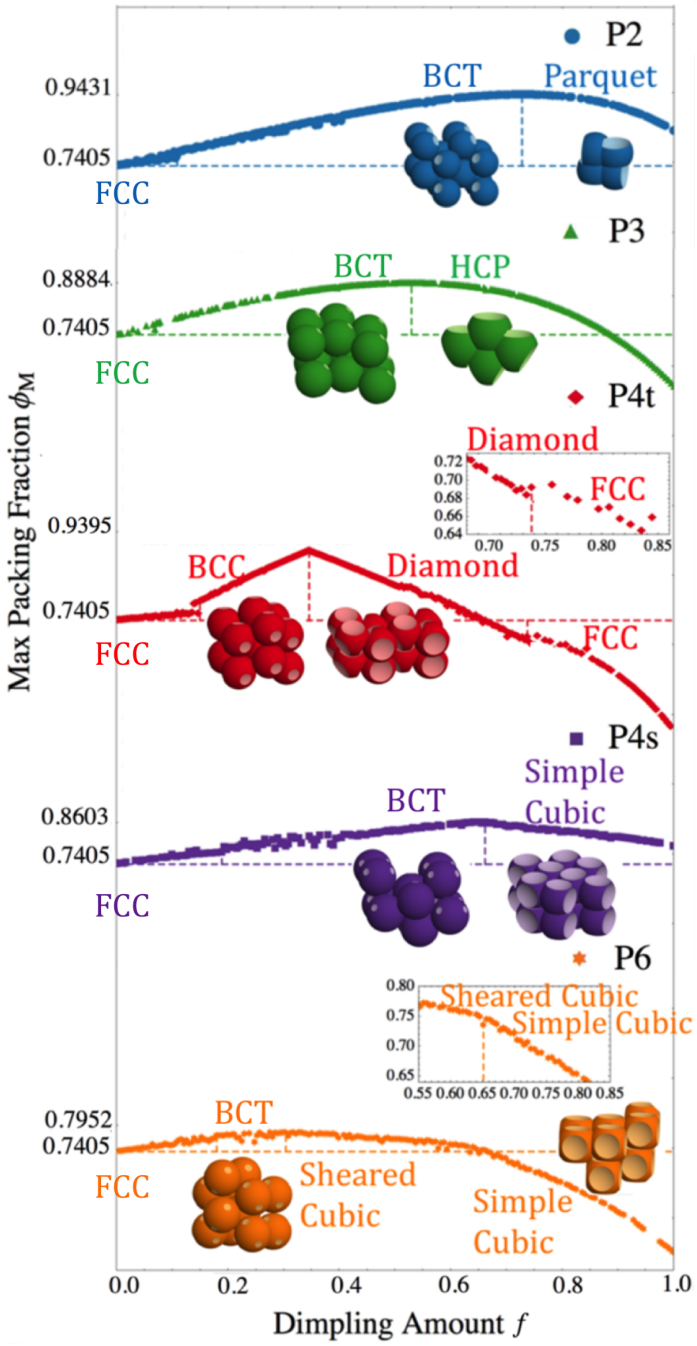

Figure 5.2: Numerical calculations of the density ϕ of the densest obtained packing for dimpled particles as a function of dimpling amount f. The curves for different particles are shifted along the y-axis for clarity. Packing fraction is maximum at a critical dimpling amount $f = f^*_{DP}$ when the dominating features switch from convex to concave regions of the particles. For small f, particles shear from a thermodynamic preference for FCC packing in the hard sphere limit to a BCT packing with the introduction of dimpling. This is not smoothly captured in numerical calculations, but we show that the transition is smooth through analytic packing calculations in the SM. (Right Insets) For P4t and P6 particles, a second transition at larger f is seen from diamond to FCC and sheared cubic to simple cubic respectively.

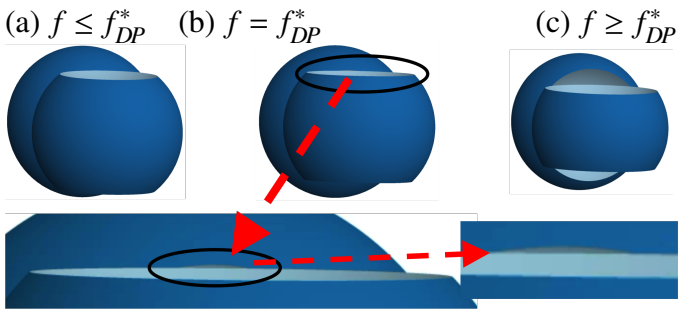

Figure 5.3: Configuration of neighboring particles around the critical dimpling amount for densest packing. In the second row, we show zoomed in images of the particles almost perfectly encompassed in the neighboring dimple at the critical dimpling amount.

increases beyond f^*_{DP}, dimple volume continues to increase, resulting in a smaller volume of the particle in the unit cell structure. This change results in a reduction in the packing density of these structures. At sufficiently large values of f, P3, P4t, and P6 particles pack less densely than spheres.

For P2, P3, and P6 particles the packing fraction changes smoothly as a function of f about its maximum at f^*_{DP}; whereas for P4t and P4s particles there is a cusp. Both types of behavior have been observed previously in dense packings of continuously varying shapes [63, 188, 189]. For P2, P3, and P6 particles, the smooth behavior occurs because structures on either side of f^*_{DP} are related by a continuous shear. For P4t particles the cusp is the result of a crossover from BCC to diamond, and for P4s it is the result of a change from BCC to simple cubic with a rotational parquet symmetry in the simple cubic lattice, which cannot be obtained by a simple shear from the BCC structure.

For P4t particles at high dimpling amounts, $f = 0.7374$, we find another transition from diamond to FCC, shown in the first right inset of Fig. 5.2. At these large dimpling amounts, the densest packing structure arises from a competition between the parallel and anti-parallel alignment of the dimples. With increase in the size of the dimples, neighboring particles find more room to rotate while they are interlocked. This results in a denser packing when the dimples align parallel to each other instead, resulting in a transition from diamond, where dimples exhibit anti-parallel alignment, to the FCC structure.

Similar to P4t particles, we find another transition for P6 particles at $f = 0.6510$, shown in the second right inset of Fig. 5.2. The particles transition from a sheared cubic arrangement to a simple cubic arrangement. This transition is observed in hexavalent particles because of their ability to shear along the 110 lattice vector direction, while neighboring particles remain interlocked in the same configuration.

We seek to quantify our observation that each family exhibits a maximum in packing

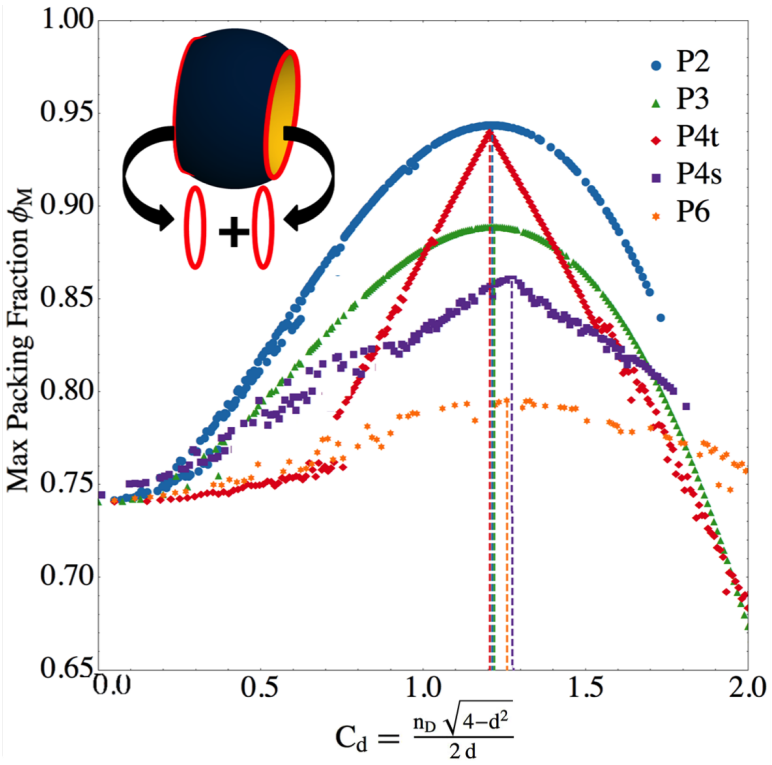

Figure 5.4: Packing fraction ϕ vs the total dimple circumference-depth ratio C_d. The packing fraction reaches a critical maximum at a universal constant $C_d^* = 1.234 \pm 0.060$.

when systems pack into structures in which dimples span convex regions on adjacent particles, through a simple geometric criterion that depends on the number and size of particle dimples. We find that the quantity $C_d \equiv \frac{(n_D c_d)}{(2\pi d)}$, which is the ratio of the total dimple circumference to the dimple depth, evaluated at the value of d corresponding to f^*_{DP} falls in the range 1.23 ± 0.06 across all five particle families; see Fig. 5.4. Further details of these calculations are shown in the following section.

5.4 Geometric Characteristics of Concave Spheres

We calculate geometric characteristics of the particles at various dimpling amounts, as shown in Figure 5.5.

Dimple Volume

The volume of a single dimple, v_d, is calculated as the union of the volume of the two intersecting spherical caps that form the dimple. The volume of spherical cap of radius R and height h is given by

$$V(R,h) = \tfrac{1}{3}\pi h^2(3R-h)\,.$$

For a single dimple formed at the intersection of central and valence spheres of radii R_+, R_-, its volume is given by

$$v_d = \tfrac{\pi}{12d}(R_+ + R_- - d)^2 \times (d^2 + 2dR_+ + 2dR_- + 6R_+R_- - 3R_+^2 - 3R_-^2) \tag{5.1}$$

. For $R_+ = R_- = 1$,

$$v_d = \tfrac{\pi}{12}(d+4)(2-d)^2\,. \tag{5.2}$$

where d is the distance between the centers of the central sphere and the valence sphere. The volume of the remaining particle v_{sp} is given by

$$v_{sp} = v_{PS} - (n_D \times v_d)\,. \tag{5.3}$$

where v_{PS} is the volume of the original central sphere, v_d is the volume of a single dimple and n_D is the number of dimples in the particle. This gives

$$v_{sp} = \tfrac{4}{3}\pi R_+^3 - n_D \times \tfrac{\pi}{12}(d+4)(2-d)^2\,. \tag{5.4}$$

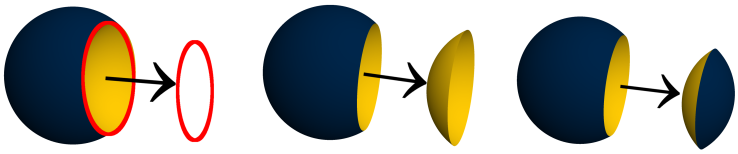

(a) Circumference (b) Surface Area (c) Volume

Figure 5.5: The different shape features of multi-dimpled spheres considered in this study.

We normalize the total dimple volume for a particle by

$$V_d = \frac{n_D \times v_d}{v_{sp}}. \tag{5.5}$$

Dimple Surface Area

Similar to the volume of the dimples, we calculate the surface area of a single dimple and normalize the total surface area of the dimples by the surface area of the particle. The surface area of a single dimple s_d is calculated as the surface area of a spherical cap formed between the central and valence spheres. For spheres of radii R_+, R_-, the surface area is given by

$$s_d = \frac{\pi R_-}{d}(R_+ - R_- + d)(R_+ + R_- - d). \tag{5.6}$$

For $R_+ = R_- = 1$,

$$s_d = \pi(2 - d). \tag{5.7}$$

The surface area of the particle, s_{sp}, is given by

$$s_{sp} = s_{PS} - (n_D \times s_d). \tag{5.8}$$

where s_{PS} is the surface area of the original central sphere. This gives

$$s_{sp} = 4\pi R_+^2 - n_D \times \pi(2 - d). \tag{5.9}$$

The self-assembled non-spherical crystal structure is rather dependent on the number and arrangement of dimples in the particle. We normalize the total dimple surface area S_d for a particle as

$$S_d = \frac{n_D \times s_d}{s_{sp}}. \tag{5.10}$$

Dimple Circumference

Similarly, the circumference of the dimples c_d is calculated from the radius of the circle of intersection between the central and valence spheres. For spheres of radii R_+, R_-, the circumference is given by

$$c_d = \frac{\pi}{d}\sqrt{(-R_+ + R_- + d)(R_+ - R_- + d)} \times \sqrt{(R_+ + R_+ - d)(R_+ + R_- + d)} \tag{5.11}$$

. For $R_+ = R_- = 1$,

$$c_d = \pi\sqrt{4 - d^2}\,. \tag{5.12}$$

This circumference is normalized by the distance between the central and valence spheres. To reduce the numerical ratio, we use a weight 2π and call this normalization factor c_{sp}. This factor is given by

$$c_{sp} = 2\pi d\,. \tag{5.13}$$

The total circumference of the dimples C_d is thus normalized by the circumference of a circle describing the distance between the parent and valence sphere in the particle.

$$C_d = \frac{n_D \times c_d}{c_{sp}}\,. \tag{5.14}$$

5.5 Crossover in Self-Assembled Structures

We also performed MC simulations at finite pressures to study assembly behavior away from the dense packing limit.

Near $f = 0$ we observe the assembly of FCC lattices as we would expect for hard spheres, while at small dimpling amounts, in all cases we observe a crossover from FCC to BCC. This transition suggests that particles with small dimples ($f \leq f^*_{SA}$), irrespective of their symmetry, behave effectively as soft spheres (see SM for further discussion) which are known to assemble BCC and other non-close packed lattices [187, 190]; this crossover has also been observed in DNA-mediated assembly [191, 192]. This effective softness may also underlie the existence of BCC rotator phases for several symmetric convex polyhedra [64].

Above a critical value $f \geq f^*_{SA}$ for each family, the phase behavior is dependent on the arrangement of dimples, as shown in Fig. 5.6. P2 particles self-assemble a parquet lattice. For P3 and P4t we do not observe assembly of an ordered structure from a homogeneous fluid at any density on the time scale of our simulations. For P3, we find the expected triangular lattice is stable against melting to a packing fraction of 0.35. For P4t, if seeded, particles assemble a diamond lattice as found previously for tetrahedrally

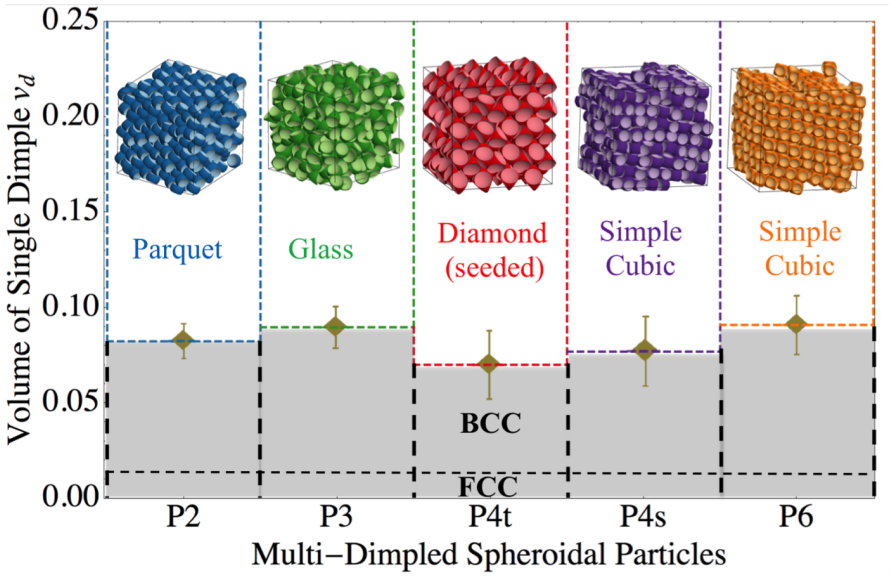

Figure 5.6: Self-assembled crystals for different multi-dimpled spheroidal particles vs volume of individual dimples in particles. We find that critical volume of an individual dimple determines the spherical or non-spherical self-assembly of these particles.

patterned enthalpically patchy particles [22], but unlike truncated tetrahedra [63] or tetrahedrally facetted spheres [8]. P4s particles self-assemble a cubic lattice with rotational parquet symmetry. P6 particles self-assemble a simple cubic lattice. In all cases we observe that the ordered phase coincides with an emergent valence, or angular specificity in the effective interactions between neighboring particles, on the order of a few $k_B T$ (see SM), as has been observed for convex particles [8].

As in their packings, in each family we observe a crossover from a BCC phase to a phase dependent on particle symmetry at f^*_{SA}, and we seek to determine if this crossover can be characterized by a quantity that is independent of particle symmetry. We find that the volume of individual dimples on a particle shows little variation at f^*_{SA} suggesting that individual dimple volume is the key microscopic parameter that controls the emergent phase behavior in these systems, irrespective of particle symmetry.

5.5.1 Potential of Mean Force and Torque

The potential of mean force and torque (PMFT) is a measure of the effective entropic attraction between a pair of particles due to the surrounding particles [8]. We calculate PMFT to show the difference between self-assembled structures by multi-dimpled concave spheroidal particles at different dimpling amounts. These calculations are evaluated at the lowest density where the crystal structure is formed, around a constant volume with a single

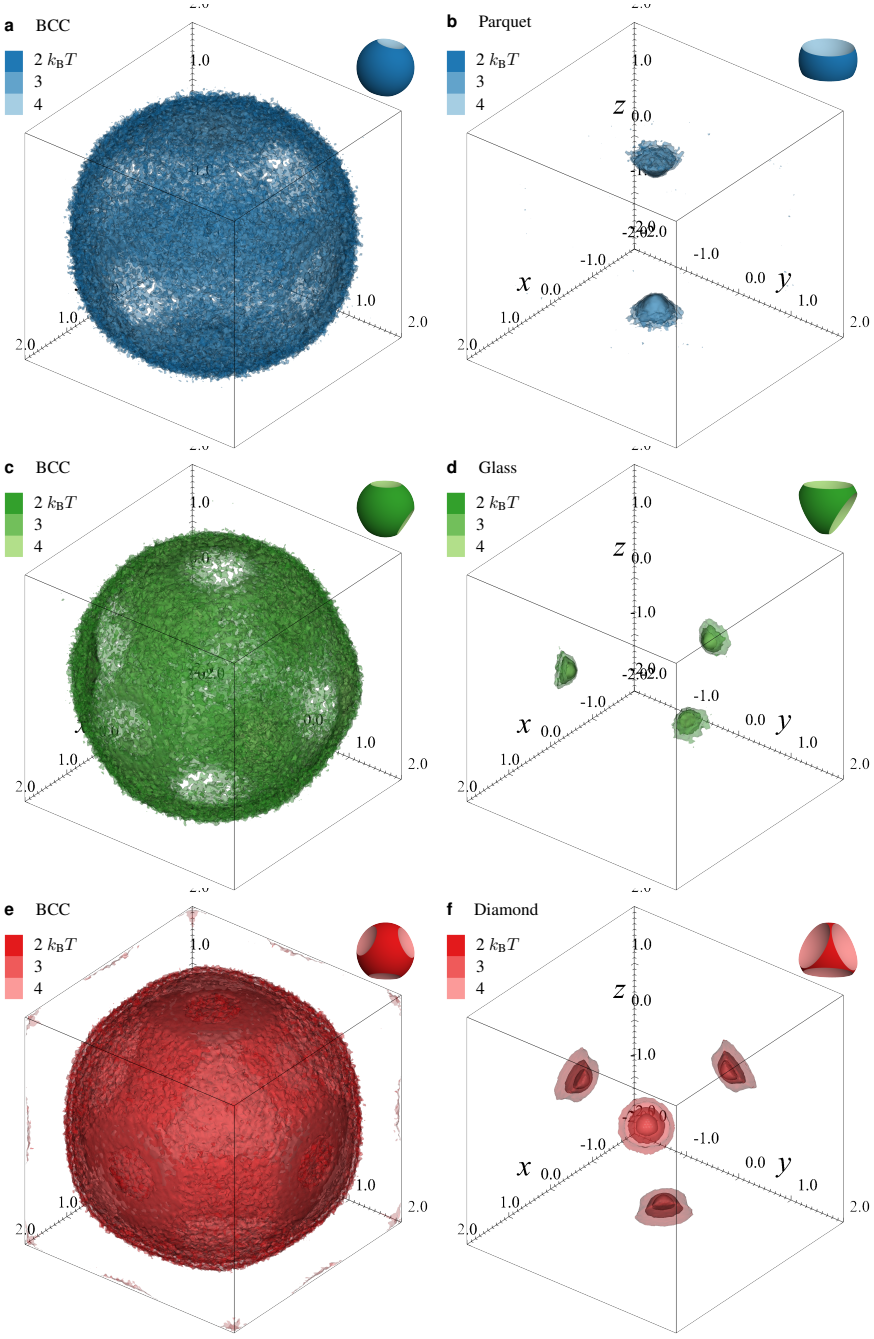

Figure 5.7: Potential of mean force and torque (PMFT) calculations [8] show that below the critical dimpling amount f_{SA}^{*} (left) an isotropic potential exists. At higher dimpling amount (right), an attractive free energy well is presented in the volume of the dimple, giving rise to different crystal structures. (a, b) Bivalent particle showing (a) BCC and (b) parquet potentials. (c, d) Trivalent particle showing (c) BCC and (d) triangular sheet potentials. (e, f) Tetrahedrally tetravalent particle showing (e) BCC and (f) tetragonal diamond potentials.

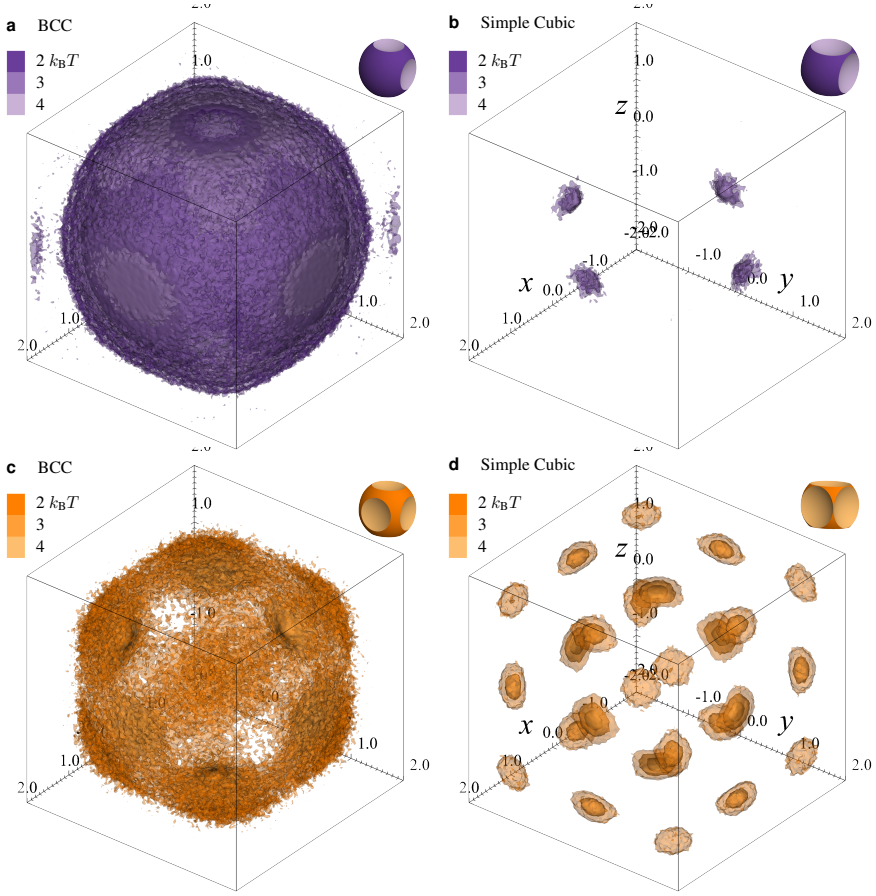

Figure 5.8: Potential of mean force and torque (PMFT) calculations [8] show that below the critical dimpling amount f_{SA}^{*} (left) an isotropic potential exists. (a, b) Square tetravalent particle showing (a) BCC and (b) simple cubic potentials. (c, d) Hexavalent particle showing (c) BCC and (d) simple cubic potentials. Because the lattice vector of the cubic lattice formed is small in this case, we see second and third neighbor peaks in the cubic potential.

particle placed at the center using methods introduced in our previous works. In Figures 5.7 - 5.8, we visualize this PMFT as a heat map in three dimensions using VisIT [193]. Below the critical dimpling amount f^*_{SA}, we see an isotropic potential around the particle. At higher dimpling amounts, the dimples behave as an entropic patch resulting in an attraction between patches.

5.6 Discussion

We found a universal structural crossover in packing that corresponds to a quantity that depends on all features of a particle shape, and one for assembly that depends on individual particle features. These findings accord well with recent work [8] arguing that assembly is driven by local packing whereas packing is a global phenomenon.

5.6.1 Emergent Behavior

Ref. [8] argued that the phase behavior of several systems of convex particles was driven by pairwise packing considerations – our finding that individual dimple geometry controls assembly extends this hypothesis to concave spheres. Additionally, in this system, when a particle binds entropically at a dimple, it loses rotational entropy given by $k_\mathrm{B} \ln \Omega$ (where Ω is the number of distinct particle orientations[2]). This entropy loss is compensated by a gain in entropy for the rest of the system. It was argued in [8] that this should be determined by the stress tensor, which for assembly is typically on the order of $k_\mathrm{B}T/v_p$ where v_p is the particle volume. This suggests that the additional entropy gained by the system is on the order of $k_\mathrm{B}v_d/v_p$, where as particle pairs bind, the rest of the system gains v_d extra free volume. Thus our finding that individual dimple volume is the parameter that controls assembly is reasonable and well grounded. The systems we studied are ideal for identifying this relationship because the free volume gained when particle pairs bind entropically is well-defined due to shape complementarity. However, we propose that the intuition we develop here might be useful for other systems of entropically patchy particles in which the additional volume gained by the system upon binding is less well-defined. Similarly, we found a specific geometric criterion that corresponds to the crossover in dense packing behavior; though we do not expect this specific criterion to persist in other systems, we expect the contrast that packing behavior is controlled by quantities that depend on the totality of particle shape, whereas assembly can be ascribed to individual features of particle shape, to persist in other systems.

[2] In technical terms, Ω is given by the volume of the relevant rotation group.

5.6.2 Reconfigurable Crystal Structures

To develop reconfigurable materials by changing colloid shape, we need a better understanding of how changing colloid shape features affects bulk packing at infinite pressure and thermodynamic self-assembly behavior away from infinite pressure. A number of studies involving shape transformation of convex building blocks have studied reconfigurable self-assembly [188, 194–197].

The existence of an universal criticality in packing and assembly behavior of dimpled particles indicates that these families can be categorized into "effectively" spherical or aspherical building blocks. Dimpled spheroidal particles of any valence can be developed as functional analogs to chemical molecules that exhibit lock-and-key binding [9]. This functionality conceivably can then be toggled on and off by swelling and shrinking them, resulting in interesting "dual" behavior of these building blocks. Fine control of the shape of such convex-concave building blocks can be experimentally realized by the absorption and desorption of solvent molecules by the building blocks. This mechanism has been recently used to tune convex building blocks between spheres and convex lenses [198, 199]. This reconfigurability inherent in building block shape can potentially deliver reconfigurability in the bulk crystal structure, resulting in switchable material properties.

5.6.3 Open Crystal Structures

We also note that crystal structures formed by multi-dimpled particles self-assemble at packing fractions of $40-50\%$, much lower than that observed in convex systems, which are typically $\geq 50\%$ (e.g. [8, 59, 63, 64, 200]). It has been proposed recently that entropy can stabilize open lattices in systems with both enthalpic and entropic contributions to the free energy [201]. Here, we found that entropy alone can stabilize open structures. The absence of strong enthalpic interactions in the present system may also result in fewer kinetic traps. Open structures are important not only for photonics, but also in applications such as advanced catalysis and medical diagnosis [202].

Finally, we have described a system that exhibits complex emergent entropy-driven phase behavior that can be ascribed to a universal underlying microscopic control parameter. Because emergent behaviors are inherently difficult to ascribe to microscopic system details, we believe this example in systems of colloids that can be conveniently synthesized [9, 177] is particularly useful because of possible experimental manipulation of emergent behavior.

CHAPTER 6

Packing and Assembly of Symmetric Sphere Union Particles

6.1 Introduction

Entropy has been used to design close packed structures [63, 64] through local dense packing motifs that repeat throughout the system [8]. In previous chapters, we designed directional entropic forces through different shape modifications [3]. The various shape modifications that have been proposed in [3] are primarily used to build entropically attractive patches on building blocks. Here, we consider the possibility of building entropically *repulsive* patches on building blocks in order to build open crystal structures. Open crystals have a large number of applications including heterogeneous catalysis where they could be used as zeolites. Building such open crystals purely out of entropy is interesting as entropic particles are less prone to kinetic arrest during assembly. Additionally, with the introduction of entropically repulsive patches in particles, we observe a competition between attractive and repulsive emergent forces upon crowding of the particles. This results in a larger number of densest packing structures obtained through finely tuning the various geometric aspects of entropic particles.

In this work, we consider sphere union particles with two, three, four (tetrahedral and square planar arrangement) and six symmetric spheres fused with one central sphere, as shown in Fig. 6.1. These building blocks are a natural extension of hard snowman [203] and dumbbell [204] shaped particles that have been extensively studied in the literature. The sphere union particles studied in this chapter have been readily synthesized using polymerization techniques [205, 206] and ultrasonic-induced emulsification [207] among other methods [208]. These particles hold the promise of a number of applications, similar to colloidal dimers that have been used to create patterns resulting in antireflecting surfaces [209].

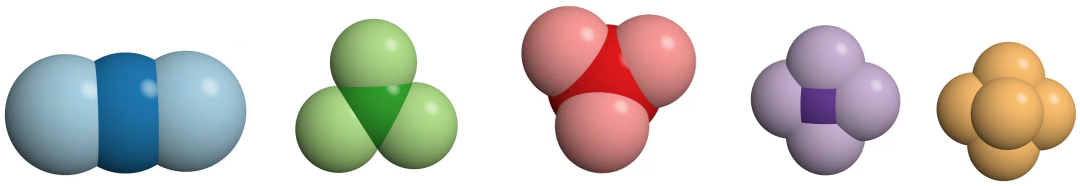

Figure 6.1: Sphere union particles with two, three, four (tetrahedral and square planar arrangement) and six symmetric spheres fused with one central sphere.

Sphere union particles are also a direct structural analogue to common chemical molecules and have thus been called colloidal molecules [210]. A range of the molecular analogues were first synthesized by Manoharan et al. [211]. Since then, fine control of bond-angle in these molecules has been achieved in a reproducible and controllable fashion [212] using self-assembly techniques [213] as well as in large quantities [214]. More recently, sphere union particles with chemically distinct surface patches that are functionalized using single stranded DNA's sticky ends have been synthesized [35]. These hold a greater promise in both enthalpic and entropic mimicry of atomic molecules, developing colloids with valence, which possess reversible, specific, and directional interactions with well-defined symmetries.

Understanding the densest packing and self-assembly of particles are key to understanding how they organize into ordered structures. These structures are governed by various shape characteristics of the particles. The densest packing is the structure formed by particles at infinite pressure. The self-assembled structure is the lowest free-energy arrangement of particles that can be kinetically achieved, in a given thermodynamic ensemble.

Here, we demonstrate the packing and assembly behaviors of sphere union particles shown in Fig. 6.1. We determine that there exist a number of densest packing structures for a small range of particle shape parameters. We find that when the particle shape is primarily spherical, the particles assemble into a rotator face-centered-cubic crystal structure. However, when the particle shape is dominated by their spherical protuberances, the large number of competing densest packing structures result in no long range crystal order at intermediate packing fractions. Particles that have a few competing densest packing structures easily self-assemble into crystal structures while others are unable to assemble due to kinetic arrests on the time scale of our simulations. We propose that this is an important criterion to determine if a structure can be assembled by purely entropic means. In the case of kinetically arrested pathways, we propose that the addition of enthalpic interactions to stabilize densest packing structures can be used for their successful assembly. We discuss this understanding in the context of modeling proteins using soft-matter techniques to

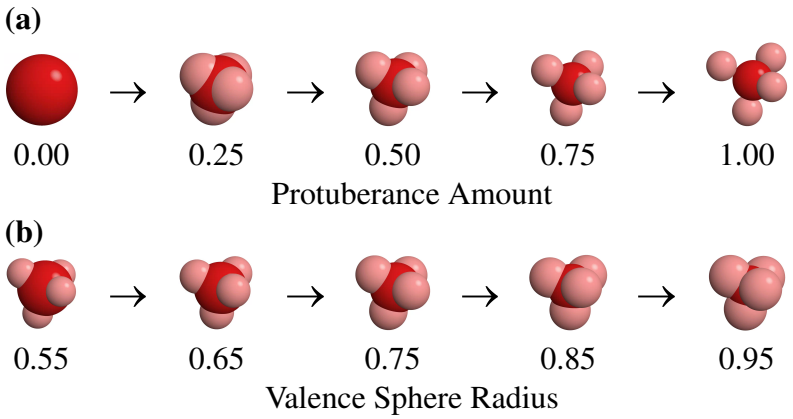

Figure 6.2: (a) Change in protuberance amount, i.e. distance between parent and valence spheres, of a tetrahedral tetravalent particle from 0 to 1. (b) Change in valence sphere radius to parent sphere radius from 0.55 to 0.95, where parent sphere radius is kept constant at 1.

determine the driving factors in protein crystallization.

6.2 Model and Methods

We study families of hard sphere union particles, as shown in Fig. 6.1, which belong to a family of colloidal molecules. The particles, denoted by PxP, are composed of a parent sphere P that is symmetrically adsorbed with x valence spheres P. We study bivalent (P2P), trivalent (P3P), tetrahedrally tetravalent (P4Pt), square tetravalent (P4Ps), and hexavalent (P6P) particles. We fix the radius of the parent sphere to 1 length unit and study varying radii of the valence sphere, $r \in [0.5, 1.0]$ at different protuberance amounts, as shown in Fig. 6.2. We define protuberance amount, α, as the distance between the centers of the parent and valence spheres. Protuberance amount α is varied between $[0, 1]$ such that the particle is made of a sphere at $\alpha = 0$ (distance between central and valence sphere is minimum) and the parent and valence spheres are tangent at $\alpha = 1$ (distance between central and valence sphere is maximum). The valence sphere positions are chosen so that their positions are related by discrete symmetries, and are equidistant from the central sphere as shown in Fig. 6.1. We determine common features between these particles that control the various crystal structures that can be formed.

Monte Carlo simulations are performed using a Hard Particle Monte Carlo plugin developed for HOOMD-Blue [1] [6]. We determine particle overlaps by implementing a recursive algorithm developed for particles that can be defined as unions of different shapes – in this

[1] http://codeblue.umich.edu/hoomd-blue/

case, a union of spheres. The densest packing structure is found by compressing systems with 1, 2, 3, 4 and 8 particles placed in a box with periodic boundary conditions [188]. Isobaric (NPT) simulations are then run with a slowly increasing pressure. The box is allowed to shear and change shape until the smallest box is found. We find this typically takes the order of $10E5$ iterations. To identify the crystal structure formed by these particles, each particle is replaced by a spherical "atom" positioned at its centroid resulting in an isostructural arrangement to an atomic crystal, an approach used in several previous works [8, 21, 63, 64, 136].

In order to determine the self-assembled structure of these particles, we begin with a random configuration of 512 particles. This system is initially equilibrated at a small packing fraction (~ 0.1) for 10^5 MC steps. Isochoric (NVT) simulations are then performed where the packing fraction is slowly increased until it reaches a target value. The system is then allowed to equilibrate at this state point for $\sim 5 \times 10^8$ MC steps . Packing densities are varied between $0.35 \leq \phi \leq \phi^*$, where ϕ^* is the densest packing for that particle.

6.3 Results

6.3.1 Densest Packings of Sphere Unions

We compute densest packings for each family of particles – $P2P$, $P3P$, $P4Pt$, $P4Ps$ and $P6P$ – at 100 different protuberance amounts $\alpha \in [0, 1]$ and 11 different valence radii $r \in [0.5, 1.0]$; see Fig. 6.3 - Fig. 6.7.

At $\alpha = 0$, all particles are spheres that pack into the FCC lattice. At $\alpha = 1$, the particles consists of spheres that are glued together along a specific symmetry. Here the particles pack the poorest if the spheres are of mismatching radii with $\phi_{max} \in (0.4, 0.5)$.

For values of α between 0 and 1, the same set of packing structures are found for a single particle shape at all values of r. However, the packing curves change from one structure to another within this same set according to the amount of empty volume available in the box. Thus this occurs at different values of α for different values of r.

Consider the case of P2P particles. For a given radius r, the particles switch from face-centered cubic (FCC) to body-centered tetragonal (BCT) initially through a smooth transition, typically at lower values of α. As α increases, there is a sharp continuous transition from BCT to two-dimensional tetragonal sheets with AB stacking. At greater values of α, there is another sharp transition into the BCT structure. As radius r varies from 0.5 to 1.0, initially there is a decrease in α required for transition. At higher r, the trend is reversed with an increase in α required for transition.

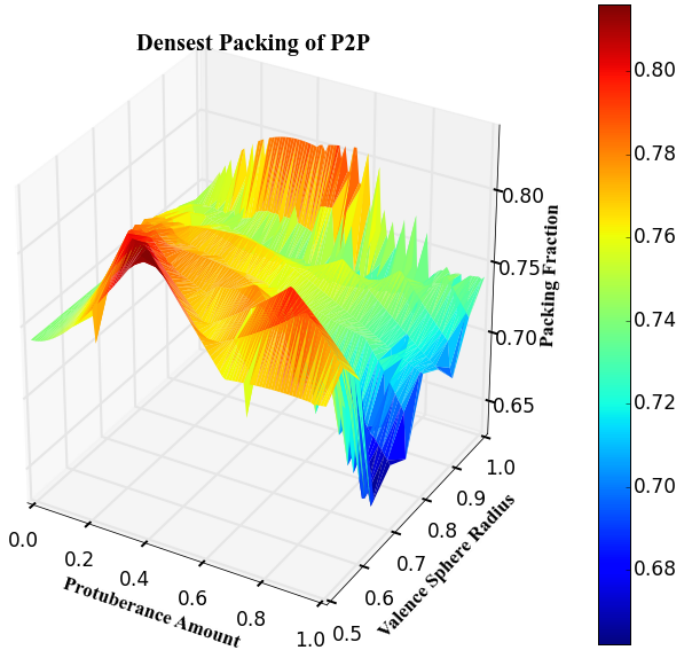

Figure 6.3: Densest packing surface of bivalent (P2P) particles, at different radii of valence sphere, with increasing protuberance amount. The rich variety of structures holds the promise of using the same building blocks to stabilize different structures.

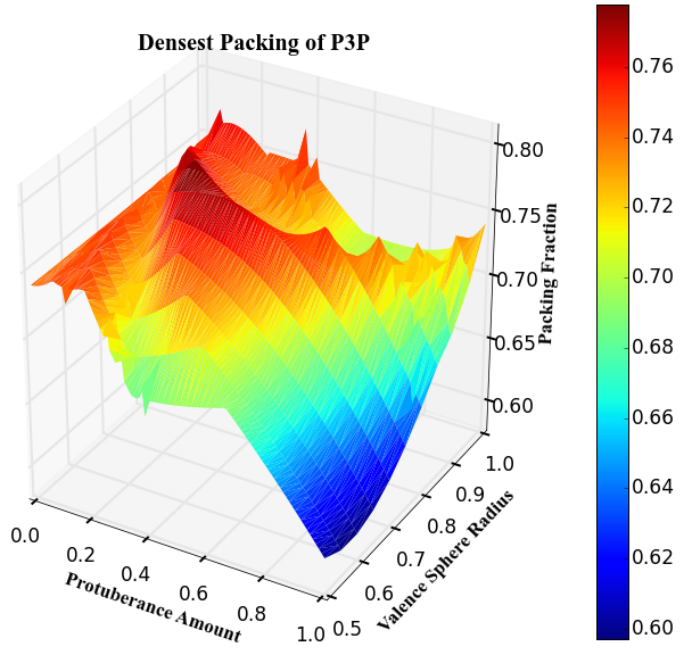

Figure 6.4: Densest packing surface of trivalent (P3P) particles, at different radii of valence sphere, with increasing protuberance amount. Different structures are found at different radius values.

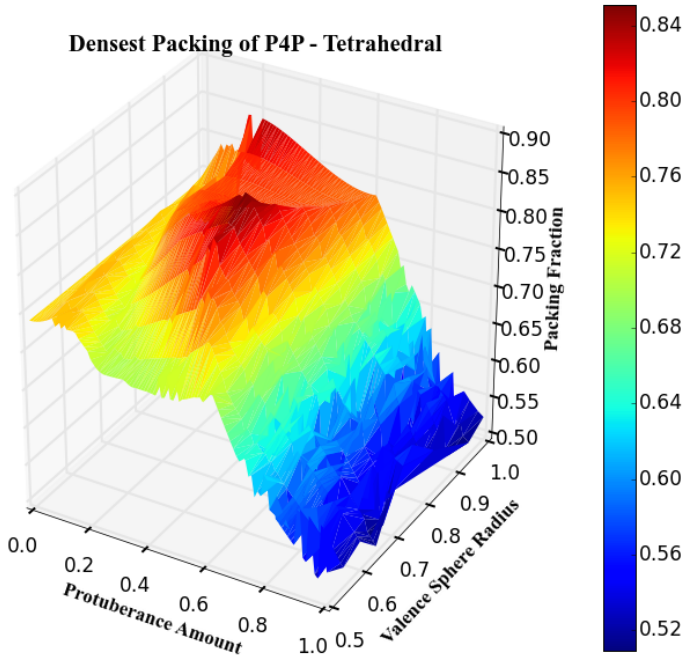

Figure 6.5: Densest packing surface of tetrahedral tetravalent (P4Pth) particles, at different radii of valence sphere, with increasing protuberance amount. Different structures are found at different radius values.

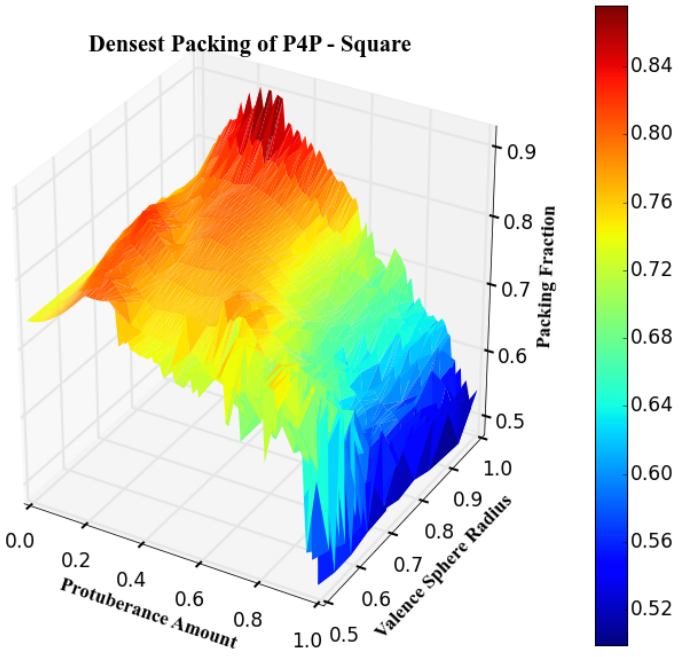

Figure 6.6: Densest packing surface of square tetravalent (P4Ps) particles, at different radii of valence sphere, with increasing protuberance amount. Different structures are found at different radius values.

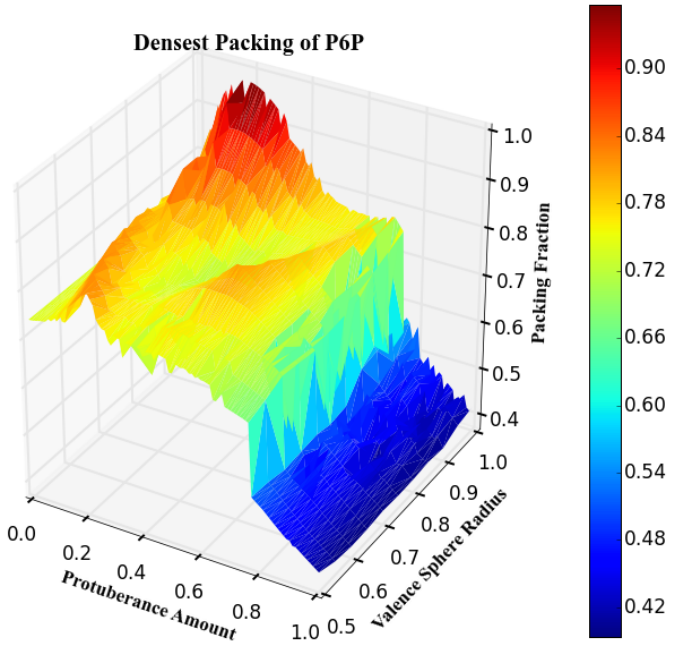

Figure 6.7: Densest packing surface of hexavalent (P6P) particles, at different radii of valence sphere, with increasing protuberance amount. The relatively lesser number of structures holds the promise of entropic self-assembly of these structures.

Across the various densest packing curves for all particle types, we observe these general trends. The extent of different packing structures varies with increasing amount of α. We observe that the structures formed are primarily spherical, due to the spherical composition of the building blocks. In the case of P2P, there are three different densest packing structures: FCC, BCT and two-dimensional tetragonal sheets with AB stacking. For P3P particles, we observe FCC, BCT and two-dimensional triangular sheets with AB stacking. For P4Pt particles, we observe FCC, BCT, and BCC structures. For P4Ps and P6P particles, we find FCC, BCT and two-dimensional square sheets. Also, we observe that in the cases of P4Ps and P6P, the densest packing curves are smooth at all values of r and α. This implies that the densest packing structures can be easily sheared into each other, thus increasing the propensity for their self-assembly by avoiding kinetic traps.

In the densest packing structures observed in Fig. 6.3 - Fig. 6.7, we note that the lattice distance in the unit cell varies as a linear function of the protuberance amount α. A hand waving argument regarding the observation of different structures can thus be made in the following manner: as the protuberance amount increases, the unit cell of the densest packing gradually shifts from a cubic to a tetragonal structure. With further increase in the protuberance amount, the tetragonal symmetry in the third dimension is also lost, resulting in the formation of two dimensional sheets that are stacked together in these structures.

Interestingly, as the radius r is increased, the inverse effect takes place. Thus the particles gain symmetry in their densest packing structures, improving from two dimensional sheets into tetragonal and cubic symmetries. Thus there is a maximum probability for the occurrence of a given structure between the limits of radius and protuberance amounts.

6.3.2 Self-Assembled Structures

In order to understand the relationship between the densest packing and self-assembly for sphere union particles, we perform Monte Carlo simulations of their assembly. The self-assembly of hard particles is driven by the maximization of shape entropy, which causes particles to arrange into locally dense packings [8].

Similar to the results we obtained for multi-dimpled spherical particles, we observe that at low protuberance amounts α, for all radius values, all particles behave like spheres. Here, the particles assemble into a rotator face-centered cubic crystal where there is no correlation between the orientations of neighboring particles, as shown in Fig. 6.8. The lattice unit vector of these crystals increases with increasing protuberance amount. As shown in Fig. 6.8 (b), these structures can be understood as open FCC lattices with entropic repulsive patches that stabilize the FCC structure.

Larger protuberances play a greater role in self-assembly. However, due to the large number of competing dense packing structures that neighboring particles locally assemble into, we do not assemble a crystal for P3P, P4Pt or P4Ps particles within the time scales of our simulation. P2P particles assemble into two-dimensional tetragonal sheets with AB stacking when the radius of the valence spheres is equal to the parent sphere. P6P particles readily assemble into the face-centered cubic lattice. This can be understood to originate in the spherical shape of the particle, as these particles are more spherical than others.

The rich variety of structures found in our densest packing results do not equate to an equally rich variety of crystal structures in assembly. On the contrary, the presence of competing locally dense packing structures seen in densest packing curves that cannot be sheared into one another results in kinetic arrests which hinder the assembly process.

For the case of P4Psq and P6P particles, we find interesting crystal structures at higher densities. The P4Psq particles form the A15 crystal structure at a packing fraction of 0.70 for small protuberance amount of 0.20, when the valence sphere radius is 1.0. At these parameters, the particle is disc like and has bumpy surfaces that result in a rotator crystal, as shown in Fig. 6.12.

The P6P particles are cubic by design. At relatively high packing fractions of 0.46, for particles with large protuberances at different valence sphere radius sizes, the particles

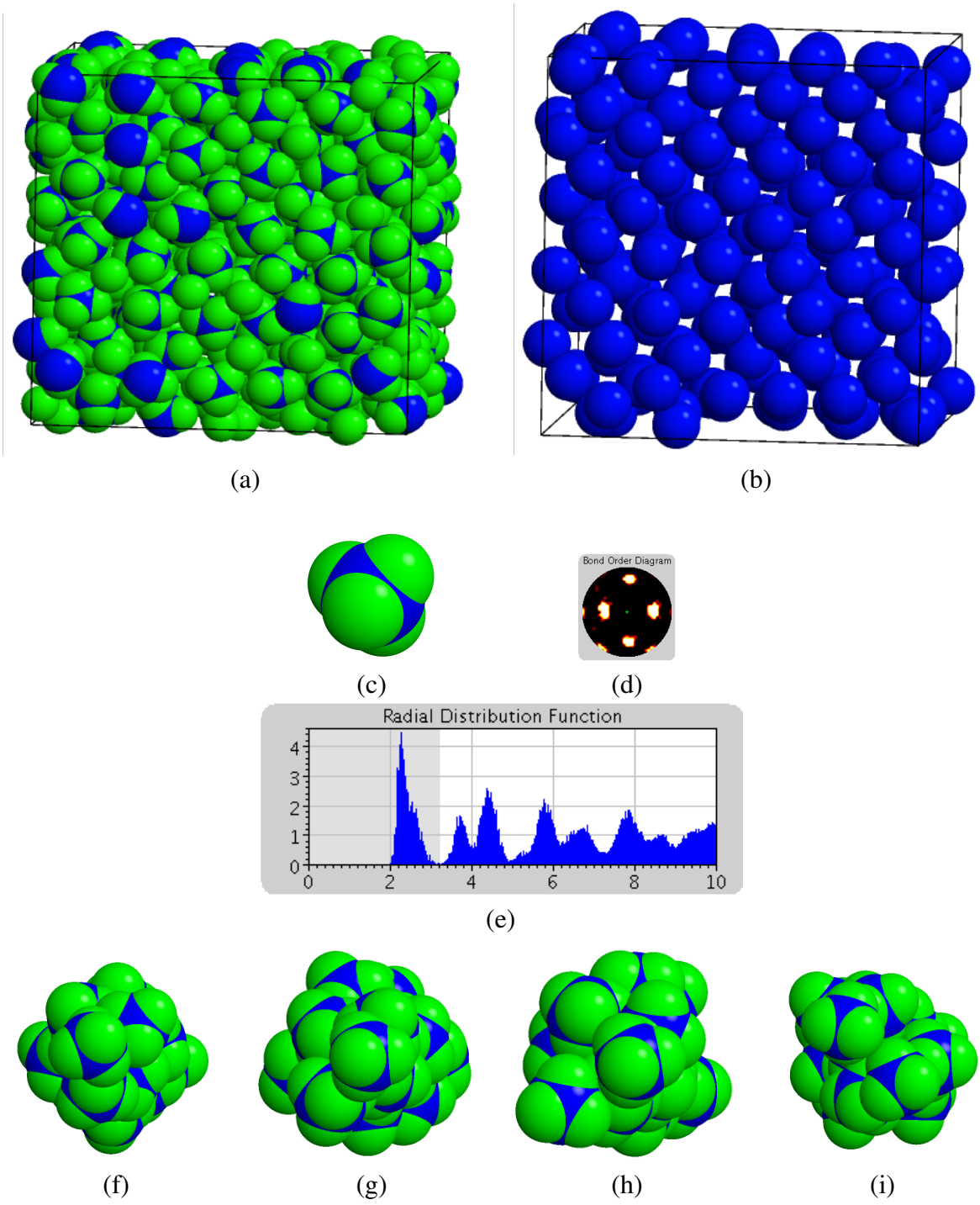

(a) (b) (c) (d) (e) (f) (g) (h) (i)

Figure 6.8: Self-assembly of an open, rotator, face centered cubic crystal by a tetrahedral sphere union particle at a packing fraction of 0.58. We show the bulk assembled structure in (a), and its open crystal structure (b). A single particle is shown in (c) for clarity, along with bond order diagram (d), and radial distribution function (e). In (f), (g), (h) and (i), we show independent simulation snapshots along z-axis of the crystal center that indicate a lack of correlation in particle orientation, thus indicating the presence of a rotator phase.

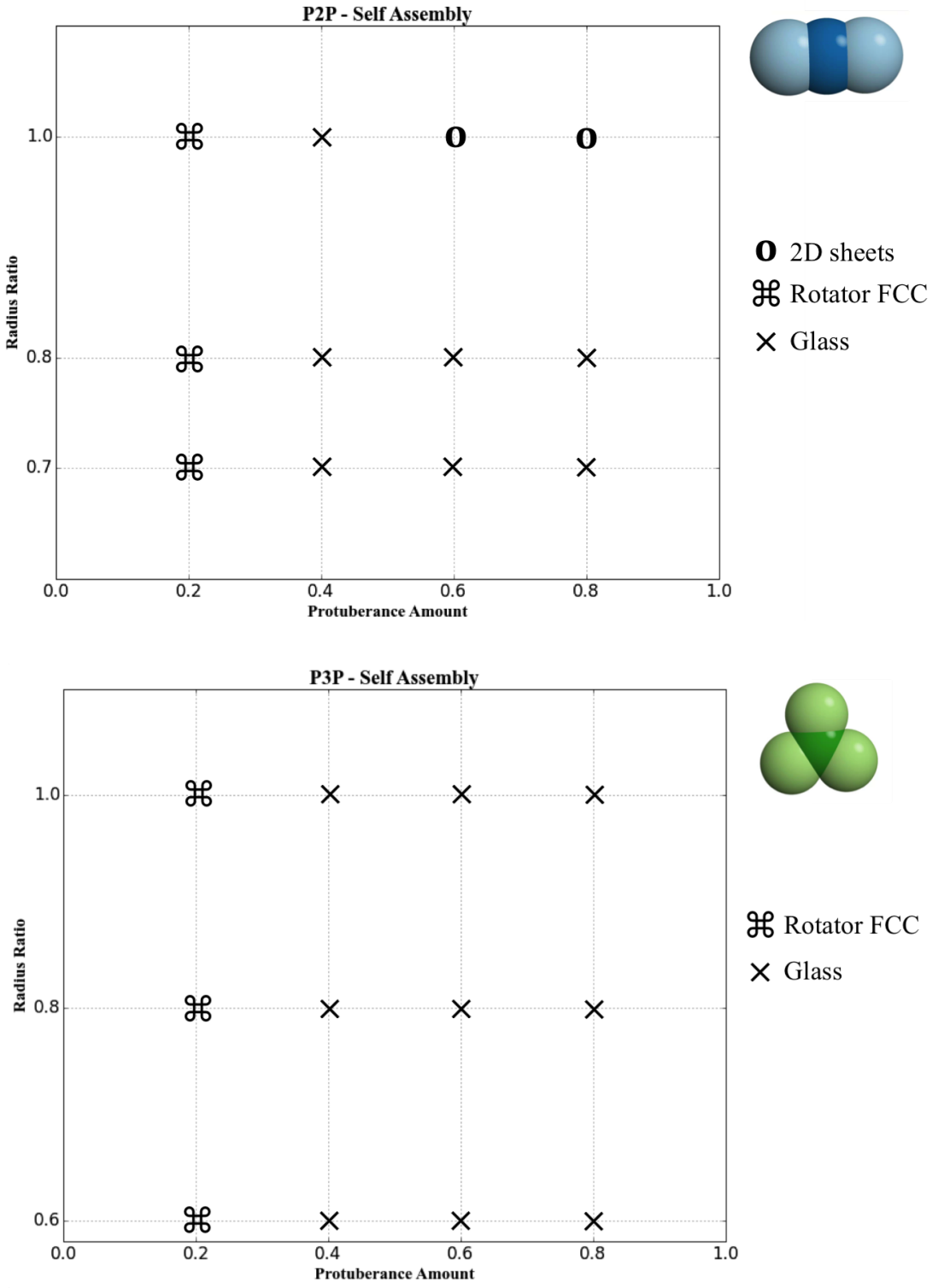

Figure 6.9: Self-assembly phase diagram of sphere union particles - P2P and P3P. We observe a rotator FCC lattice at small protuberance amounts for all families of particles. At higher protuberance amounts, we do not observe any crystal structures on the time scale of our simulations for P3P particles. For P2P particles, we observe two dimensional sheets of particles when $r = 1$.

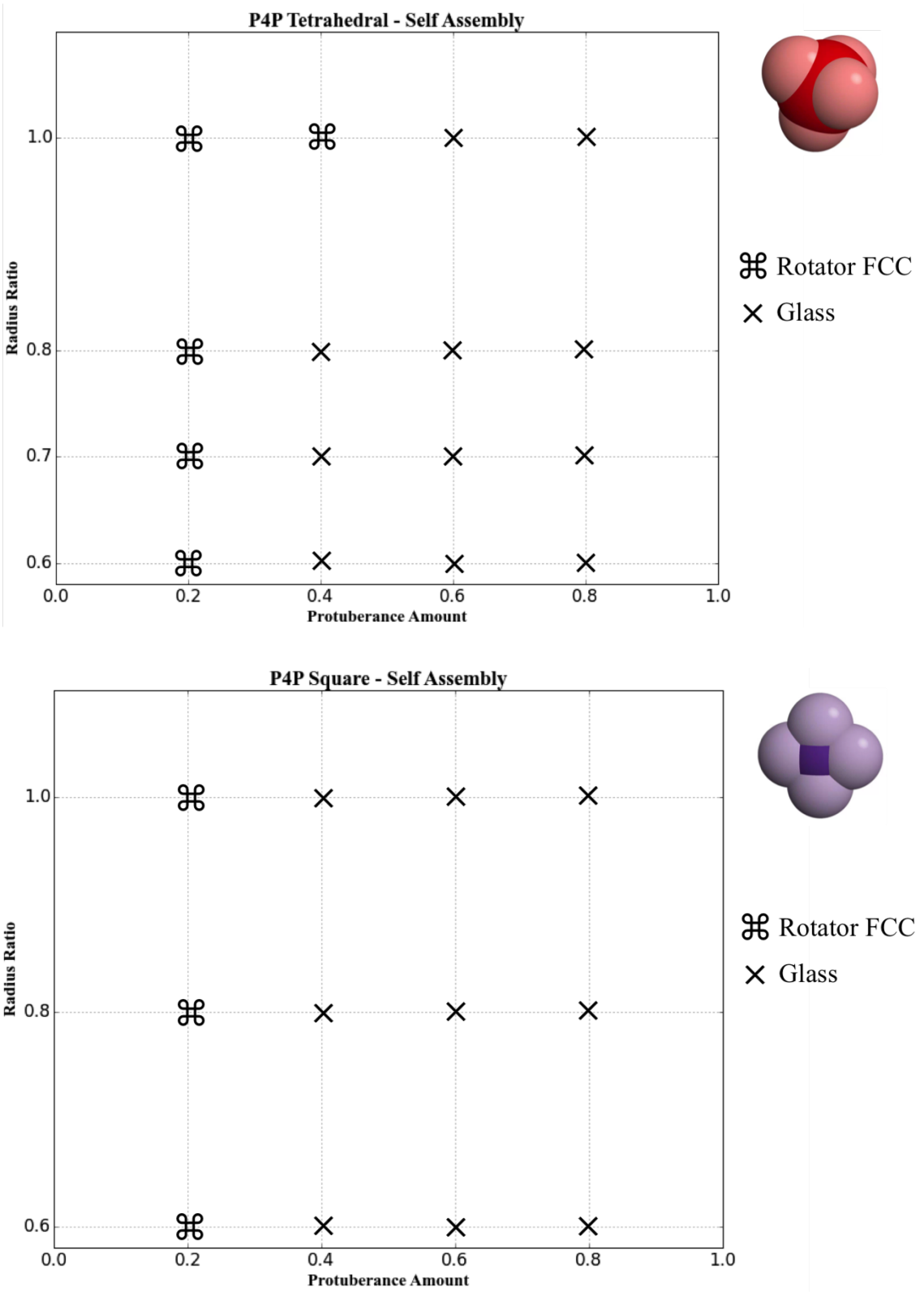

Figure 6.10: Self-assembly phase diagram of sphere union particles - P4Pt and P4Ps. We observe a rotator FCC lattice at small protuberance amounts for all families of particles. At higher protuberance amounts, we do not observe any crystal structures on the time scale of our simulations for P4Pt and P4Ps particles.

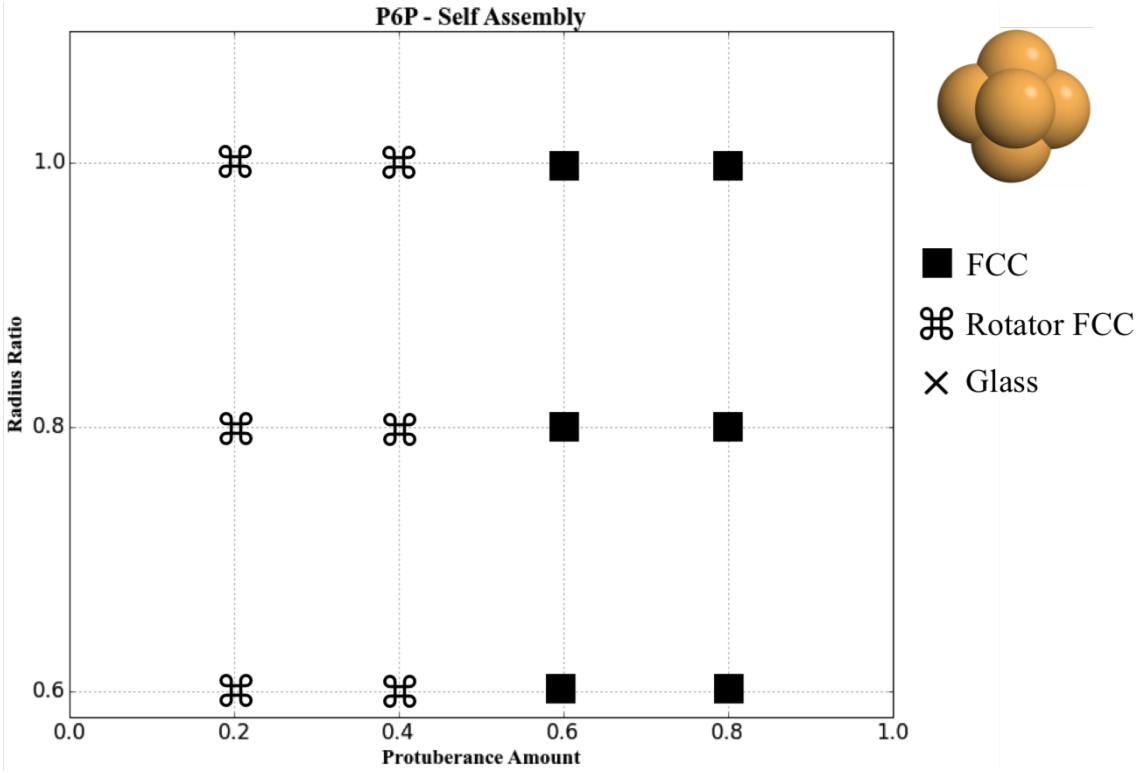

Figure 6.11: Self-assembly phase diagram of sphere union particles - P6P. We observe a rotator FCC lattice at small protuberance amounts for all families of particles. For P6P particles, we observe FCC structure even at high protuberance amounts due to the high spherical nature of these particles.

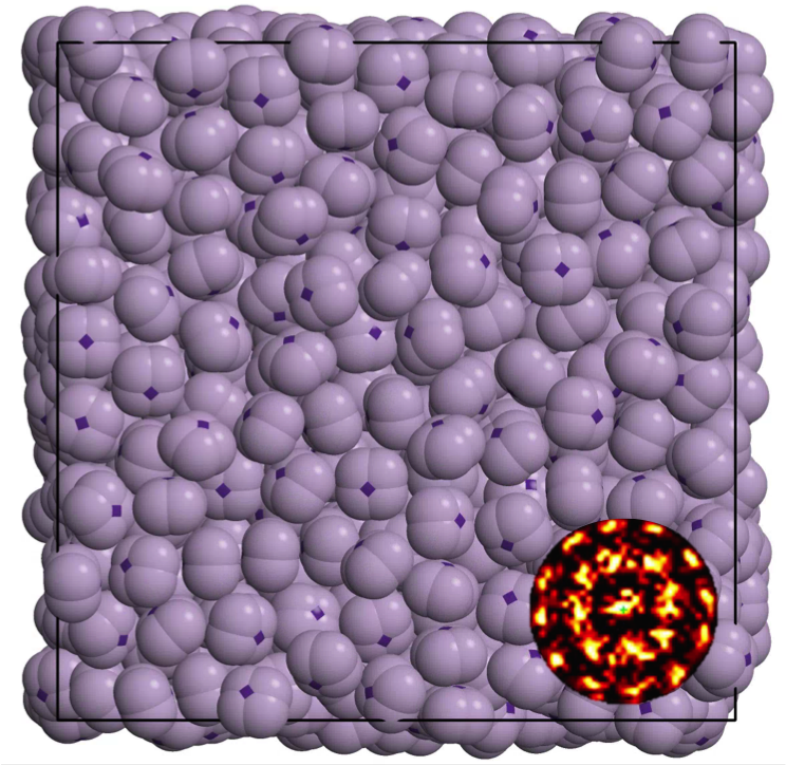

Figure 6.12: Self assembled A15 rotator crystal phase at dense packing fraction of P4Psq - square tetravalent sphere union particles. This structured was obtained at packing fraction of 0.70, for small protuberance amount of 0.20, and valence sphere radius equal to parent sphere.

readily assemble into a crystal with a hexagonal close packed lattice. This structure is unique as it does not exhibit a plastic crystal state - instead the particles align themselves both translationally and rotationally into the HCP lattice, as shown in Fig. 6.13. For both P4Psq and P6P particles, future work will be needed to flush out the entire phase diagram at higher packing fractions. We also expect to observe a rich variety of crystal structures from other particles at higher packing fractions.

6.4 Discussion

In this chapter, we discussed the densest packing and self-assembly of symmetric sphere union particles for varying sphere radii and protuberance amounts. We found that the densest packings of the particles change from FCC to structures dominated by the symmetry of the particles. The relative positions of these changes are determined by an interplay of both the radius and the protuberance amount. In general, the densest packing structures shift at

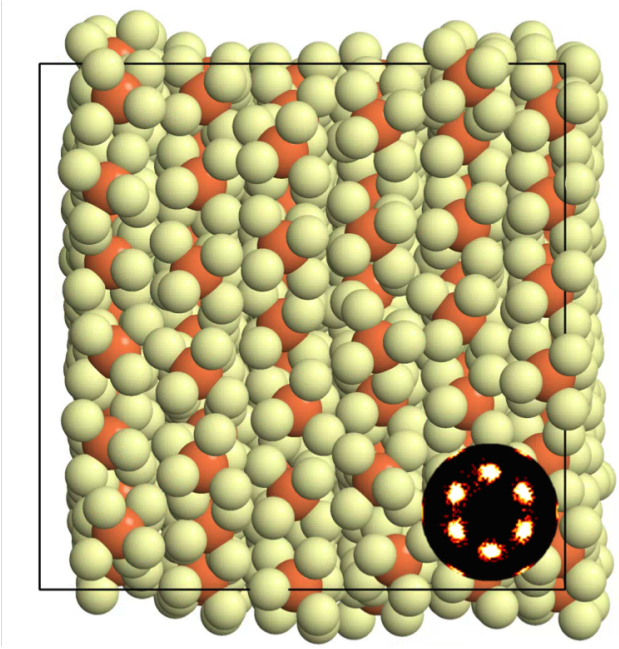

Figure 6.13: Self assembed hexagonal close packed (HCP) structure at relatively dense packing fraction of P6P - hexavalent sphere union particles. This structure was obtained at packing fraction of 0.46, for large protuberance amounts of 0.60 and 0.80 at different valence sphere radii.

different points for different values of radius and protuberance amounts.

Sphere union particles with small protuberance amounts equal to 0.20 always self-assemble into a rotator face-centered cubic lattice. This can be understood from the work in Chapter 5. At these small protuberance amounts, the isotropic nature of the spherical particle is not disturbed. This results in a mostly isotropic potential of mean force and torque in the neighborhood of these particles. These structures hold the promise of applications involving open crystal structures. For example, consider a particle that is made of an optically opaque parent sphere with optically transparent valence spheres. These particles, as shown in Fig. 6.8 (b), would serve as an open crystal to the wavelength of light. Further extensions of such work can be aimed at building open diamond crystals from similar building blocks.

At higher protuberance amounts, the potential of mean force and torque is dominated by geometric features that determine the neighborhood of a particle. We observe that in the case of sphere unions of six valence spheres (P6P), the particles readily assemble into a face-centered cubic structure. In the case of sphere unions of two valence spheres (P2P), the particles form two dimensional tetragonal sheets in an AB stacking. For all other particle types in this study, the assemblies are found to be kinetically arrested on the time scale of

our simulations. We attribute this observation to our finding of a large number of competing local dense packing structures in the densest packing calculations for these particles.

The observation of a rich variety of densest packing structures implies that these particles can be stabilized into a number of structures, at least in the limit of infinite pressure. While entropic means might not suffice to achieve these structures, the introduction of enthalpic patchy sites on these particles can be used to promote their assembly into different crystal structures. In the context of protein crystal self-assembly, most progress has relied on the "patchy sphere" model, for which the patch locations can be chosen to match experimentally determined, e.g. orthorhombic, unit cell assembles with defined molecular orientations. Many of the crystal structures formed by proteins are open crystal structures. By using patchy sphere models with two different types of spheres, one to model the protein molecules and another to model the void space in open crystals, these models can be used to stabilize protein structures. Some of these spheres can also be modeled as soft spheres to successfully model the behavior of proteins without the explicit inclusion of enthalpic interactions that make the system computationally expensive. These soft spheres would have a tolerance in their overlap allowing for an accurate representation of proteins, possibly resulting in a better understanding of the folding of protein molecules.

We proposed these particles as colloidal molecules. In this sense, we have only exploited their shape. By adding surface charge, we could introduce interactions between these building blocks. Further work on controlling the interactions along the various geometric aspects of these particles can be performed by tuning their sizes. This holds the promise of reconfigurable structures that can be obtained due to small changes in the interactions of their building blocks.

CHAPTER 7

Summary

> God used beautiful mathematics in creating the world.
>
> Paul M. Dirac

7.1 Conclusions

In this thesis, we considered shape modifications to spheres in order to introduce directional entropic forces. All of these shape modifications have been experimentally realized, thanks to experimental progress in the synthesis of spheroidal particles.

We considered the effect of a sea of depletants surrounding a pair of particles, which results in an osmotic pressure around the particles. We quantified the effective potential of mean force and torque (PMFT) around a colloidal particle in both its fluid and solid states. By understanding the effect of depletion, we showed that emergent binding at low colloidal concentrations can be activated through depletants. Specifically, the colloidal particles bind in a manner that increases the free volume available to the depletants in the system.

Next we considered the question of flat facetted spheres. While it is known that flat facets promote binding and can assemble into a number of structures, particles with true flat facets are difficult to experimentally synthesize. Thus we asked the question "How flat is flat?", understanding the effect of curvature on the assembly of particles. We answered this question in the presence of depletants - by first numerically calculating the free volume available to the depletants in a given configuration of collodial particles. We expect the structure with a larger free volume for the depletants to be more readily assembled in bulk. We found this to be true in the case of low colloid concentrations, where the entropy maximization of depletants plays a bigger role than the entropy maximization of colloidal particles towards the total gain of entropy for the system. Thus we were able to deter-

mine depletant sizes that can promote a targeted binding configuration between colloidal particles.

Concave features on the surfaces of spheres are a prime example of directional entropic patches. We thus extended our previous work to consider simulations of multi-dimpled spherical particles. By evaluating the densest packing curves and self-assembly structures of these particles, we found a crossover in their behavior that originates in the competition between convex and concave regions of the particles. In particular, we found that the densest packings cross over into structures dominated by their concave regions at a critical total dimple circumference to depth ratio. This emphasizes the notion that densest packing is a global effect of all features in particles. We found a similar crossover into concave feature driven assembly from sphere like assembly at a critical individual volume of the dimple. This emphasizes the notion that self-assembly is a locally driven effect, with neighboring particles finding locally dense packings. These results have an important effect on understanding emergent phenomena, as entropic interactions are an emergent behavior that occur due to the crowding of neighboring particles. The ability to *a priori* determine emergent phenomena holds the promise of better control over the design of such phenomena.

Finally, we considered the inverse of multi-dimpled spherical particles, *i.e.*, sphere union particles. By replacing dimples with bumps, we proposed the notion of directional entropic repulsive forces for creating open crystal structures. These particles are a direct extension of hard dumbbell and snowman shaped particles. We found densest packing curves for these particles at different radii and protuberance amounts. Interesting trends were found, with close packed structures like face centered cubic, body centered tetragonal and body centered cubic forming at larger lattice spacings. In the self-assembly simulations, we found that at low protuberance amounts, the lattice spacing of face-centered cubic crystals can be finely controlled by these particles. At higher protuberance amounts, in general, the particles were kinetically arrested in their assembly due to the large number of competing densest packing structures. These particles hold the promise of a facile synthesis method for the development of colloidal molecules, *i.e.*, analogues to molecular atoms, that can be designed to have surfaces with different interaction strengths.

By studying the different axes of shape modification, we have exploited the ability to tune directional entropic forces in the design of colloidal particles for targeted development of crystal structures.

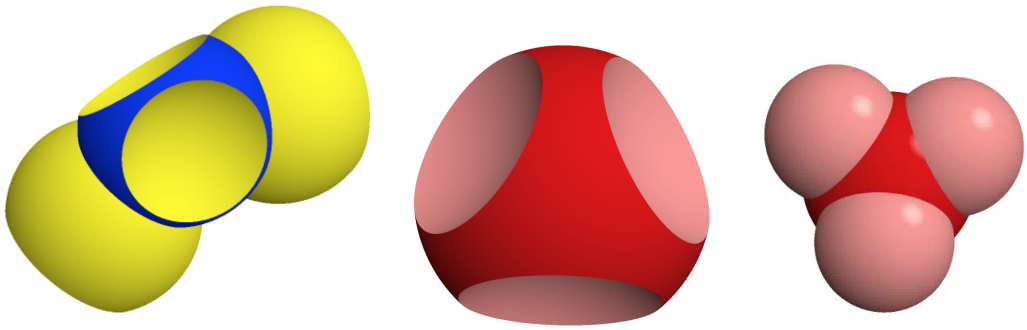

(a) (b)

Figure 7.1: Heterogeneous features (dimple - protuberance) on a single particle (a) or a mixture of complementary particles (b) can provide interesting opportunities to understand the interplay of directional entropic forces.

7.2 Future Work

7.2.1 Heterogeneous Features

An interesting avenue to consider for future work is the mixture of various shape features in a spherical particle. These could be a mixture of convex and concave features in a single particle, or mixtures of two particles with complementary features, as shown in Fig. 7.1. The interplay of particle features here can result in interlocking of double lattices as well as the formation of two independent crystal structures. This and other possibilities provide a great motivation to study such systems.

7.2.2 Entropy + Enthalpy

Introducing interactions between particles by selectively decorating certain shape modifications is an interesting step forward, bringing together both enthalpic and entropic patches to design new crystal structures. The ability to tune particle shape through means of swelling and shrinking the particles can help in fine, *in situ* control of enthalpic interaction energies. We have proposed this concept for facetted particles in Fig. 7.2. This can be extended in a straightforward manner to the various shape modifications of spheres that have been performed in this work.

7.2.3 Modeling Proteins

Representing folded protein molecules as nanoparticle building blocks is a promising strategy to explore the tremendous design space of functionalized biomaterials. Proteins are

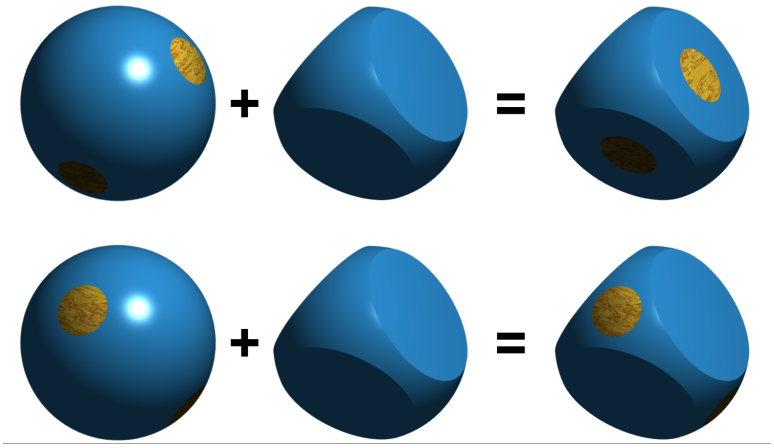

Figure 7.2: Enthalpic patches can be combined with entropic patches to enhance or inhibit entropic patchiness as shown schematically here. This can be obtained by using the same direction for both types of patches (top), or by using different directions for the entropic patches and the enthalpic patches (bottom). Figure reproduced from [3].

well known to form crystalline materials, and the more than 80,000 structures of the Protein Data Bank (PDB) that have been found by x-ray crystallography are testimony to the importance of protein crystallization for structural biology. Assigning a three-dimensional shape to a protein, defined by the spatial extent of its constituent atoms, can help us take advantage of the knowledge of various principle of patchy particles. By using a three-dimensional 'patchy shape' model, where the patchy interactions of the model will be calibrated through feedback with experiment, a better understanding of the fundamental mechanisms in protein crystal formation can be achieved.

The questions that were opened during this work revolve around system complexity. By introducing many more features in the shape of particles, we can expect the number of possibilities to get further complicated. New approaches to the computational study of these systems would be needed. Machine learning and other learning algorithms can be designed to help narrow down the search space for a targeted structure. The future of computational design for targeted self-assembly of materials is at the crossroads of improved parameter space search techniques and new building blocks that can be readily synthesized experimentally.

APPENDIX A

PMFT for Rounded Cylinders

We understand that non-specific interactions form and break easily in comparison to specific interactions. This suggests that non-specific interactions can function as a route to specific binding in these systems. In Fig. A.1 and Fig. A.2 we plot this potential to compare the effect of different particle shape features. Figure A.1 compares the potential of mean force and torque at a fixed value of the temperature and pressure for a rounded cylinder and a true cylinder (see Fig. 3.2 for a depiction of the geometric understanding of the coordinates and Fig. 3.4 for a depiction of the rounded cylinders themselves).

We show this in figure A.2 in which we plot the potential of mean force at $\phi_{1,2} = (-0.999, -0.999), (-0.578, -0.578), (-0.578, -0.999), (-0.999, -0.578)$ for cylinders at $r_d^3 P/k_B T = 0.015$ and 0.04. We can clearly see that the potential becomes deeper near specific patch sites at higher pressures.

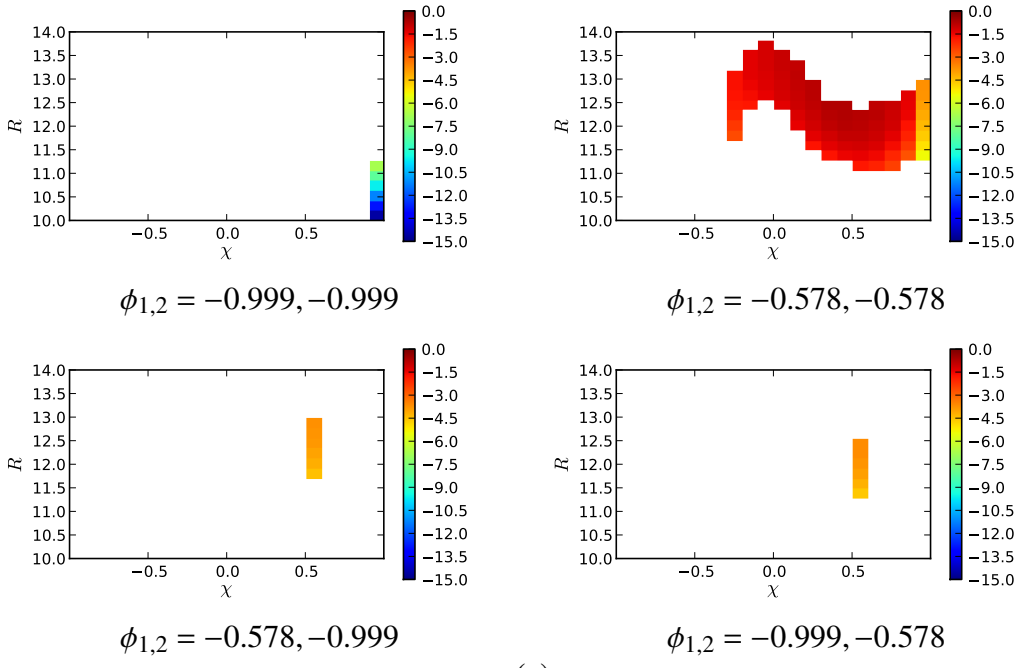

(a)

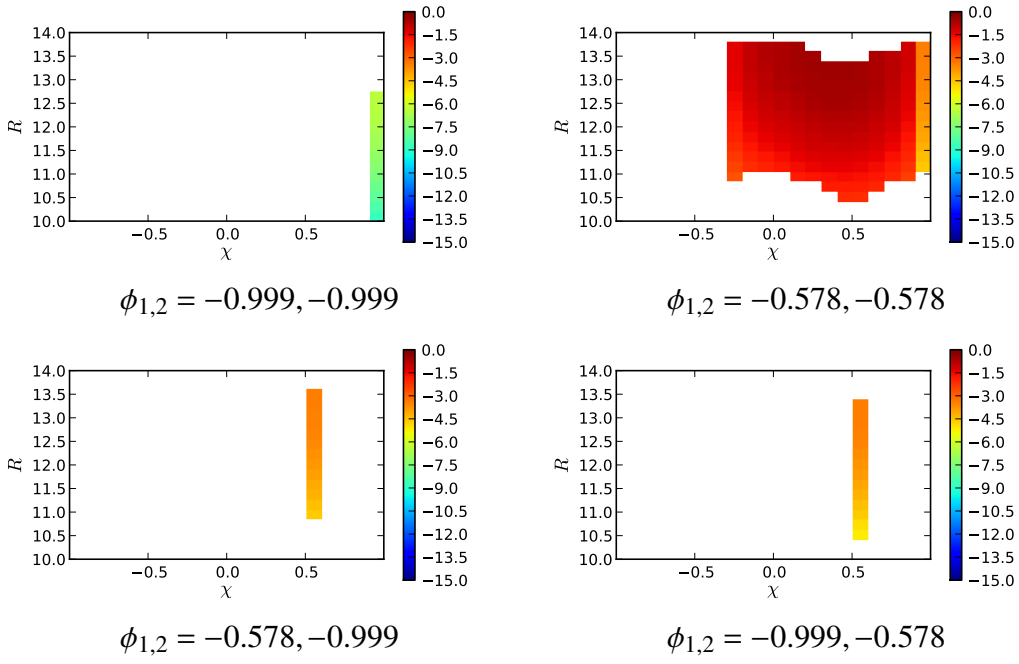

(b)

Figure A.1: Plot of the potential of mean force and torque for a true cylinder (a) and a rounded cylinder (b) in units of $k_{\mathrm{B}}T$. In the former case the diameter of the cylinder is the same as its height. In all cases the maximum radius of a sphere that can be inscribed within the shape is fixed to ten times the radius of the depletant. The true cylinder leads to a more highly anisotropic interaction potential with a deeper minimum near facial alignment than the rounded cylinder.

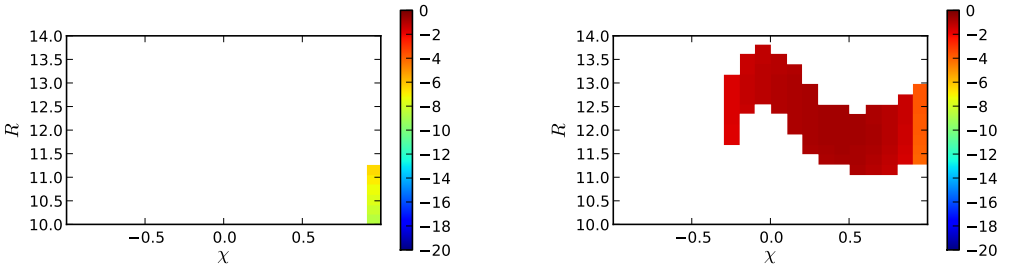

$\phi_{1,2} = -0.999, -0.999, P = 0.015$ $\phi_{1,2} = -0.578, -0.578, P = 0.015$

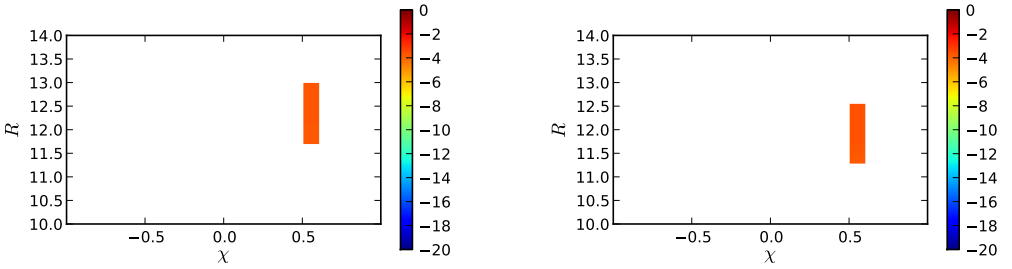

$\phi_{1,2} = -0.578, -0.999, P = 0.015$ $\phi_{1,2} = -0.999, -0.578, P = 0.015$

(a)

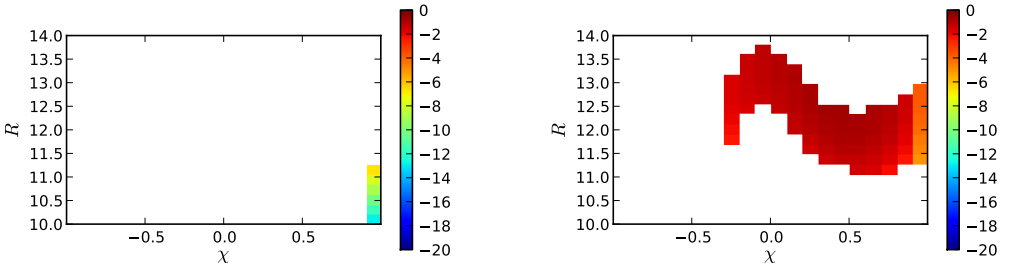

$\phi_{1,2} = -0.999, -0.999, P = 0.04$ $\phi_{1,2} = -0.578, -0.578, P = 0.04$

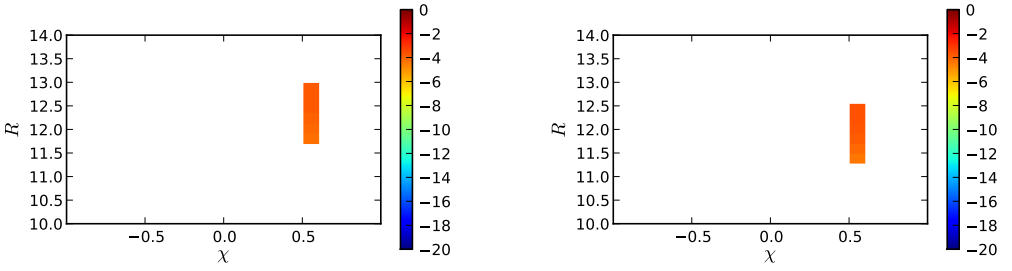

$\phi_{1,2} = -0.578, -0.999, P = 0.04$ $\phi_{1,2} = -0.999, -0.578, P = 0.04$

(b)

Figure A.2: Plot of the potential of mean force and torque for a true cylinder at $r_d^3 P = 0.05$ with $k_B T = 1.5(a), 3.0(b)$, where the diameter of the top is ten times the depletant diameter. Note that at higher depletant pressures the specific (i.e. end-to-end) binding becomes more favourable.

APPENDIX B

Densest Packing of Concave Spheres

B.1 Analytic Calculations of Densest Packings

To verify the putative densest packing predicted computationally via MC simulations for the particles studied in Chapter 5, analytic calculations of the packings of these particles were performed. In Figures B.1 - B.5, we plot analytic calculations of the packing curve and numerically predicted packings for one and two particles of all particle types. We show that our numerical calculations match very well with the analytic findings, with an error less than 0.001% when $f \geq 0.10$.

We further numerically calculate maximum packing densities of all particle types with up to eight particles. However, due to the complexity of the analytic packing problem for number of particles $n \geq 3$, we do analytic calculations only for (some) one- and two-particle packings ($n = 1, 2$) for different particle types. If solvable, these analytic curves and intersection equations are shown in Figures B.1 - B.5.

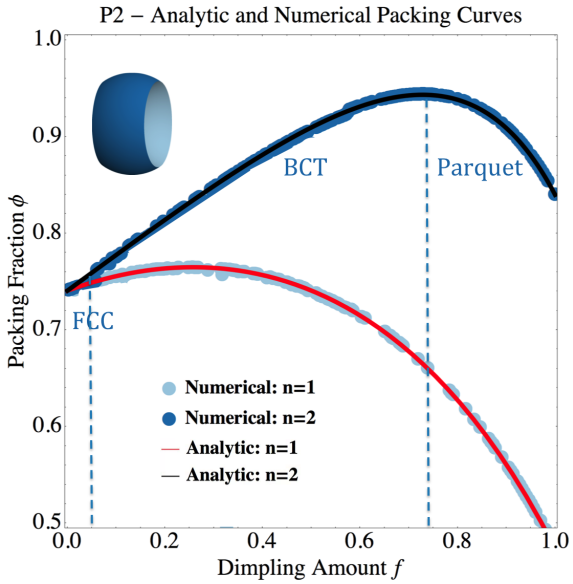

Figure B.1: Analytic and numerical packing curves showing a perfect fit for bivalent particle (P2) for one and two particles in a box. Analytic packing curve for one particle is shown in red, two particles in black. The dark markers denote numerical densest packing calculations for two particles in a box, and light for one particle. Blue dashed lines show the different packing regions found in numerical calculations.

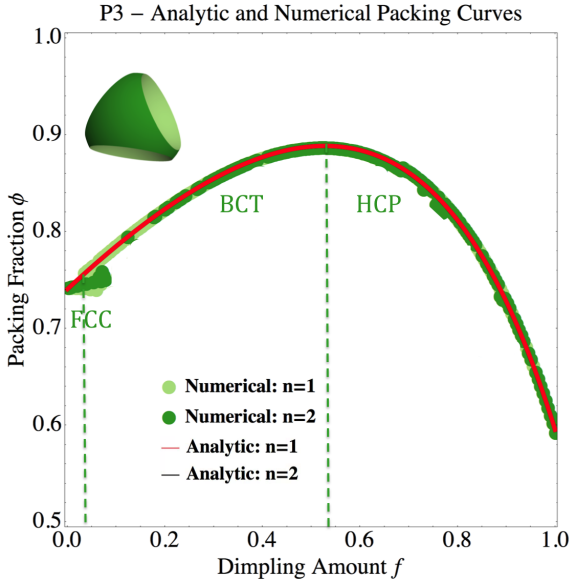

Figure B.2: Analytic and numerical packing curves showing a perfect fit for trivalent particle (P3) for one and two particles in a box. The curves overlap as one and two particles pack in the same manner. Green dashed lines show the different packing regions found in numerical calculations.

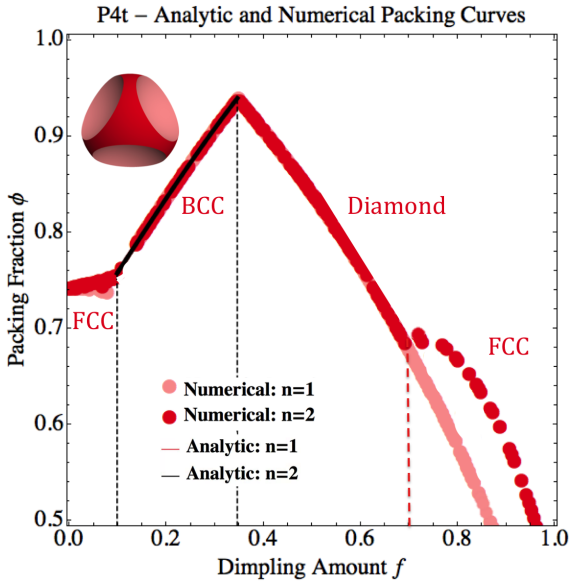

Figure B.3: Analytic and numerical packing curves showing a perfect fit in a single region between black dashed lines for tetrahedral tetravalent particle (P4t) of one and two particles in a box. Analytic packing equations could not be calculated at all dimpling amounts by analytic means. Red dashed lines show the different packing regions found in numerical calculations, in addition to those found in analytic calculations.

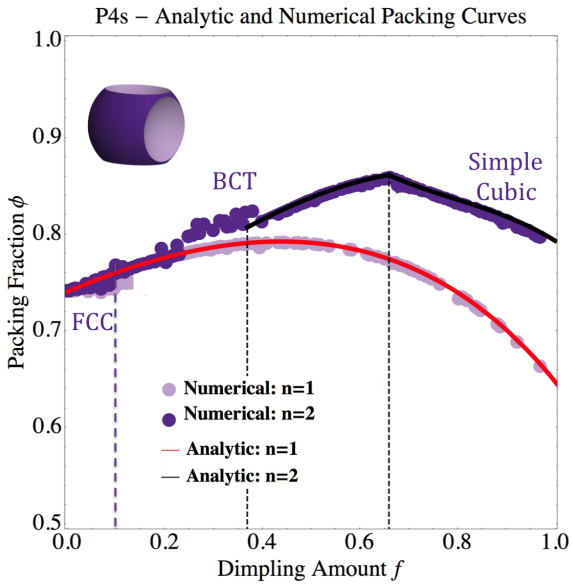

Figure B.4: Analytic and numerical packing curves of a square tetravalent particle (P4s) showing a perfect fit in the entire domain for one particle in a box and between black dashed lines in two regions for two particles in a box. Analytic packing curves could not be calculated at all dimpling amounts for two particles by analytic means. Magenta dashed lines show the different packing regions found in numerical calculations, in addition to those found in analytic calculations.

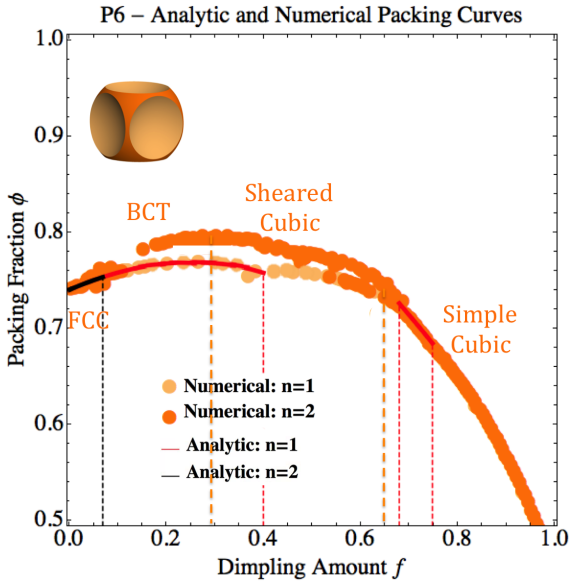

Figure B.5: Analytic and numerical packing curves of a hexavalent particle (P6) showing a perfect fit between red dashed lines in two regions for one particle in a box and between black dashed lines in one region for two particles in a box. Analytic packing curves could not be calculated at all dimpling amounts for two particles by analytic means. Orange dashed lines show the different packing regions found in numerical calculations, in addition to those found in analytic calculations.

APPENDIX C

Self-assembly of Concave Spheres

C.1 Hard to Soft Transition

In Chapter 5, we note that small concave variations to the shape of a hard sphere have a similar effect to introducing soft interactions on spheroidal particles. Our results demonstrate that in the family of particle shapes we consider, with increasing dimple size, we first observe a structural change from FCC to BCT in packing and to BCC in assembly, at a small dimpling amount, before undergoing a subsequent change to a structure dependent on the anisotropic nature of the dimples.

In order to explicitly show the transition from FCC to BCC in assembly, we include in Fig. C.1 the g(r) calculation near FCC to BCC transition for a tetrahedrally tetravalent particle. At a constant packing fraction of 0.63, we report a change in the $g(r)$ from FCC to BCC structure for an infinitesimal dimple volume (hard sphere) to a finite dimple volume respectively.

C.2 Valence of Multi-Dimpled Particles

By means of PMFT calculations [8], we report that neighboring particles bind along the direction of dimples during self-assembly (Figs. 5.7 - 5.8). The self-assembled crystal structures have an emergent valence dependent on the geometry of the dimples due to the interlocking of convex and concave regions. However, in the diamond crystal structure obtained from tetrahedrally tetravalent (P4t) particles, the dimples align facing each other. This is primarily caused by self-depleting effects from neighboring particles when seeded, that we report in our previous work [8]. Hence, there is considerable empty volume between the particles, resulting in a much lower packing fraction of $\phi = 0.32$ than is evident from the structure. Nevertheless, the emergent valence of these particles in their crystal structure is governed by the dimple geometry as shown from PMFT calculations.

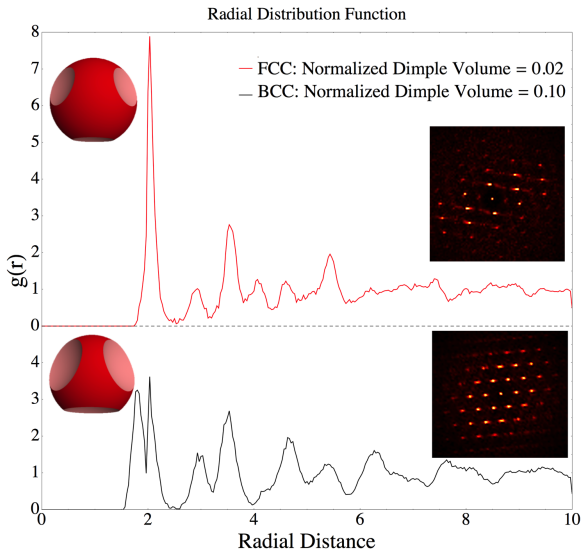

Figure C.1: The radial distribution function of tetrahedrally tetravalent particles (P4t) at negligible dimple volume (above) and small dimple volume (below). We report a transition from a face-centered cubic to a body-centered cubic crystal structure as volume of the dimple increases.

C.3 Critical Dimpling Amount

Table C.1: Crossover Values for Putative Densest Packings and Thermodynamic Assemblies

Particle	f^*_{DP}	C_d	f^*_{SA}	v_d
P2	0.73	1.21	0.50	0.104
P3	0.53	1.22	0.48	0.070
P4t	0.37	1.20	0.60	0.107
P4s	0.56	1.32	0.82	0.105
P6	0.27	1.26	0.64	0.070

The critical dimpling amount for the putative densest packing f^*_{DP} and self-assembly f^*_{SA} of each member of the sphinx family is calculated as the crossover point in the corresponding particle behavior. At these crossover values, different geometric characteristics of each member of the sphinx family have been calculated as shown in Table C.1.

To understand the packing of multi-dimpled spheroidal particles, we determine the primary feature in the shape of these particles that affects their behavior. We investigate the value of f^*_{DP} compared to the total volume V_d, surface area S_d and circumference C_d of all dimples on a single particle as d is varied. We normalize each of these three parameters.

The volume and surface area are normalized by the remaining respective quantity in a single particle, while the circumference is normalized by the circumference of a circle with radius equal to the distance between the central and valence spheres, a linear function of the depth of the dimple. We compute the total normalized dimple volume, surface area and circumference to depth ratio in each family of particle at f^*_{DP}. We find that the total circumference to depth ratio C_d of the dimples is 1.2341 ± 0.060 at f^*_{DP} across all five particle families; see figure in main text. In contrast, no universal behavior was found for dimple volume or surface area. This scaling behavior is also understood from the geometry of the putative densest packings. The observed critical crossover in the packing curves of these particles is a result of the presence of convex and concave features in their shape. We report that this criticality is a constant for particles of different dimple geometries, because packing is a global effect. However, calculating the geometry of this interlocking is a non-trivial problem that cannot be easily generalized as it depends on the number of dimples and their geometry.

We also observed that in their assembly, all particle types undergo a structural transition from BCC into a thermodynamic phase dictated by their concave features. To quantify when the concave features are sufficient to induce a change in the preferred structure, we compare particle shape characteristics at the critical dimpling amount for self assembly f^*_{SA}. We find that, across particle types, v_d shows little variation at f^*_{SA}, which suggests that *the volume of individual dimples controls assembly behavior, independent of particle type.*

C.4 Transition Density

The particles studied in this work assemble at approximately the same conditions. For the sake of completeness, we show the transition density phase diagrams for thermodynamic self-assembly of each particle in Figures C.2 – C.6. In these plots, we also observe the reported behavior of a crossover in the assembly of particles beyond a constant critical volume of a single dimple in the top axis.

These crystal structures are formed by entropic interactions between the convex and concave regions of two adjacent particles. We find that the emergent valence is dependent on the geometry of the dimples. The number of directions for the alignment of the particles depends on the crystal lattice, for example, two in the parquet structure. It should also be noted that the particles have rotational symmetries, which align with the symmetry of the crystals and thus do not break the symmetry of the crystals. In the case of the tetrahedrally tetravalent particle, particles have two orientations in the diamond crystal structure formed.

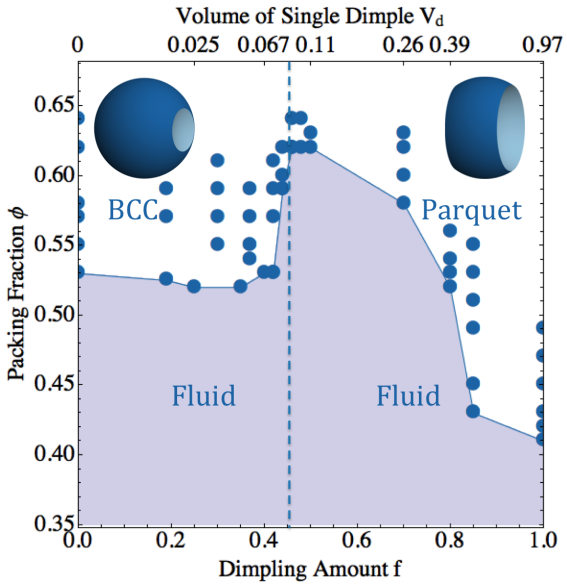

Figure C.2: Numerical packing curves showing a transition from FCC to BCC structures. This new transition, where new packing configurations (BCC) are accessible at higher dimpling amount f, occurs in concave particles where the change in particle shape is accompanied by a change in the void formed between particles in their densest packing. Blue dashed lines show the different packing regions found in numerical calculations.

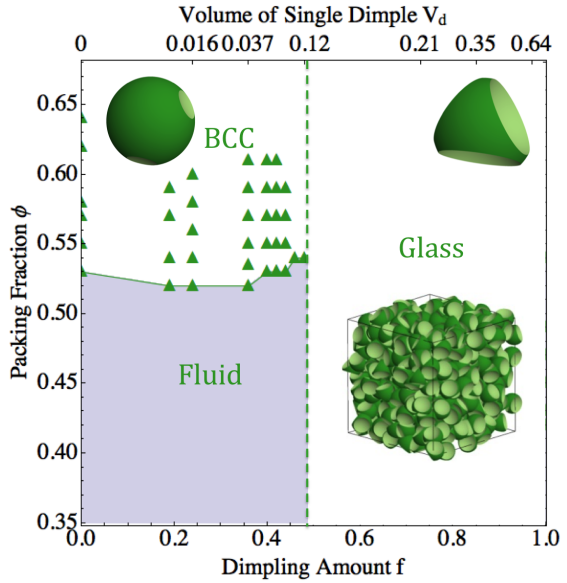

Figure C.3: Numerical packing curves showing a transition from FCC to BCC structures. This new transition, where new packing configurations (BCC) are accessible at higher dimpling amount f, occurs in concave particles where the change in particle shape is accompanied by a change in the void formed between particles in their densest packing. Green dashed lines show the different packing regions found in numerical calculations.

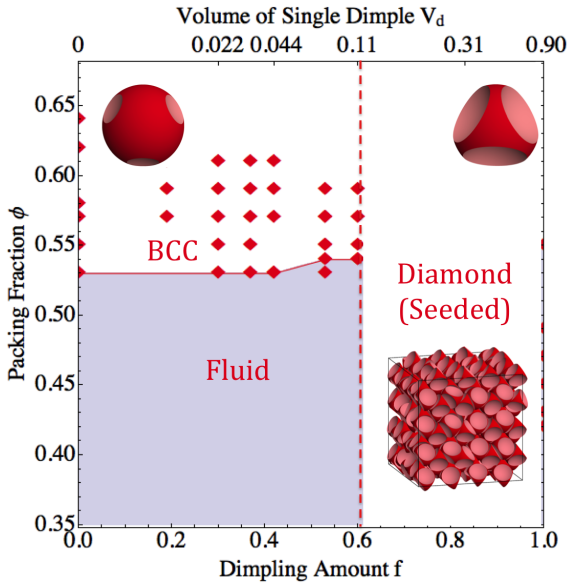

Figure C.4: Numerical packing curves showing a transition from FCC to BCC structures. This new transition, where new packing configurations (BCC) are accessible at higher dimpling amount f, occurs in concave particles where the change in particle shape is accompanied by a change in the void formed between particles in their densest packing. Red dashed lines show the different packing regions found in numerical calculations.

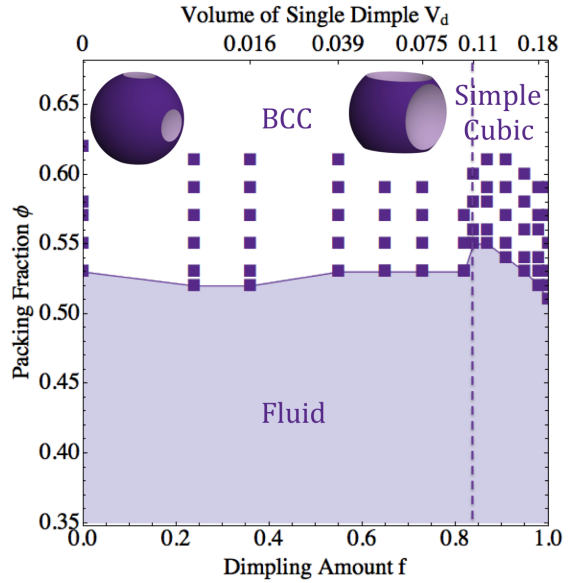

Figure C.5: Numerical packing curves showing a transition from FCC to BCC structures. This new transition, where new packing configurations (BCC) are accessible at higher dimpling amount f, occurs in concave particles where the change in particle shape is accompanied by a change in the void formed between particles in their densest packing. Magenta dashed lines show the different packing regions found in numerical calculations.

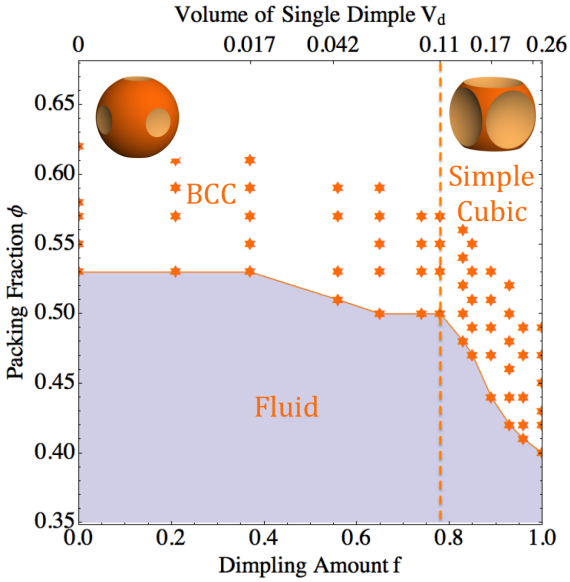

Figure C.6: Numerical packing curves showing a transition from FCC to BCC structures. This new transition, where new packing configurations (BCC) are accessible at higher dimpling amount f, occurs in concave particles where the change in particle shape is accompanied by a change in the void formed between particles in their densest packing. Orange dashed lines show the different packing regions found in numerical calculations.

BIBLIOGRAPHY

[1] Jankowski, E. and Glotzer, S. C., "Screening and designing patchy particles for optimized self-assembly propensity through assembly pathway engineering," 2012. vii, 2

[2] Glotzer, S. C. and Solomon, M. J., "Anisotropy of building blocks and their assembly into complex structures." *Nat. Mater.*, Vol. 6, No. 8, Aug. 2007, pp. 557–62. vii, 3, 4, 34, 41, 57

[3] van Anders, G., Ahmed, N. K., Smith, R., Engel, M., and Glotzer, S. C., "Entropically patchy particles: engineering valence through shape entropy." *ACS Nano*, Vol. 8, No. 1, Jan. 2014, pp. 931–40. vii, x, xiii, 4, 32, 41, 58, 60, 61, 75, 93

[4] Lekkerkerker, H. N. W. and Tuinier, R., *Colloids and the Depletion Interaction*, Springer, Dordrecht, 2011. vii, 5, 6, 7, 20

[5] Gray, H., *Anatomy of the human body*, Philadelphia: Lea & Febiger, 1918. vii, 7

[6] Anderson, J. A., Lorenz, C. D., and Travesset, A., "General purpose molecular dynamics simulations fully implemented on graphics processing units," *J. Comput. Phys.*, Vol. 227, No. 10, May 2008, pp. 5342–5359. vii, 11, 14, 15, 18, 77

[7] Chen, E. R., "picturebook guide to the SPHINX galaxy," *preprint*, 2014. vii, 11, 14, 16, 18, 44, 63

[8] van Anders, G., Klotsa, D., Ahmed, N. K., Engel, M., and Glotzer, S. C., "Understanding shape entropy through local dense packing," *Proc. Natl. Acad. Sci.*, Vol. 111, No. 45, Oct. 2014, pp. E4812–E4821. viii, x, xi, 6, 19, 20, 21, 24, 31, 32, 38, 39, 41, 44, 53, 56, 57, 60, 61, 63, 70, 71, 72, 73, 74, 75, 78, 82, 101

[9] Wang, Y., Wang, Y., Zheng, X., Yi, G.-R., Sacanna, S., Pine, D. J., and Weck, M., "Three-dimensional lock and key colloids." *J. Am. Chem. Soc.*, Vol. 136, No. 19, May 2014, pp. 6866–9. x, 56, 61, 74

[10] Whitesides, G. M. and Boncheva, M., "Beyond molecules: self-assembly of mesoscopic and macroscopic components." *Proc. Natl. Acad. Sci. U. S. A.*, Vol. 99, No. 8, April 2002, pp. 4769–74. 2, 3, 4

[11] Glotzer, S. C., Solomon, M. J., and Kotov, N. a., "Self-assembly: From nanoscale to microscale colloids," *AIChE J.*, Vol. 50, No. 12, Dec. 2004, pp. 2978–2985. 2, 3

[12] Pelesko, J., *Self Assembly The Science of Things That Put Themselves Together*, Chapman and Hall/CRC, 2007. 2, 3

[13] LeBard, D. N., Levine, B. G., Mertmann, P., Barr, S. a., Jusufi, A., Sanders, S., Klein, M. L., and Panagiotopoulos, A. Z., "Self-assembly of coarse-grained ionic surfactants accelerated by graphics processing units," *Soft Matter*, Vol. 8, No. 8, 2012, pp. 2385. 2

[14] Stoykovich, M. P., Müller, M., Kim, S. O., Solak, H. H., Edwards, E. W., de Pablo, J. J., and Nealey, P. F., "Directed assembly of block copolymer blends into nonregular device-oriented structures." *Science*, Vol. 308, No. 5727, 2005, pp. 1442–1446. 2

[15] Tang, C., Lennon, E. M., Fredrickson, G. H., Kramer, E. J., and Hawker, C. J., "Evolution of block copolymer lithography to highly ordered square arrays." *Science*, Vol. 322, No. 5900, 2008, pp. 429–432. 2

[16] Schnur, J. M., "Lipid Tubules: A Paradigm f or Molecularly Engineered Structures," *Science*, Vol. 262, No. 5140, 1993, pp. 1669–1676. 2, 3

[17] Israelachvili, J. N., Mitchell, D. J., and Ninham, B. W., "Theory of self-assembly of hydrocarbon amphiphiles into micelles and bilayers," *J. Chem. Soc., Faraday Trans. 2*, Vol. 72, 1976, pp. 1525–1568. 2, 3

[18] Zhang, S., Marini, D. M., Hwang, W., and Santoso, S., "Design of nanostructured biological materials through self-assembly of peptides and proteins," 2002. 2

[19] Cucker, F. and Smale, S., "Emergent behavior in flocks," *IEEE Trans. Automat. Contr.*, Vol. 52, No. 5, 2007, pp. 852–862. 2, 60

[20] Li, F., Josephson, D. P., and Stein, A., "Colloidal assembly: The road from particles to colloidal molecules and crystals," Oct. 2011. 3

[21] Zhang, Z. and Glotzer, S. C., "Self-Assembly of Patchy Particles," *Nano Lett.*, Vol. 4, No. 8, Aug. 2004, pp. 1407–1413. 3, 4, 34, 41, 57, 78

[22] Zhang, Z., Keys, A. S., Chen, T., and Glotzer, S. C., "Self-assembly of patchy particles into diamond structures through molecular mimicry." *Langmuir*, Vol. 21, No. 25, Dec. 2005, pp. 11547–51. 3, 44, 57, 63, 70

[23] Chen, T., Zhang, Z., and Glotzer, S. C., "Simulation studies of the self-assembly of cone-shaped particles," *Langmuir*, Vol. 23, No. 12, June 2007, pp. 6598–6605. 3, 11

[24] Clark, N., Hurd, A., and Ackerson, B., "Single colloidal crystals," *Nature*, Vol. 281, 1979, pp. 57–60. 3

[25] Ozin, G. A., Hou, K., Lotsch, B. V., Cademartiri, L., Puzzo, D. P., Scotognella, F., Ghadimi, A., and Thomson, J., "Nanofabrication by self-assembly," May 2009. 3

[26] Paunov, V. and Cayre, O., "Supraparticles and "Janus" Particles Fabricated by Replication of Particle Monolayers at Liquid Surfaces Using a Gel Trapping Technique," *Adv. Mater.*, Vol. 16, No. 9-10, 2004, pp. 788–791. 4

[27] Cayre, O., Paunov, V. N., and Velev, O. D., "Fabrication of Asymmetrically Coated Colloid Particles by Microcontact Printing Techniques," *J. Mater. Chem.*, Vol. 13, 2003, pp. 2445–2450. 4

[28] Roh, K.-H., Martin, D. C., and Lahann, J., "Biphasic Janus Particles with Nanoscale Anisotropy," *Nat. Mater.*, Vol. 4, No. 10, Oct 2005, pp. 759–763. 4

[29] Zhang, G., Wang, D., and Möhwald, H., "Patterning Microsphere Surfaces by Templating Colloidal Crystals," *Nano Lett.*, Vol. 5, No. 1, 2005, pp. 143–146. 4

[30] Cui, J.-Q. and Kretzschmar, I., "Surface-Anisotropic Polystyrene Spheres by Electroless Deposition," *Langmuir*, Vol. 22, No. 20, 2006, pp. 8281–8284. 4

[31] Hong, L., Jiang, S., and Granick, S., "Simple Method to Produce Janus Colloidal Particles in Large Quantity," *Langmuir*, Vol. 22, No. 23, 2006, pp. 9495–9499. 4

[32] Zhang, Q., Lee, Y. H., Phang, I. Y., Pedireddy, S., Tjiu, W. W., and Ling, X. Y., "Bimetallic Platonic Janus Nanoparticles," *Langmuir*, Vol. 29, No. 41, 2013, pp. 12844–12851. 4

[33] Jackson, A. M., Myerson, J. W., and Stellacci, F., "Spontaneous assembly of subnanometre-ordered domains in the ligand shell of monolayer-protected nanoparticles," *Nature Materials*, Vol. 3, No. 5, 2004, pp. 330–336. 4

[34] Martin, B. R., Dermody, D. J., Reiss, B. D., Fang, M., Lyon, L. A., Natan, M. J., and Mallouk, T. E., "Orthogonal Self-Assembly on Colloidal Gold-Platinum Nanorods," *Adv. Mater.*, Vol. 11, No. 12, 1999, pp. 1021–1025. 4

[35] Wang, Y., Wang, Y., Breed, D. R., Manoharan, V. N., Feng, L., Hollingsworth, A. D., Weck, M., and Pine, D. J., "Colloids with valence and specific directional bonding." *Nature*, Vol. 491, No. 7422, Nov. 2012, pp. 51–5. 4, 76

[36] Pawar, A. B. and Kretzschmar, I., "Fabrication, Assembly, and Application of Patchy Particles," *Macromol. Rapid Commun.*, Vol. 31, No. 2, 2010, pp. 150–168. 4, 60

[37] Park, S., Lim, J.-H., Chung, S.-W., and Mirkin, C. A., "Self-Assembly of Mesoscopic Metal-Polymer Amphiphiles," *Science*, Vol. 303, No. 5656, 2004, pp. 348–351. 4

[38] Li, F., Yoo, W. C., Beernink, M. B., and Stein, A., "Site-Specific Functionalization of Anisotropic Nanoparticles: From Colloidal Atoms to Colloidal Molecules," *J. Am. Chem. Soc.*, Vol. 131, No. 51, 2009, pp. 18548–18555. 4

[39] Onoe, H., Matsumoto, K., and Shimoyama, I., "Three-Dimensional Sequential Self-Assembly of Microscale Objects," *Small*, Vol. 3, No. 8, 2007, pp. 1383–1389. 4

[40] Figuerola, A., Franchini, I. R., Fiore, A., Mastria, R., Falqui, A., Bertoni, G., Bals, S., Van Tendeloo, G., Kudera, S., Cingolani, R., and Manna, L., "End-to-End Assembly of Shape-Controlled Nanocrystals via a Nanowelding Approach Mediated by Gold Domains," *Adv. Mater.*, Vol. 21, No. 5, 2009, pp. 550–554. 4

[41] Rycenga, M., McLellan, J. M., and Xia, Y., "Controlling the Assembly of Silver Nanocubes through Selective Functionalization of Their Faces," *Adv. Mater.*, Vol. 20, No. 12, 2008, pp. 2416–2420. 4

[42] Zhang, G., Wang, D., and Möhwald, H., "Decoration of Microspheres with Gold Nanodots - Giving Colloidal Spheres Valences," *Angewandte Chemie International Edition*, Vol. 44, No. 47, 2005, pp. 7767–7770. 4

[43] Gangwal, S., Pawar, A., Kretzschmar, I., and Velev, O. D., "Programmed Assembly of Metallodielectric Patchy Particles in External AC Electric Fields," *Soft Matter*, Vol. 6, 2010, pp. 1413–1418. 4

[44] Chen, Q., Bae, S. C., and Granick, S., "Directed self-assembly of a colloidal kagome lattice," *Nature*, Vol. 469, 2011, pp. 381,384. 4

[45] Chen, Q., Whitmer, J. K., Jiang, S., Bae, S. C., Luijten, E., and Granick, S., "Supracolloidal Reaction Kinetics of Janus Spheres," *Science*, Vol. 331, No. 6014, 2011, pp. 199–202. 4

[46] Mao, Z., Xu, H., and Wang, D., "Molecular Mimetic Self-Assembly of Colloidal Particles," *Adv. Funct. Mater.*, Vol. 20, No. 7, March 2010, pp. 1053–1074. 4, 41

[47] Li, F., Josephson, D. P., and Stein, A., "Colloidal assembly: the road from particles to colloidal molecules and crystals." *Angew. Chem. Int. Ed. Engl.*, Vol. 50, No. 2, Jan. 2011, pp. 360–88. 4

[48] Onsager, L., "The Effects of Shape on the Interaction of Colloidal Particles," *Annals of the New York Academy of Sciences*, Vol. 51, No. 4, 1949, pp. 627–659. 4

[49] Frenkel, D., "Onsager's Spherocylinders Revisited," *J. Phys. Chem.*, Vol. 91, No. 19, 1987, pp. 4912–4916. 5, 21

[50] Stroobants, A., Lekkerkerker, H. N. W., and Frenkel, D., "Evidence for One-, Two-, and Three-Dimensional Order in a System of Hard Parallel Spherocylinders," *Phys. Rev. A*, Vol. 36, Sep 1987, pp. 2929–2945. 5, 21

[51] Murray, C. B., Kagan, C. R., and Bawendi, M. G., "S YNTHESIS AND C HARACTERIZATION OF M ONODISPERSE N ANOCRYSTALS AND C LOSE -P ACKED N ANOCRYSTAL A SSEMBLIES," *Annu. Rev. Mater. Res.*, Vol. 30, No. 1, Aug. 2000, pp. 545–610. 5

[52] Sun, Y. and Xia, Y., "Shape-controlled synthesis of gold and silver nanoparticles." *Science*, Vol. 298, No. 5601, Dec. 2002, pp. 2176–2179. 5

[53] Busbee, B., Obare, S., and Murphy, C., "An Improved Synthesis of High-Aspect-Ratio Gold Nanorods," *Adv. Mater.*, Vol. 15, No. 5, March 2003, pp. 414–416. 5

[54] Liu, H. and Alivisatos, a. P., "Preparation of Asymmetric Nanostructures through Site Selective Modification of Tetrapods," *Nano Lett.*, Vol. 4, No. 12, Dec. 2004, pp. 2397–2401. 5

[55] Schilling, T., Pronk, S., Mulder, B., and Frenkel, D., "Monte Carlo Study of Hard Pentagons," *Phys. Rev. E*, Vol. 71, Mar 2005, pp. 036138. 5, 21

[56] John, B. S., Juhlin, C., and Escobedo, F. A., "Phase Behavior of Colloidal Hard Perfect Tetragonal Parallelepipeds," *J. Chem. Phys.*, Vol. 128, No. 4, 2008, pp. 044909. 5, 21

[57] Haji-Akbari, A., Engel, M., Keys, A. S., Zheng, X., Petschek, R. G., Palffy-Muhoray, P., and Glotzer, S. C., "Disordered, quasicrystalline and crystalline phases of densely packed tetrahedra." *Nature*, Vol. 462, No. 7274, Dec. 2009, pp. 773–7. 5, 21, 22, 42, 44, 62

[58] Evers, W. H., Nijs, B. D., Filion, L., Castillo, S., Dijkstra, M., and Vanmaekelbergh, D., "Entropy-Driven Formation of Binary Semiconductor-Nanocrystal Superlattices," *Nano Lett.*, Vol. 10, No. 10, 2010, pp. 4235–4241. 5, 21

[59] Agarwal, U. and Escobedo, F. A., "Mesophase Behaviour of Polyhedral Particles," *Nat. Mater.*, Vol. 10, 2011, pp. 230–235. 5, 21, 74

[60] Zhao, K., Bruinsma, R., and Mason, T. G., "Entropic Crystal–Crystal Transitions of Brownian Squares," *Proc. Natl. Acad. Sci. U.S.A.*, Vol. 108, No. 7, 2011, pp. 2684–2687. 5, 21

[61] Haji-Akbari, A., Engel, M., and Glotzer, S. C., "Degenerate Quasicrystal of Hard Triangular Bipyramids," *Phys. Rev. Lett.*, Vol. 107, Nov 2011, pp. 215702. 5, 21

[62] Rossi, L., Sacanna, S., Irvine, W. T. M., Chaikin, P. M., Pine, D. J., and Philipse, A. P., "Cubic crystals from cubic colloids," *Soft Matter*, Vol. 7, 2011, pp. 4139–4142. 5, 20, 21, 40

[63] Damasceno, P. F., Engel, M., and Glotzer, S. C., "Crystalline assemblies and densest packings of a family of truncated tetrahedra and the role of directional entropic forces." *ACS Nano*, Vol. 6, No. 1, Jan. 2012, pp. 609–14. 5, 21, 22, 38, 41, 42, 44, 53, 63, 65, 70, 74, 75, 78

[64] Damasceno, P. F., Engel, M., and Glotzer, S. C., "Predictive self-assembly of polyhedra into complex structures." *Science*, Vol. 337, No. 6093, July 2012, pp. 453–7. 5, 21, 22, 41, 42, 44, 63, 69, 74, 75, 78

[65] Henzie, J., Grünwald, M., Widmer-Cooper, A., Geissler, P. L., and Yang, P., "Self-assembly of uniform polyhedral silver nanocrystals into densest packings and exotic superlattices," *Nat Mater*, Vol. 11, 2012, pp. 131,137. 5, 21

[66] Ni, R., Gantapara, A. P., de Graaf, J., van Roij, R., and Dijkstra, M., "Phase Diagram of Colloidal Hard Superballs: from Cubes via Spheres to Octahedra," *Soft Matter*, Vol. 8, 2012, pp. 8826–8834. 5, 21

[67] Zhang, J., Luo, Z., Martens, B., Quan, Z., Kumbhar, A., Porter, N., Wang, Y., Smilgies, D.-M., and Fang, J., "Reversible Kirkwood-Alder Transition Observed in Pt3Cu2 Nanoctahedron Assemblies under Controlled Solvent Annealing/Drying Conditions," *J. Am. Chem. Soc.*, Vol. 134, No. 34, 2012, pp. 14043–14049. 5, 21

[68] Agarwal, U. and Escobedo, F. A., "Effect of Quenched Size Polydispersity on the Ordering Transitions of Hard Polyhedral Particles," *J. Chem. Phys.*, Vol. 137, No. 2, 2012, pp. 024905. 5, 21

[69] Smallenburg, F., Filion, L., Marechal, M., and Dijkstra, M., "Vacancy-Stabilized Crystalline Order in Hard Cubes," *Proc. Natl. Acad. Sci. U.S.A.*, Vol. 109, No. 44, 2012, pp. 17886–17890. 5, 21

[70] Marechal, M., Patti, A., Dennison, M., and Dijkstra, M., "Frustration of the Isotropic-Columnar Phase Transition of Colloidal Hard Platelets by a Transient Cubatic Phase," *Phys. Rev. Lett.*, Vol. 108, May 2012, pp. 206101. 5, 21

[71] Gantapara, A. P., de Graaf, J., van Roij, R., and Dijkstra, M., "Phase Diagram and Structural Diversity of a Family of Truncated Cubes: Degenerate Close-Packed Structures and Vacancy-Rich States," *Phys. Rev. Lett.*, Vol. 111, Jul 2013, pp. 015501. 5, 21

[72] Cademartiri, L., Bishop, K. J. M., Snyder, P. W., and Ozin, G. A., "Using Shape for Self-Assembly," *Philos. Trans. R. Soc., A*, Vol. 370, No. 1969, 2012, pp. 2824–2847. 5, 20, 21

[73] Asakura, S. and Oosawa, F., "On Interaction between Two Bodies Immersed in a Solution of Macromolecules," *J. Chem. Phys.*, Vol. 22, No. 7, 1954, pp. 1255. 6, 7, 9, 19, 20, 34

[74] Vrij, A., "Polymers at Interfaces and the Interactions in Colloidal Dispersions," *Pure Appl. Chem.*, Vol. 48, 1976, pp. 471–483. 6, 20, 38

[75] Fåhraeus, R., "THE SUSPENSION STABILITY OF THE BLOOD," *Physiological Reviews*, Vol. 9, No. 2, 1929, pp. 241–274. 6

[76] Janzen, J. and Brooks, D., "Do plasma proteins adsorb to red cells?" *Clinical Hemorheology and Microcirculation*, Vol. 9, 1989, pp. 695. 6

[77] Doublier, J. L., Garnier, C., Renard, D., and Sanchez, C., "Protein-polysaccharide interactions," 2000. 6

[78] Leberman, R., "The isolation of plant viruses by means of "simple" coacervates." *Virology*, Vol. 30, No. 3, 1966, pp. 341–347. 6

[79] Cohen, S. S., "THE ISOLATION AND CRYSTALLIZATION OF PLANT VIRUSES AND OTHER PROTEIN MACRO MOLECULES BY MEANS OF HYDROPHILIC COLLOIDS," *Journal of Biological Chemistry*, Vol. 144, No. 2, 1942, pp. 353–362. 6

[80] Cockbain, E. G., "The aggregation of oil particles in emulsions," *Trans. Faraday Soc.*, Vol. 48, 1952, pp. 185–196. 6

[81] Fairhurst, D., Aronson, M., Ohm, M., and Goddard, E., "Some comments on non-ionic surfactant concentration effects in oil-in-water emulsions," 1983. 6

[82] Mason, T. G., "Osmotically driven shape-dependent colloidal separations," *Phys. Rev. E*, Vol. 66, Dec 2002, pp. 060402. 8, 20

[83] Park, K., Koerner, H., and Vaia, R. A., "Depletion-Induced Shape and Size Selection of Gold Nanoparticles," *Nano Lett.*, Vol. 10, 2010, pp. 1433–1439. 8

[84] Zhao, K. and Mason, T. G., "Directing Colloidal Self-Assembly through Roughness-Controlled Depletion Attractions," *Phys. Rev. Lett.*, Vol. 99, Dec 2007, pp. 268301. 8, 20, 57

[85] Barry, E. and Dogic, Z., "Entropy driven self-assembly of nonamphiphilic colloidal membranes," *Proc. Natl. Acad. Sci. U.S.A.*, Vol. 107, No. 23, 2010, pp. 10348–10353. 8, 20

[86] Sacanna, S., Irvine, W. T. M., Chaikin, P. M., and Pine, D. J., "Lock and key colloids." *Nature*, Vol. 464, No. 7288, March 2010, pp. 575–8. 8, 41, 60, 61

[87] Odriozola, G., Jiménez-Angeles, F., and Lozada-Cassou, M., "Entropy driven key-lock assembly." *J. Chem. Phys.*, Vol. 129, No. 11, Sept. 2008, pp. 111101. 8, 41, 61

[88] Ashton, D. J., Jack, R. L., and Wilding, N. B., "Self-assembly of colloidal polymers via depletion-mediated lock and key binding," *Soft Matter*, Vol. 9, No. 40, Dec. 2013, pp. 9661. 8, 41, 61

[89] Ashton, D. J., Ivell, S. J., Dullens, R. P. a., Jack, R. L., Wilding, N. B., and Aarts, D. G. a. L., "Self-assembly and crystallisation of indented colloids at a planar wall," *arXiv Prepr. arXiv ...*, Dec. 2014, pp. 1–8. 8

[90] Colón-Meléndez, L., Beltran-Villegas, D. J., van Anders, G., Liu, J., Spellings, M., Sacanna, S., Pine, D. J., Glotzer, S. C., Larson, R. G., and Solomon, M. J., "Binding kinetics of lock and key colloids," *J. Chem. Phys.*, Vol. 142, No. 17, 2015, pp. 174909. 8

[91] Lekkerkerker, H., Poon, W., Pusey, P., Stroobants, A., and Warren, P., "Phase Behaviour of Colloid + Polymer Mixtures," *Europhys. Lett.*, Vol. 20, No. 6, 1992, pp. 559–564. 8

[92] Lekkerkerker, H. and Widom, B., "An exactly solvable model for depletion phenomena," *Phys. A Stat. Mech. its Appl.*, Vol. 285, No. 3-4, Oct. 2000, pp. 483–492. 9

[93] Gnan, N., Zaccarelli, E., Tartaglia, P., and Sciortino, F., "How properties of interacting depletant particles control aggregation of hard-sphere colloids," *Soft Matter*, Vol. 8, No. 6, 2012, pp. 1991. 9

[94] Frenkel, D. and Smit, B., *Understanding Molecular Simulations: From Algorithms to Applications*, Elsevier, 2002. 11

[95] Allen, M. P. and Tildesley, D. J., *Computer simulation of liquids*, Clarendon Press, 1987. 11, 12

[96] Metropolis, N., Rosenbluth, A. W., Rosenbluth, M. N., Teller, A. H., and Teller, E., "Equation of state calculations by fast computing machines," *J. Chem. Phys.*, Vol. 21, 1953, pp. 1087–1092. 11, 12

[97] Lebowitz, J., Percus, J., and Verlet, L., "Ensemble Dependence of Fluctuations with Application to Machine Computations," *Phys. Rev.*, Vol. 153, No. 1, 1967, pp. 250. 11, 12

[98] Anderson, J. a., Jankowski, E., Grubb, T. L., Engel, M., and Glotzer, S. C., "Massively parallel monte carlo for many-particle simulations on GPUs," *J. Comput. Phys.*, Vol. 254, 2013, pp. 27–38. 14

[99] Marechal, M., Kortschot, R. J., Demirörs, A. F., Imhof, A., and Dijkstra, M., "Phase behavior and structure of a new colloidal model system of bowl-shaped particles." *Nano Lett.*, Vol. 10, No. 5, May 2010, pp. 1907–11. 14, 41, 43, 53, 61

[100] Marechal, M. and Dijkstra, M., "Phase behavior and structure of colloidal bowl-shaped particles: Simulations," *Phys. Rev. E*, Vol. 82, No. 3, Sept. 2010, pp. 1–11. 14, 41, 43, 53, 61

[101] Cinacchi, G. and van Duijneveldt, J. S., "Phase Behavior of Contact Lens-Like Particles: Entropy-Driven Competition between Isotropic−Nematic Phase Separation and Clustering," *J. Phys. Chem. Lett.*, Vol. 1, No. 4, Feb. 2010, pp. 787–791. 14, 41, 43

[102] Cinacchi, G., "Phase behavior of hard spherical caps." *J. Chem. Phys.*, Vol. 139, No. 12, Sept. 2013, pp. 124908. 14, 41, 43

[103] He, M. and Siders, P., "Monte Carlo calculation of orientationally anisotropic pair distributions and energy transfer in a model monolayer," *J. Phys. Chem.*, Vol. 94, No. 18, Sept. 1990, pp. 7280–7288. 14

[104] de Boer, J., "Molecular distribution and equation of state of gases," *Reports on Progress in Physics*, Vol. 12, No. 1, 1949, pp. 305. 20, 38

[105] Baumgartl, J., Dullens, R. P. A., Dijkstra, M., Roth, R., and Bechinger, C., "Experimental Observation of Structural Crossover in Binary Mixtures of Colloidal Hard Spheres," *Phys. Rev. Lett.*, Vol. 98, May 2007, pp. 198303. 20

[106] Zhao, K. and Mason, T. G., "Suppressing and Enhancing Depletion Attractions between Surfaces Roughened by Asperities," *Phys. Rev. Lett.*, Vol. 101, Sep 2008, pp. 148301. 20, 57

[107] Badaire, S., Cottin-Bizonne, C., Woody, J. W., Yang, A., and Stroock, A. D., "Shape Selectivity in the Assembly of Lithographically Designed Colloidal Particles," *J. Am. Chem. Soc.*, Vol. 129, No. 1, 2007, pp. 40–41. 20, 57

[108] Badaire, S., Cottin-Bizonne, C., and Stroock, A. D., "Experimental Investigation of Selective Colloidal Interactions Controlled by Shape, Surface Roughness, and Steric Layers," *Langmuir*, Vol. 24, No. 20, 2008, pp. 11451–11463, PMID: 18788764. 20, 57

[109] Yake, A. M., Snyder, C. E., and Velegol, D., "Site-Specific Functionalization on Individual Colloids: Size Control, Stability, and Multilayers," *Langmuir*, Vol. 23, No. 17, 2007, pp. 9069–9075. 20, 57

[110] Snyder, C. E., Ong, M., and Velegol, D., "In-Solution Assembly of Colloidal Water," *Soft Matter*, Vol. 5, 2009, pp. 1263–1268. 20, 57

[111] Kraft, D. J., Ni, R., Smallenburg, F., Hermes, M., Yoon, K., Weitz, D. A., van Blaaderen, A., Groenewold, J., Dijkstra, M., and Kegel, W. K., "Surface Roughness Directed Self-Assembly of Patchy Particles into Colloidal Micelles," *Proc. Natl. Acad. Sci. U.S.A.*, Vol. 109, No. 27, 2012, pp. 10787–10792. 20, 57

[112] Roth, R., van Roij, R., Andrienko, D., Mecke, K. R., and Dietrich, S., "Entropic Torque," *Phys. Rev. Lett.*, Vol. 89, Jul 2002, pp. 088301. 20, 22

[113] Young, K. L., Jones, M. R., Zhang, J., Macfarlane, R. J., Esquivel-Sirvent, R., Nap, R. J., Wu, J., Schatz, G. C., Lee, B., and Mirkin, C. A., "Assembly of Reconfigurable One-Dimensional Colloidal Superlattices due to a Synergy of Fundamental Nanoscale Forces," *Proc. Natl. Acad. Sci. U.S.A.*, Vol. 109, No. 7, 2012, pp. 2240–2245. 20

[114] Odriozola, G., Jimenez-Angeles, F., and Lozada-Cassou, M., "Entropy driven key-lock assembly," *The Journal of Chemical Physics*, Vol. 129, No. 11, 2008, pp. 111101. 20

[115] König, P.-M., Roth, R., and Dietrich, S., "Lock and key model system," *EPL (Europhysics Letters)*, Vol. 84, No. 6, 2008, pp. 68006. 20

[116] Sacanna, S., Irvine, W. T. M., Chaikin, P. M., and Pine, D., "Lock and key colloids," *Nature*, Vol. 464, 2010, pp. 575,578. 20

[117] Odriozola, G. and Lozada-Cassou, M., "Statistical Mechanics Approach to Lock-Key Supramolecular Chemistry Interactions," *Phys. Rev. Lett.*, Vol. 110, Mar 2013, pp. 105701. 20

[118] Sacanna, S. and Pine, D. J., "Shape-anisotropic colloids: Building blocks for complex assemblies," *Current Opinion in Colloid and Interface Science*, Vol. 16, No. 2, 2011, pp. 96 – 105. 20

[119] Israelachvili, J. N., Mitchell, D. J., and Ninham, B. W., "Theory of self-assembly of hyrocarbon amphiphiles into micelles and bilayers," *Journal of the Chemical Society, Faraday Transactions 2*, Vol. 72, 1976, pp. 1252–1568. 21

[120] Solomon, M. J., "Directions for targeted self-assembly of anisotropic colloids from statistical thermodynamics," *Curr. Opin. Colloid Interface Sci.*, Vol. 16, No. 2, 2011, pp. 158 – 167. 21

[121] Ashkin, A., Dziedzic, J. M., Bjorkholm, J. E., and Chu, S., "Observation of a single-beam gradient force optical trap for dielectric particles," *Opt. Lett.*, Vol. 11, No. 5, May 1986, pp. 288–290. 21

[122] Prasad, V., Semwogerere, D., and Weeks, E. R., "Confocal microscopy of colloids," *J. Phys. Condens. Matter*, Vol. 19, 2007, pp. 113102. 21, 60

[123] Young, K. L., Personick, M. L., Engel, M., Damasceno, P. F., Barnaby, S. N., Bleher, R., Li, T., Glotzer, S. C., Lee, B., and Mirkin, C. A., "A Directional Entropic Force Approach to Assemble Anisotropic Nanoparticles into Superlattices," *Angew. Chem., Int. Ed.*, Vol. in press, 2013. 22, 42, 57

[124] Croxton, C. and Osborn, T., "The development of torque fields at the surface of molecular fluids," *Physics Letters A*, Vol. 55, No. 7, 1975, pp. 415 – 416. 22

[125] König, P.-M., Roth, R., and Dietrich, S., "Depletion forces between nonspherical objects," *Phys. Rev. E*, Vol. 74, Oct 2006, pp. 041404. 22

[126] Anderson, P., "More Is Different," *Science*, Vol. 177, 1972, pp. 393,396. 40

[127] Avendaño, C., Liddell Watson, C. M., and Escobedo, F. A., "Directed self-assembly of spherical caps via confinement," *Soft Matter*, Vol. 9, No. 38, 2013, pp. 9153. 41, 43

[128] Ricci, M., Berardi, R., and Zannoni, C., "Columnar liquid crystals formed by bowl-shaped mesogens. A Monte Carlo study," *Soft Matter*, Vol. 4, No. 10, 2008, pp. 2030. 41

[129] Odriozola, G. and Lozada-Cassou, M., "Statistical Mechanics Approach to Lock-Key Supramolecular Chemistry Interactions," *Phys. Rev. Lett.*, Vol. 110, No. 10, March 2013, pp. 105701. 41, 61

[130] Colón-Meléndez, L., Beltrán-Villegas, D., van Anders, G., Liu, J., Spellings, M. P., Sacanna, S., Pine, D. J., Glotzer, S. C., Larson, R. G., and Solomon, M. J., "Binding kinetics of lock and key colloids," *Submitted*, 2014. 41, 61

[131] Bianchi, E., Blaak, R., and Likos, C. N., "Patchy colloids: state of the art and perspectives." *Phys. Chem. Chem. Phys.*, Vol. 13, No. 14, April 2011, pp. 6397–410. 41

[132] Onoe, H., Matsumoto, K., and Shimoyama, I., "Three-dimensional sequential self-assembly of microscale objects." *Small*, Vol. 3, No. 8, Aug. 2007, pp. 1383–9. 41

[133] Hong, L., Cacciuto, A., Luijten, E., and Granick, S., "Clusters of amphiphilic colloidal spheres." *Langmuir*, Vol. 24, No. 3, Feb. 2008, pp. 621–5. 41

[134] Biancaniello, P., Kim, A., and Crocker, J., "Colloidal Interactions and Self-Assembly Using DNA Hybridization," *Phys. Rev. Lett.*, Vol. 94, No. 5, Feb. 2005, pp. 058302. 41

[135] Park, S. Y., Lytton-Jean, A. K. R., Lee, B., Weigand, S., Schatz, G. C., and Mirkin, C. a., "DNA-programmable nanoparticle crystallization." *Nature*, Vol. 451, No. 7178, Jan. 2008, pp. 553–6. 41

[136] Ortiz, D., Kohlstedt, K. L., Nguyen, T. D., and Glotzer, S. C., "Self-assembly of reconfigurable colloidal molecules." *Soft Matter*, Vol. 10, No. 20, May 2014, pp. 3541–52. 44, 63, 78

[137] Lin, S., Fleming, J., and Hetherington, D., "A three-dimensional photonic crystal operating at infrared wavelengths," *Nature*, Vol. 24, No. 1997, 1998, pp. 1997–1999. 57

[138] Noda, S., "Full Three-Dimensional Photonic Bandgap Crystals at Near-Infrared Wavelengths," *Science (80-.).*, Vol. 289, No. 5479, July 2000, pp. 604–606. 57

[139] Aoki, K., Miyazaki, H. T., Hirayama, H., Inoshita, K., Baba, T., Shinya, N., and Aoyagi, Y., "Three-dimensional photonic crystals for optical wavelengths assembled by micromanipulation," *Appl. Phys. Lett.*, Vol. 81, No. 17, 2002, pp. 3122. 57

[140] Meseguer, F., "Colloidal crystals as photonic crystals," *Colloids Surfaces A Physicochem. Eng. Asp.*, Vol. 270-271, Dec. 2005, pp. 1–7. 57

[141] Romano, F., Sanz, E., and Sciortino, F., "Role of the range in the fluid-crystal coexistence for a patchy particle model." *J. Phys. Chem. B*, Vol. 113, No. 46, Nov. 2009, pp. 15133–6. 57

[142] Romano, F., Sanz, E., and Sciortino, F., "Phase diagram of a tetrahedral patchy particle model for different interaction ranges," *J. Chem. Phys.*, Vol. 132, No. 18, 2010, pp. 184501. 57

[143] Romano, F., Sanz, E., and Sciortino, F., "Crystallization of tetrahedral patchy particles in silico." *J. Chem. Phys.*, Vol. 134, No. 17, May 2011, pp. 174502. 57

[144] Rechtsman, M., Stillinger, F., and Torquato, S., "Synthetic diamond and wurtzite structures self-assemble with isotropic pair interactions," *Phys. Rev. E*, Vol. 75, No. 3, March 2007, pp. 031403. 57

[145] Sacanna, S. and Pine, D. J., "Shape-anisotropic colloids: Building blocks for complex assemblies," *Curr. Opin. Colloid Interface Sci.*, Vol. 16, No. 2, April 2011, pp. 96–105. 57, 60

[146] Glotzer, S. C., "Nanotechnology: Shape matters." *Nature*, Vol. 481, No. 7382, Jan. 2012, pp. 450–2. 57

[147] Sacanna, S., Korpics, M., Rodriguez, K., Colon-Melendez, L., Kim, S.-H., Pine, D. J., and Yi, G.-R., "Shaping Colloids for Self-Assembly," *Nat. Commun.*, Vol. 4, 2013, pp. 1688. 57, 61

[148] Ahmadi, T. S., Wang, Z. L., Green, T. C., Henglein, A., and El-Sayed, M. A., "Shape-Controlled Synthesis of Colloidal Platinum Nanoparticles," *Science*, Vol. 272, No. 5270, 1996, pp. 1924–1925. 57

[149] Sau, T. K. and Murphy, C. J., "Room Temperature, High-Yield Synthesis of Multiple Shapes of Gold Nanoparticles in Aqueous Solution," *J. Am. Chem. Soc.*, Vol. 126, No. 28, 2004, pp. 8648–8649. 57

[150] Demortière, A., Launois, P., Goubet, N., Albouy, P.-A., and Petit, C., "Shape-Controlled Platinum Nanocubes and Their Assembly into Two-Dimensional and Three-Dimensional Superlattices," *J. Phys. Chem. B*, Vol. 112, No. 46, 2008, pp. 14583–14592. 57

[151] Seo, D., Park, J. C., and Song, H., "Polyhedral Gold Nanocrystals with Oh Symmetry: From Octahedra to Cubes," *J. Am. Chem. Soc.*, Vol. 128, No. 46, 2006, pp. 14863–14870. 57

[152] Fan, F.-R., Liu, D.-Y., Wu, Y.-F., Duan, S., Xie, Z.-X., Jiang, Z.-Y., and Tian, Z.-Q., "Epitaxial Growth of Heterogeneous Metal Nanocrystals: From Gold Nanooctahedra to Palladium and Silver Nanocubes," *J. Am. Chem. Soc.*, Vol. 130, No. 22, 2008, pp. 6949–6951. 57

[153] Habas, S. E., Lee, H., Radmilovic, V., Somorjai, G. A., and Yang, P., "Shaping Binary Metal Nanocrystals through Epitaxial Seeded Growth," *Nat. Mater.*, Vol. 6, 2007, pp. 692–697. 57

[154] Song, H., Kim, F., Connor, S., Somorjai, G. A., and Yang, P., "Pt Nanocrystals: Shape Control and Langmuir–Blodgett Monolayer Formation," *J. Phys. Chem. B*, Vol. 109, No. 1, 2005, pp. 188–193. 57

[155] Skrabalak, S. E., Au, L., Li, X., and Xia, Y., "Facile Synthesis of Ag Nanocubes and Au Nanocages," *Nat. Protoc.*, Vol. 2, No. 9, 2007, pp. 2182–2190. 57

[156] Jana, N. R., Gearheart, L., and Murphy, C. J., "Wet Chemical Synthesis of Silver Nanorods and Nanowires of Controllable Aspect Ratio," *Chem. Commun.*, 2001, pp. 617–618. 57

[157] Kim, F., Connor, S., Song, H., Kuykendall, T., and Yang, P., "Platonic Gold Nanocrystals," *Angew. Chem., Int. Ed.*, Vol. 43, No. 28, 2004, pp. 3673–3677. 57

[158] Klajn, R., Pinchuk, A., Schatz, G., and Grzybowski, B., "Synthesis of Heterodimeric Sphere–Prism Nanostructures via Metastable Gold Supraspheres," *Angew. Chem., Int. Ed.*, Vol. 46, No. 44, 2007, pp. 8363–8367. 57

[159] Tian, N., Zhou, Z.-Y., Sun, S.-G., Ding, Y., and Wang, Z. L., "Synthesis of Tetrahexahedral Platinum Nanocrystals with High-Index Facets and High Electro-Oxidation Activity," *Science*, Vol. 316, No. 5825, 2007, pp. 732–735. 57

[160] Murphy, C. J., Sau, T. K., Gole, A. M., Orendorff, C. J., Gao, J., Gou, L., Hunyadi, S. E., and Li, T., "Anisotropic Metal Nanoparticles: Synthesis, Assembly, and Optical Applications," *J. Phys. Chem. B*, Vol. 109, No. 29, 2005, pp. 13857–13870. 57

[161] Grzelczak, M., Perez-Juste, J., Mulvaney, P., and Liz-Marzan, L. M., "Shape Control in Gold Nanoparticle Synthesis," *Chem. Soc. Rev.*, Vol. 37, 2008, pp. 1783–1791. 57

[162] Zhao, N., Ma, W., Cui, Z., Song, W., Xu, C., and Gao, M., "Polyhedral Maghemite Nanocrystals Prepared by a Flame Synthetic Method: Preparations, Characterizations, and Catalytic Properties," *ACS Nano*, Vol. 3, No. 7, 2009, pp. 1775–1780. 57

[163] Ho, C., Keller, A., Odell, J., and Ottewill, R., "Preparation of monodisperse ellipsoidal polystyrene particles," *Colloid Polym. Sci.*, Vol. 271, No. 5, 1993, pp. 469–479. 57

[164] Clark, T. D., Tien, J., Duffy, D. C., Paul, K. E., and Whitesides, G. M., "Self-Assembly of 10-μm-Sized Objects into Ordered Three-Dimensional Arrays," *J. Am. Chem. Soc.*, Vol. 123, No. 31, 2001, pp. 7677–7682. 57

[165] Velikov, K. P., van Dillen, T., Polman, A., and van Blaaderen, A., "Photonic crystals of shape-anisotropic colloidal particles," *Appl. Phys. Lett.*, Vol. 81, No. 5, 2002, pp. 838–840. 57

[166] van Dillen, T., Polman, A., van Kats, C. M., and van Blaaderen, A., "Ion beam-induced anisotropic plastic deformation at 300 keV," *Appl. Phys. Lett.*, Vol. 83, No. 21, 2003, pp. 4315–4317. 57

[167] Mohraz, A. and Solomon, M. J., "Direct Visualization of Colloidal Rod Assembly by Confocal Microscopy," *Langmuir*, Vol. 21, No. 12, 2005, pp. 5298–5306. 57

[168] Hernandez, C. J. and Mason, T. G., "Colloidal Alphabet Soup: Monodisperse Dispersions of Shape-Designed LithoParticles," *J. Phys. Chem. C*, Vol. 111, No. 12, 2007, pp. 4477–4480. 57

[169] Moon, J., Kim, A., Crocker, J., and Yang, S., "High-Throughput Synthesis of Anisotropic Colloids via Holographic Lithography," *Adv. Mater.*, Vol. 19, No. 18, 2007, pp. 2508–2512. 57

[170] Champion, J. A., Katare, Y. K., and Mitragotri, S., "Making polymeric micro- and nanoparticles of complex shapes," *Proc. Natl. Acad. Sci. U.S.A.*, Vol. 104, No. 29, 2007, pp. 11901–11904. 57

[171] Yanai, N. and Granick, S., "Directional Self-Assembly of a Colloidal Metal–Organic Framework," *Angew. Chem.*, Vol. 124, No. 23, 2012, pp. 5736–5739. 57

[172] Tao, A., Sinsermsuksakul, P., and Yang, P., "Tunable Plasmonic Lattices of Silver Nanocrystals," *Nat. Nanotechnol.*, Vol. 2, 2007, pp. 435–440. 57

[173] Zhang, L., Feng, G., Zeravcic, Z., Brugarolas, T., Liu, A. J., and Lee, D., "Using Shape Anisotropy to Toughen Disordered Nanoparticle Assemblies," *ACS Nano*, Vol. 7, No. 9, 2013, pp. 8043–8050. 57

[174] Fernandes, B. D., Spuch-Calvar, M., Baida, H., Tréguer-Delapierre, M., Oberlé, J., Langot, P., and Burgin, J., "Acoustic Vibrations of Au Nano-Bipyramids and their Modification under Ag Deposition: a Perspective for the Development of Nanobalances," *ACS Nano*, Vol. 7, No. 9, 2013, pp. 7630–7639. 57

[175] Sau, T. K. and Rogach, A. L., "Nonspherical Noble Metal Nanoparticles: Colloid-Chemical Synthesis and Morphology Control," *Adv. Mater.*, Vol. 22, No. 16, 2010, pp. 1781–1804. 57

[176] Xia, Y., Xiong, Y., Lim, B., and Skrabalak, S., "Shape-Controlled Synthesis of Metal Nanocrystals: Simple Chemistry Meets Complex Physics?" *Angew. Chem., Int. Ed.*, Vol. 48, No. 1, 2009, pp. 60–103. 57

[177] Désert, A., Hubert, C., Fu, Z., Moulet, L., Majimel, J., Barboteau, P., Thill, A., Lansalot, M., Bourgeat-Lami, E., Duguet, E., and Ravaine, S., "Synthesis and Site-Specific Functionalization of Tetravalent, Hexavalent, and Dodecavalent Silica Particles." *Angew. Chem. Int. Ed. Eng.*, , No. Figure 1, Sept. 2013, pp. 1–6. 57, 61, 74

[178] Aynajian, P., da Silva Neto, E. H., Gyenis, A., Baumbach, R. E., Thompson, J. D., Fisk, Z., Bauer, E. D., and Yazdani, A., "Visualizing heavy fermions emerging in a quantum critical Kondo lattice," *Nature*, Vol. 486, 2012, pp. 201–206. 60

[179] Anderson, P., "More is different," *Science*, Vol. 177, No. 4047, 1972, pp. 393–396. 60

[180] Kamien, R. D., "Entropic Attraction and Ordering," *Soft Matter, Volume 3, Colloidal Order: Entropic and Surface Forces*, edited by G. Gompper and M. Schick, Wiley-VCH, Weinheim, 2007. 60

[181] Shah, A., Schultz, B., Zhang, W., Glotzer, S. C., and Solomon, M. J., "Actuation of shape-memory colloidal fibres of Janus ellipsoids." *Nat. Mater.*, Vol. 14, No. January, 2014, pp. 117–124. 60

[182] Wang, W., Zhang, M.-J., Xie, R., Ju, X.-J., Yang, C., Mou, C.-L., Weitz, D. A., and Chu, L.-Y., "Hole–Shell Microparticles from Controllably Evolved Double Emulsions," *Angew. Chem. Int. Ed.*, Vol. 52, No. 31, 2013, pp. 8084–8087. 61

[183] Kim, S.-H., Hollingsworth, A. D., Sacanna, Stefano andChang, S.-J., Lee, G., Pine, D. J., and Yi, G.-R., "Synthesis and Assembly of Colloidal Particles with Sticky Dimples," *Journal of the American Chemical Society*, Vol. 134, No. 39, 2012, pp. 16115–16118. 61

[184] Ivell, S. J., Dullens, R. P. A., Sacanna, S., and Aarts, D. G. A. L., "Emerging structural disorder in a suspension of uniformly dimpled colloidal particles," *Soft Matter*, Vol. 9, 2013, pp. 9361–9365. 61

[185] Sacanna, S., Irvine, W. T. M., Rossi, L., and Pine, D. J., "Lock and key colloids through polymerization-induced buckling of monodisperse silicon oil droplets," *Soft Matter*, Vol. 7, 2011, pp. 1631–1634. 61

[186] Hales, T. C., "Some algorithms arising in the proof of the Kepler conjecture," *Ann. Math. Second Ser.*, Vol. 162, 2002, pp. 14. 61, 63

[187] Robbins, M. O., Kremer, K., and Grest, G. S., "Phase diagram and dynamics of Yukawa systems," *J. Chem. Phys.*, Vol. 88, No. 1988, 1988, pp. 3286. 61, 69

[188] Chen, E. R., Klotsa, D., Engel, M., Damasceno, P. F., and Glotzer, S. C., "Complexity in Surfaces of Densest Packings for Families of Polyhedra," *Phys. Rev. X*, Vol. 4, No. 1, Feb. 2014, pp. 011024. 63, 65, 74, 78

[189] Kallus, Y. and Elser, V., "Dense-packing crystal structures of physical tetrahedra," *Phys. Rev. E*, Vol. 83, No. 3, March 2011, pp. 036703. 65

[190] Monovoukas, Y. and Gast, A. P., "The experimental phase diagram of charged colloidal suspensions," *Journal of Colloid and Interface Science*, Vol. 128, 1989, pp. 533–548. 69

[191] Nykypanchuk, D., Maye, M. M., van der Lelie, D., and Gang, O., "DNA-guided crystallization of colloidal nanoparticles." *Nature*, Vol. 451, No. January, 2008, pp. 549–552. 69

[192] Macfarlane, R. J., Lee, B., Hill, H. D., Senesi, A. J., Seifert, S., and Mirkin, C. A., "Molecular recognition and self-assembly special feature: Assembly and organization processes in DNA-directed colloidal crystallization." *Proc. Natl. Acad. Sci. U. S. A.*, Vol. 106, No. 26, 2009, pp. 10493–10498. 69

[193] Childs, H., Brugger, E., Whitlock, B., Meredith, J., Ahern, S., Pugmire, D., Biagas, K., Miller, M., Harrison, C., Weber, G. H., Krishnan, H., Fogal, T., Sanderson, A., Garth, C., Bethel, E. W., Camp, D., Rübel, O., Durant, M., Favre, J. M., and Navrátil, P., "VisIt: An End-User Tool For Visualizing and Analyzing Very Large Data," *High Performance Visualization–Enabling Extreme-Scale Scientific Insight*, Oct 2012, pp. 357–372. 73

[194] Nguyen, T. D. and Glotzer, S. C., "Reconfigurable assemblies of shape-changing nanorods." *ACS Nano*, Vol. 4, No. 5, May 2010, pp. 2585–94. 74

[195] Zhang, Y., Lu, F., van der Lelie, D., and Gang, O., "Continuous Phase Transformation in Nanocube Assemblies," *Phys. Rev. Lett.*, Vol. 107, No. 13, Sept. 2011, pp. 135701. 74

[196] Kohlstedt, K. and Glotzer, S. C., "Self-assembly and tunable mechanics of reconfigurable colloidal crystals," *Phys. Rev. E*, Vol. 87, No. 3, March 2013, pp. 032305. 74

[197] Guo, R., Liu, Z., Xie, X.-M., and Yan, L.-T., "Harnessing Dynamic Covalent Bonds in Patchy Nanoparticles: Creating Shape-Shifting Building Blocks for Rational and Responsive Self-Assembly," *J. Phys. Chem. Lett.*, Vol. 4, No. 8, April 2013, pp. 1221–1226. 74

[198] Ku, K. H., Yang, H., Shin, J. M., and Kim, B. J., "Aspect ratio effect of nanorod surfactants on the shape and internal morphology of block copolymer particles," *J. Polym. Sci. Part A Polym. Chem.*, Aug. 2014. 74

[199] Ku, K. H., Shin, J. M., Kim, M. P., Lee, C.-H., Seo, M.-K., Yi, G.-R., Jang, S. G., and Kim, B. J., "Size-controlled nanoparticle-guided assembly of block copolymers for convex lens-shaped particles." *J. Am. Chem. Soc.*, Vol. 136, No. 28, July 2014, pp. 9982–9. 74

[200] de Graaf, J., van Roij, R., and Dijkstra, M., "Dense Regular Packings of Irregular Nonconvex Particles," *Phys. Rev. Lett.*, Vol. 107, No. 15, Oct. 2011, pp. 155501. 74

[201] Mao, X., Chen, Q., and Granick, S., "Entropy favours open colloidal lattices." *Nat. Mater.*, Vol. 12, No. 3, March 2013, pp. 217–22. 74

[202] Davis, M. E., "Ordered porous materials for emerging applications." *Nature*, Vol. 417, No. June, 2002, pp. 813–821. 74

[203] Dennison, M., Milinković, K., and Dijkstra, M., "Phase diagram of hard snowman-shaped particles." *J. Chem. Phys.*, Vol. 137, No. 4, 2012, pp. 044507. 75

[204] Milinković, K., Dennison, M., and Dijkstra, M., "Phase diagram of hard asymmetric dumbbell particles," *Phys. Rev. E*, Vol. 87, No. 3, March 2013, pp. 032128. 75

[205] Kim, J. W., Larsen, R. J., and Weitz, D. A., "Synthesis of nonspherical colloidal particles with anisotropic properties," *J. Am. Chem. Soc.*, Vol. 128, No. 44, 2006, pp. 14374–14377. 75

[206] Kim, J. W., Larsen, R. J., and Weitz, D. A., "Uniform nonspherical colloidal particles with tunable shapes," *Adv. Mater.*, Vol. 19, No. 15, 2007, pp. 2005–2009. 75

[207] Wagner, C. S., Yan, L., and Wittemann, A., "Preparation of submicrometer-sized clusters from polymer spheres using ultrasonication," *Langmuir*, Vol. 24, No. 20, 2008, pp. 12126–12128. 75

[208] Lee, K. J., Yoon, J., and Lahann, J., "Recent advances with anisotropic particles," *Curr. Opin. Colloid Interface Sci.*, Vol. 16, No. 3, June 2011, pp. 195–202. 75

[209] Koo, H., Yi, D., Yoo, S., and Kim, D.-Y., "A Snowman-like Array of Colloidal Dimers for Antireflecting Surfaces," *Adv. Mater.*, Vol. 16, No. 3, 2004, pp. 274–277. 75

[210] van Blaaderen, A., "Chemistry. Colloidal molecules and beyond." *Science*, Vol. 301, No. 5632, 2003, pp. 470–471. 76

[211] Manoharan, V. N., Elsesser, M. T., and Pine, D. J., "Dense packing and symmetry in small clusters of microspheres." *Science*, Vol. 301, No. 5632, 2003, pp. 483–487. 76

[212] Kraft, D. J., Groenewold, J., and Kegel, W. K., "Colloidal molecules with well-controlled bond angles," *Soft Matter*, Vol. 5, No. 20, 2009, pp. 3823. 76

[213] Kraft, D. J., Vlug, W. S., Van Kats, C. M., Van Blaaderen, A., Imhof, A., and Kegel, W. K., "Self-assembly of colloids with liquid protrusions," *J. Am. Chem. Soc.*, Vol. 131, No. 6, 2009, pp. 1182–1186. 76

[214] Perro, A., Duguet, E., Lambert, O., Taveau, J.-C., Bourgeat-Lami, E., and Ravaine, S., "A chemical synthetic route towards "colloidal molecules"." *Angew. Chem. Int. Ed. Engl.*, Vol. 48, No. 2, Jan. 2009, pp. 361–5. 76